Multi-Core Fiber for High-Capacity Spatially-Multiplexed Transmission

（大容量空間多重伝送用マルチコアファイバ）

by

HAYASHI, Tetsuya

A Thesis Submitted in Partial Fulfillment of the Requirements for the Degree of Doctor of Philosophy in Engineering

Division of Media and Network Technologies
Graduate School of Information Science and Technology
Hokkaido University

Supervisor: SAITOH, Kunimasa, Professor

August 2013

Contents

List of Figures

List of Tables

Chapter 1

Introduction

1.1 Background of the Research

1.1.1 Exponential Growth of the Network Traffic, and the Capacity Limit of the Optical Fiber

The data traffic is exponentially increasing in the various network fields, as shown in Fig. 1.1 (see Ref. [1] for the details). For example, the Internet traffic is growing by 20%–60% in a year, and this trend is estimated to continue [1–3].

On the other hand, as shown in Fig. 1.2, the transmission capacity of optical fiber has also exponentially grown in the past few decades [2, 3], owing to the emergences of various new technologies.

Recent single-core transmission systems have achieved capacities up to about 100 Tb/s per fiber by employing

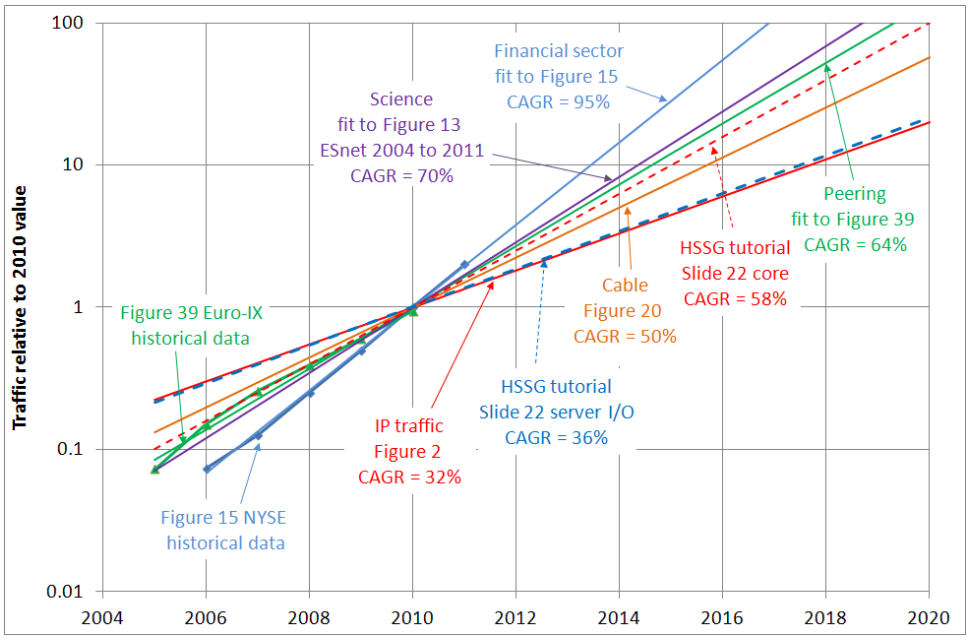

Fig. 1.1: Relative traffic increase normalized to 2010. (Reproduced from Ref. [1] © 2012 IEEE.)
(IP: Internet Protocol, Euro-IX: the European Internet Exchange Association,
HSSG: IEEE 802.3 Higher Speed Study Group Tutorial [4],
CAGR: Compounded Annual Growth Rate)

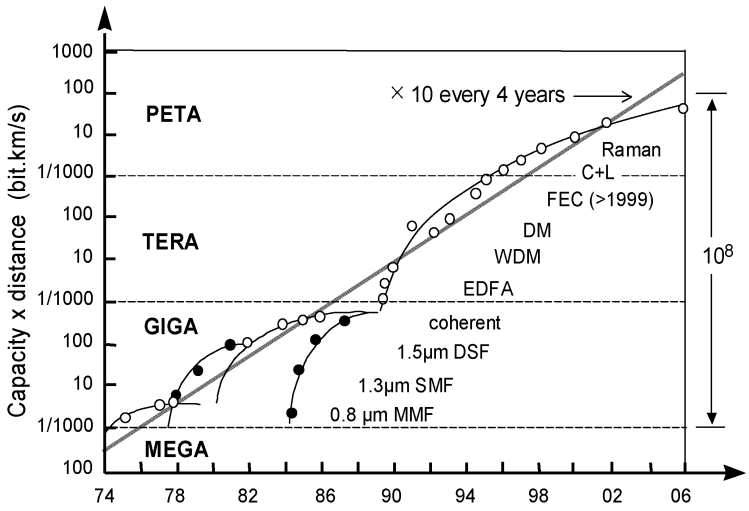

(a) Growth of the capacity-distance product. (Reproduced from Ref. [2] © 2006 IEEE.)
MMF: multi-mode fiber, SMF: single-mode fiber, DSF: dispersion-shifted fiber, EDFA: Erbium-doped fiber amplifier, WDM: wavelength division multiplexing, DM: dispersion management, FEC: forward error correction, C+L: WDM over C+L band (1530–1625 nm), Raman: Raman amplification

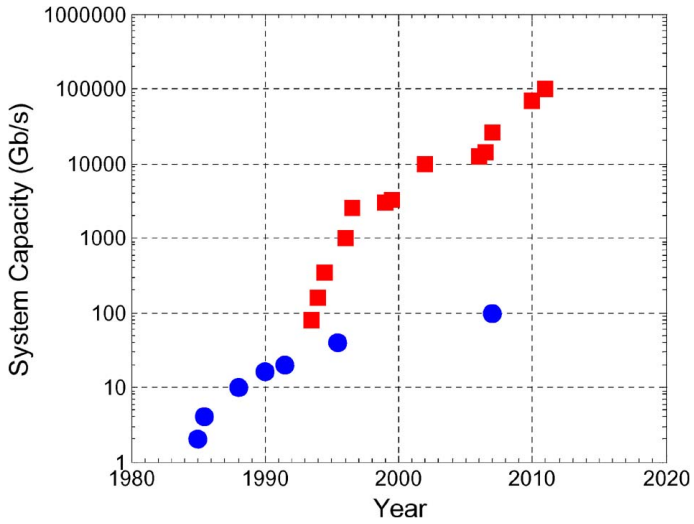

(b) Growth of the system capacity—total capacity for a single fiber in laboratory/research demonstrations. (Reproduced from Ref. [3] © 2012 IEEE.)
(Filled circles: TDM systems, filled squares: WDM systems)

Fig. 1.2: Growth of the transmission capacity of optical fiber.

time-, wavelength-, polarization-division multiplexings, and multi-level modulations [5]. For further increasing the fiber capacity, expansion of the optical bandwidth of transmission window and enhancement of the spectral efficiency (SE) are required. However, the C+L band (see Fig. 1.3) has already been used up, which is the transmission suitable band (1530–1625 nm) because of the low attenuation of silica glass and of the low noise and high gain of erbium-doped fiber amplifier. Achieving low-noise long-haul transmission using other bands is difficult due to the high attenuation of the fibers and the lack of good amplifiers.

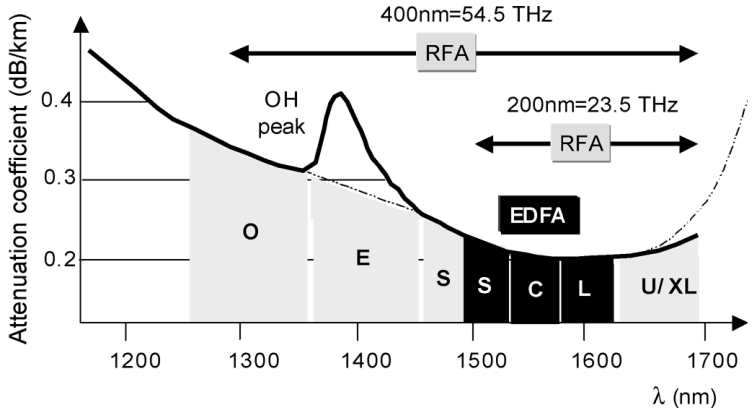

Fig. 1.3: Transmission window of fused-silica fibers showing standard optical amplification bands (O, E, S, C, L, and U/XL). (Reproduced from Ref. [2] © 2006 IEEE.)

Furthermore, even if the fundamental limits of low loss and low nonlinearity could be achieve in the hollow-core fiber, the improvement of signal-to-noise ratio will result in only a slight increase of SE, as shown in Fig. 1.4. Therefore, the transmission capacity of the single-core fiber is rapidly approaching its fundamental limit, and the current trends of traffic growth will result in capacity crunch in the near future [3, 6].

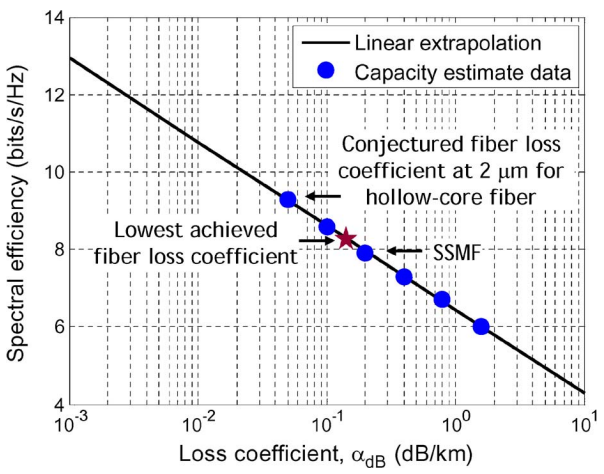

(a) Calculated maximum spectral efficiency for various fiber loss coefficients and a linear extrapolation.

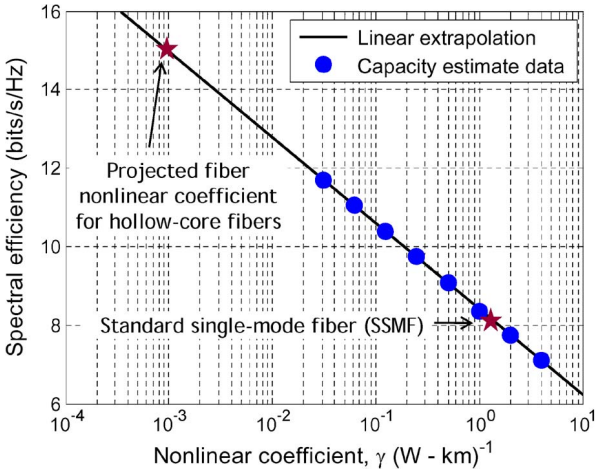

(b) Calculated maximum spectral efficiency for various fiber nonlinear coefficients and a linear extrapolation.

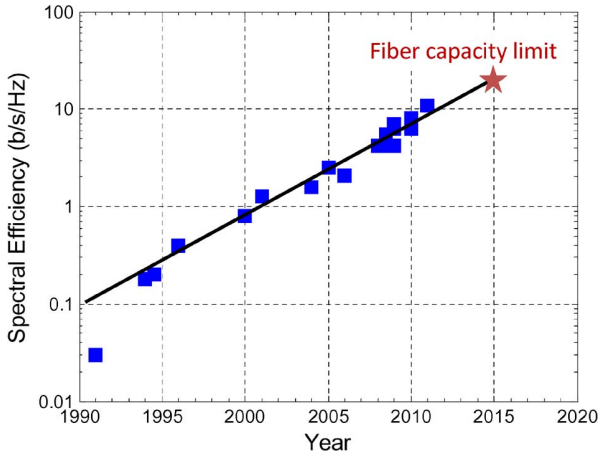

(c) Spectral efficiency achieved in research demonstrations versus year.

Fig. 1.4: Calculated limit of spectral efficiency. (Reproduced from Ref. [3] © 2012 IEEE.)

1.1.2 Studies on the Spatially-Multiplexed Transmission for Breaking Through the Capacity Limit.

In such a situation, spatial-division multiplexing (SDM) is an attractive technology for further enlargement of the fiber capacity or spatial capacity—the capacity per cross-sectional area of the fiber [2, 3, 7].

Concepts of SDM optical fiber transmission are not so new [8–10]. Multi-core fiber (MCF) for high density transmission was first proposed in the late 1970s [8, 9]. This MCF was drawn from one preform including multiple cores; therefore, its cladding was circular shaped and similar to recent MCFs (see Fig. 1.5a). However, since there was a difficulty in aligning and splicing the multiple cores in circular MCFs, another type of MCF, the so called

bunch fiber, was proposed [11]. The bunch fiber is drawn from bunched multiple preforms and each preform includes one respective core, and thus has non-circular cladding (see Figs. 1.5b and 1.5c, for examples). The bunch fiber had been developed for use in subscriber lines [12–15]. However, the passive optical network (PON) [16] was able to provide cost- and space-efficient networks for the subscriber lines, and the MCF became unnecessary for the density improvement and have not been commercialized for SDM transmission.

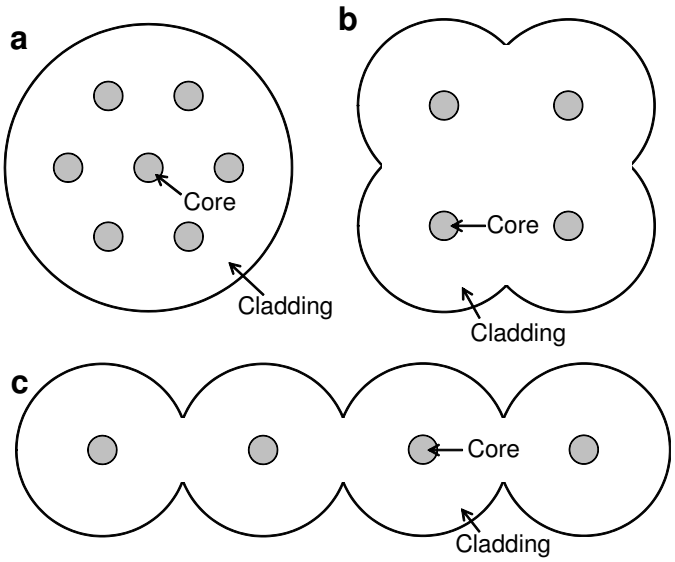

Fig. 1.5: Schematic cross-sections of (a) a normal MCF and (b,c) bunched MCFs.

In the late 2000s, the SDM technologies had rapidly come to attract attentions again [7], since the future capacity crunch became a reality [2,3,6], as reviewed in Section 1.1.1. At the time of writing—the first half of 2013—, the research on the optical fibers for the SDM ranges for various technologies, such as:

- Fiber types:
  - The so-called uncoupled MCF [17], wherein each core is used as an individual waveguide.
  - The so-called coupled MCF [18–20], wherein a set of multiple cores is used as one few-mode waveguide.
  - The so-called few-mode fiber (FMF) [21–24], wherein a core guides a few or several spatial modes (different from the conventional multi-mode fiber that supports hundreds of spatial modes).
- Types of transmission systems regarding to the crosstalk between spatial channels:
  - Low crosstalk is required, but the conventional high capacity transmitters and receivers can be utilized [17–19, 21].
  - High crosstalk can be accepted, but signal processing using multiple-input-multiple-output (MIMO) is required [20, 22–24].

- Types of multiplexed spatial modes:
  - The linearly-polarized (LP) modes [17].
  - The supermodes [18, 19].
  - The orbital angular momentum (OAM) modes [25–27].

1.2 Overview

From mid 2009, we have conducted the research and development of uncoupled MCFs toward the practical realization in the high-capacity long-haul transmission. This thesis describes our research on the uncoupled MCF for SDM transmission. The uncoupled MCF is just referred to as MCF in this thesis.

The rest of this thesis is organized as follows.

Chapter 2 describes the results of our feasibility study on the MCF. We studied on characteristics degradations specific to the MCF, in order to investigate whether or not the degradations can be suppressed. In the study, we revealed that the inter-core XT of the MCF is heavily dependent not only on the fiber structure but also on the fiber bend, from the theoretical and experimental investigations. It was also revealed that the XT is a stochastic value. We also found that the losses of outer cores of a MCF can be degraded if the outer cores are too close to the coating, because the powers guided in the cores can couple to the coating with high refractive index.

In Chapter 3, we propose a suppression method of the crosstalk of the homogeneous MCF, which utilizes the fiber bend. We developed an approximation model and derived analytical expressions of the statistical characteristics of the XT of the homogeneous MCF, so that we can easily design homogeneous MCFs. The derived expression for the statistical mean of the XT is quite simple, thus are widely used for estimating the XT of homogeneous MCFs at present. We also developed a XT measurement method with wavelength scanning to obtain the statistical properties of the XT. Based on the results of Chapter 2 and these developments, we designed and fabricated an ultra-low-XT MCF, and demonstrated that the XT of the MCF can be suppressed enough for ultra-long-haul ($>$10,000 km) transmissions.

In Chapter 4, we discuss how the XT behaves stochastically, reveal the behavior of the XT as a noise, and consider and quantify the effect of the XT on Q-factor, since the target levels of the XT in earlier studies and the previous chapters did not necessarily have the theoretical grounding, and the stochasticity of the XT has not been taken into account.

Chapter 5 describes how we can enhance the signal-to-noise ratio (SNR) in each core of the MCF, and how the XT can affect the SNR. We present a low-loss large-effective-area MCF whose XT is properly suppressed so that the XT can be adequately lower than the amplified spontaneous emission noise and the nonlinear interference

noise. In addition, we discuss how this result enhances the SNR in multi-core transmission systems.

In Chapter 6, since after a few years of the intensive research by various groups, including us, the characteristics of the inter-core crosstalk (XT) of the multi-core fiber (MCF) have been well elucidated, we review the essence of these studies on the XT, clarify ambiguous points of the studies, and derive a novel expression of the average power-coupling coefficient, with which we can understand the behavior of the XT and interpret its physical meaning easily. Based on the derived expression, we discuss how the longitudinal fluctuation of fiber structures and the macrobend can affect the XT, and organize the previously-reported methods for XT suppression.

In Chapter 7, we studied how the XT is affected by the fiber splice, the tight macrobend, and the microbend—these factors are possible to be induced in installed MCFs. For examples, actually-deployed MCF link can consist of concatenated MCFs and have many splicing points, the MCF may be tightly bent at around splices and connections, and the microbend—that is, the microscopic fiber bend induced by external stresses— can be an issue when the MCF is cabled. So, XT degradations due to these factors must be suppressed, toward the practical realization of the multi-core fiber (MCF).

Finally, Chapter 8 concludes this thesis.

Chapter 2

Feasibility Study on Multi-Core Fiber

2.1 Introduction to This Chapter

At the time when we started this study, Koshiba *et al.* had reported that the inter-core crosstalk (XT) of the MCF can be suppressed less than −30 dB after 100 km propagation, even for the all-solid MCF—fit to mass-production process— with 7–19 step-index cores and the cladding diameter of 125 μm, by inducing slight differences in the effective indices between neighboring cores, from the theoretical consideration based on the coupled-mode theory [17]. However, the all-solid MCF had not been well investigated by actual fabrication yet, though photonic-crystal MCFs—difficult to fabricate in low loss and in large volume— had been started to be investigated [28, 29].

Therefore, at first, we studied on the feasibility of the MCF, that is, whether or not the all-solid MCF can be fabricated without significant characteristics degradations. So, this chapter describes the characteristics degradations specific to the MCF. The basic study on the inter-core XT of the MCFs is described in Section 2.2, and the loss degradation of outer cores near the coating is described in Section 2.3.

2.2 Basic Study on Inter-Core Crosstalk

Suppression of the XT is crucial to transmit signals individually through each core of the MCF.

In this section, theoretical background of earlier studies are briefly reviewed, inapplicability of the earlier study to actual MCFs is experimentally demonstrated, and significant effect of fiber bend on the XT is theoretically and experimentally revealed.

2.2.1 Theoretical Background of Earlier Studies

Until we started the study on the MCF, some research groups had investigated the crosstalk of the MCF and reported that a slight difference in the effective refractive indices, or the propagation constants, between cores of the MCF can effectively suppress the XT between the cores [15, 17, 30]. All of these studies were based on the simple coupled-mode theory, which holds in cases of short waveguide or of very ideal longitudinally-unperturbed waveguide. This section briefly reviews the coupled-mode theory and the XT suppression method based on it.

The coupled-mode equation for optical fiber(s) with parallel cores is expressed as [31]:

$$\frac{d\boldsymbol{E}}{dz} = -j\left(\boldsymbol{\beta} + \boldsymbol{\kappa}\right)\boldsymbol{E}, \tag{2.1}$$

where $\boldsymbol{E} = [E_1, E_2, \ldots, E_N]^T$ is the vector of the electric fields E_n of the each core modes, $\boldsymbol{\beta} = \mathrm{diag}\left(\beta_1, \beta_2, \ldots, \beta_N\right)$ is $N \times N$ diagonal matrix which includes the propagation constants $\beta = (2\pi/\lambda) n_{\mathrm{eff}}$, λ is the wavelength in vacuum, n_{eff} is the effective refractive index, and $\boldsymbol{\kappa}$ is $N \times N$ matrix including the mode-coupling coefficients κ_{nm} from Core m to Core n, which is expressed as:

$$\kappa_{nm} = \frac{\omega\varepsilon_0 \iint \left(n^2 - n_m^2\right) \boldsymbol{e}_n^* \cdot \boldsymbol{e}_m \, dxdy}{\iint \hat{z} \cdot \left(\boldsymbol{e}_n^* \times \boldsymbol{h}_n + \boldsymbol{e}_n \times \boldsymbol{h}_n^*\right) dxdy}, \tag{2.2}$$

where ω is the angular frequency of the light in vacuum, ε_0 the vacuum permittivity, n is the actual index profile, n_m is the index profile of Core m in the absence of the other cores, $\boldsymbol{e}$ the normalized vector core mode of the electric field, $\boldsymbol{h}$ the normalized vector core mode of the magnetic field, the superscript $*$ indicates the complex conjugate, and $\hat{z}$ is the unit vector in the direction of z axis.

Since $\boldsymbol{E}$ can be expressed as

$$\boldsymbol{E} = \exp\left(-j\boldsymbol{\beta} z\right)\boldsymbol{A}, \tag{2.3}$$

where $\boldsymbol{A} = [A_1, A_2, \ldots, A_N]^T$ is the vector of the complex amplitudes A_n of E_n, Eq. 2.1 can be rewritten as

$$\frac{d\boldsymbol{A}}{dz} = -j\exp\left(j\boldsymbol{\beta} z\right)\boldsymbol{\kappa}\exp\left(-j\boldsymbol{\beta} z\right)\boldsymbol{A}. \tag{2.4}$$

A component of Eq. 2.5 is the well-know form of the coupled-mode equation and represented as

$$\frac{dA_n}{dz} = \sum_m -j\kappa_{nm}\exp\left[j\left(\beta_n - \beta_m\right)z\right]A_m. \tag{2.5}$$

In the two core case—Core m and Core n—, when only Core m is excited ($|A_m(0)| = 1$), the power of Core n is derived as

$$|A_n|^2 = F_{nm}\sin^2\left(q_{nm} z\right), \tag{2.6}$$

$$F_{nm} = \frac{\kappa_{nm}^2}{\kappa_{nm}^2 + \left(\frac{\beta_n - \beta_m}{2}\right)^2}, \tag{2.7}$$

$$q_{nm} = \sqrt{\kappa_{nm}^2 + \left(\frac{\beta_n - \beta_m}{2}\right)^2}, \tag{2.8}$$

where F is the maximum power transfer ratio. Figure 2.1 shows the relationship between the difference in the effective indices between cores and the maximum power transfer ratio F at 1550 nm. Indeed, F is suppressed to be less than 0.001 (-30 dB) by only a slight difference of 0.001 in n_{eff} between cores, even when $\kappa = 10$ [/m].

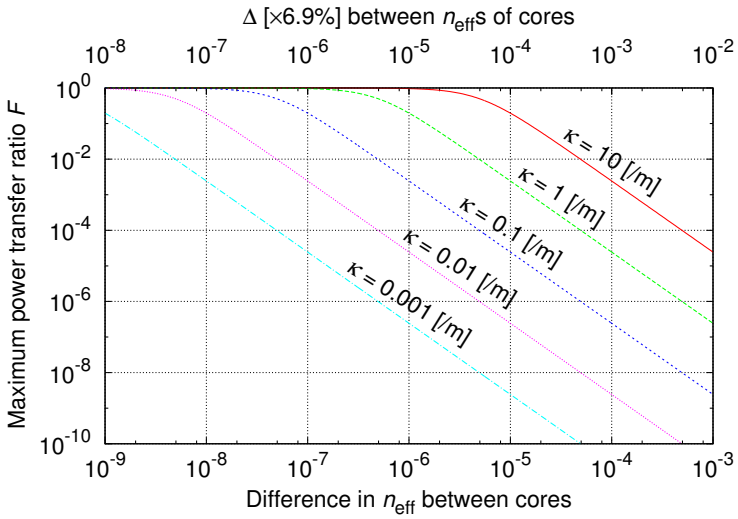

Fig. 2.1: The relationship between the difference in the effective indices between cores and the maximum power transfer ratio F at 1550 nm.

2.2.2 Experimental Trial for Crosstalk Suppression: Validation of the Earlier Theoretical Prediction

To confirm actual capability of the heterogeneous MCF structure to suppress the XT, we designed and fabricated a heterogeneous MCF. The wavelength of 1550 nm and the core pitch of 30 μm were assumed for the design. The heterogeneous MCF had equal outer cores and a dissimilar center core, as shown in Fig. 2.2, so that the XT between the center core and the outer cores was expected to be suppressed.

We designed the MCF cores based on the pure-silica-core technology; thus, the all cores were designed to have the same core Δ, which was about 0.38%. Figure 2.3 shows the relationship between the core diameter and the effective refractive index of the core, which was calculated using a full-vectorial finite-element imaginary-distance beam propagation method (FE-ID-BPM) [32] from a refractive index profile of a preform of a single-core fiber fabricated with the same fabrication process and the same design of the MCF core. Since Ref. [17] suggested that the difference in the core Δ between neighboring cores more than ±0.005% can suppress the XT at the core-to-core distance larger than 30 μm, we designed the center core and the outer cores to have the difference of more than 0.01% in the effective indices, by changing the diameters of the cores. The core diameters were designed

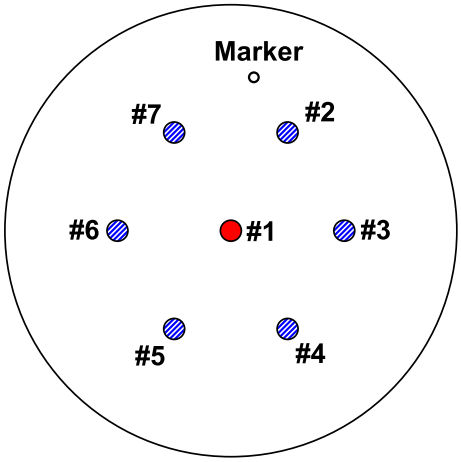

Fig. 2.2: Schematic cross-section of the designed heterogeneous MCF.

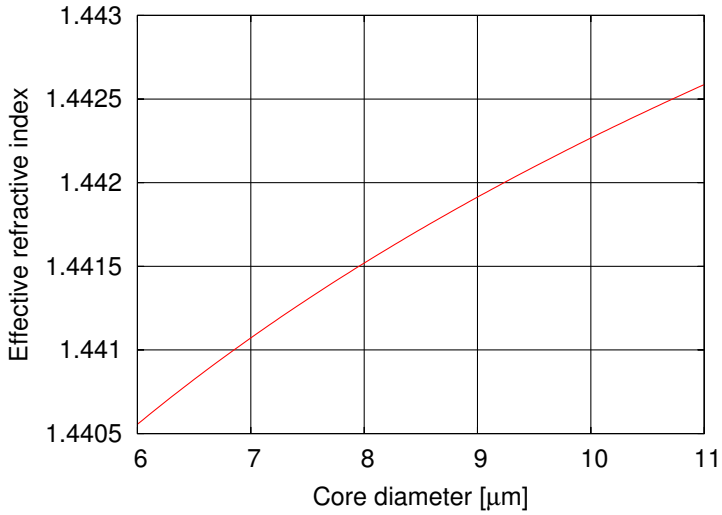

Fig. 2.3: The relationship between the core diameter and the effective refractive index.

to be 8.9 μm for the center core and 9.4 μm for the outer cores, so that the Δ between the effective indices of the center core and the outer core was designed to be about 0.012%.

Figure 2.4 shows the calculated longitudinal power evolutions of cores, which was calculated for the case where only the center core of the designed MCF is excited, by using the simple coupled-mode equation. The maximum XT was calculated to be less than −40 dB; thus, the XT was considered to be suppressed very well based on the earlier studies.

For obtaining more information on the dependence of the MCF characteristics on the MCF structures, we drew three kinds of MCFs which has different cladding diameters from one preform as shown in Table 2.1. A cross-section of MCF-A30 is shown in Fig. 2.5.

The setup for XT measurement is shown in Fig. 2.6. The light source was a laser diode whose wavelength is

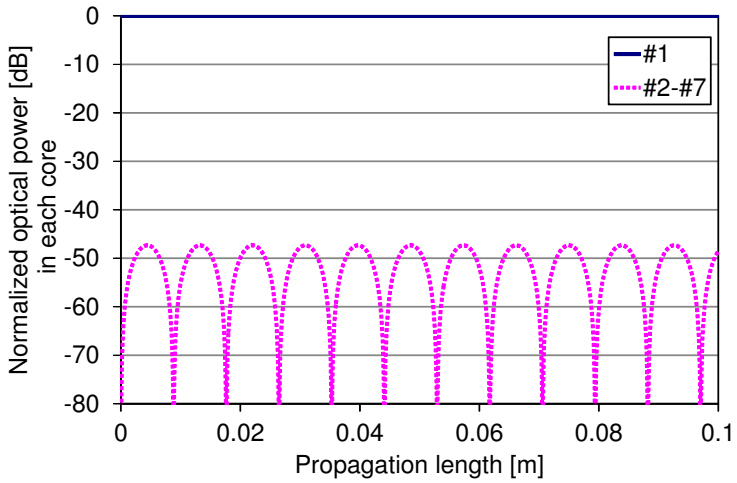

Fig. 2.4: Longitudinal power evolutions of cores of the designed MCF, which was calculated using the simple coupled-mode equation.

Table. 2.1: Design properties of MCF-A.

		MCF-A26	MCF-A30	MCF-A34
Core Δ [%]		0.38		
Core pitch [μm]		26	30	34
Diameter [μm]	Center core	7.7	8.9	10.1
	Outer cores	8.1	9.4	10.7
	Cladding	108.3	125	141.7

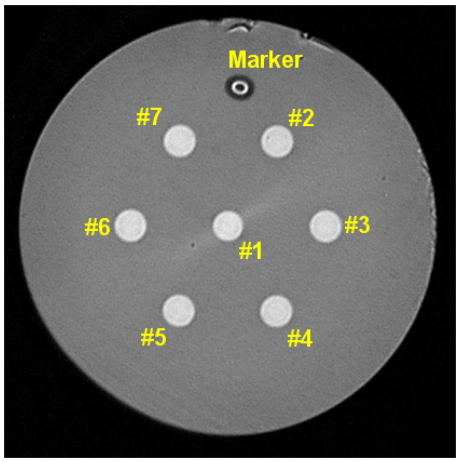

Fig. 2.5: A cross-section of the fabricated MCF-A30.

1.55 μm and linewidth is less than 10 nm. The XT was obtained by measuring the output power of each core when exciting one core. Here, the XT was defined as the ratio of output power of a certain core divided by sum of output powers of all cores. We measured the XT of 2-m-long MCF-A26, MCF-A30, and MCF-A34; 3-km-long MCF-A26; and 5-km-long MCF-A30 and MCF-A34. The bend radii R_b of the 2-m-long MCFs were not controlled, but no tight bend was applied to the MCFs. The kilometers-long MCFs were wound on 140-mm-radius bobbins.

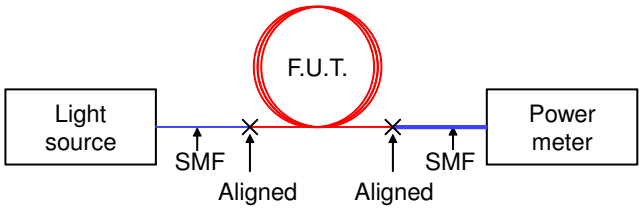

Fig. 2.6: The crosstalk measurement setup.

Figure 2.7 shows the measurement results. Figures 2.7a and 2.7b show the results for the 2-m-long MCFs, and Figs. 2.7c and 2.7d show the results for the MCFs longer than a kilometer—3 km of MCF-A26, and 5 km of MCF-A30 and MCF-A34. Even in the cases of the 2-m-long MCFs, the XT was higher than the estimated value. Furthermore, the XT of the kilometers-long MCFs were so high that the output powers were converged to equilibrium; the only exception was the case where Core 5 was excited in MCF-A34—this is because the number of surrounding core of Core 5 is fewer than that of Core 1.

The measurement results clearly demonstrated that the XT of actual MCFs are completely discrepant from the prediction based on the earlier studies.

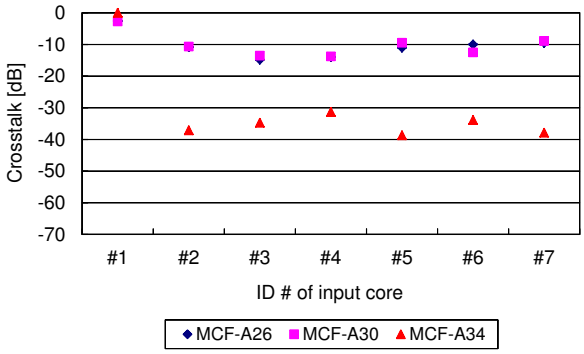

(a) Excited core: Core 1,
Fiber length: 2 m.

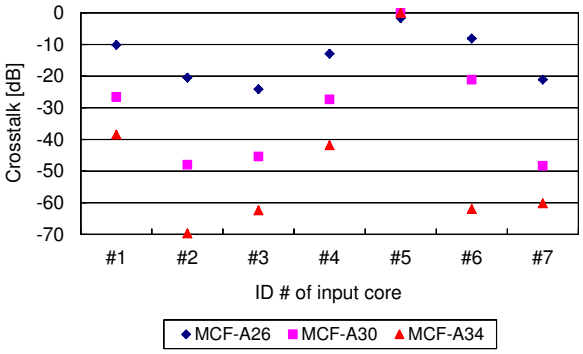

(b) Excited core: Core 5,
Fiber length: 2 m.

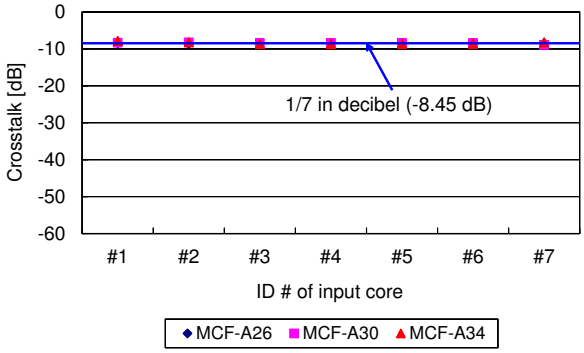

(c) Excited core: Core 1,
Fiber length: 3 km of MCF-A26,
5 km of MCF-A30,
5 km of MCF-A34.

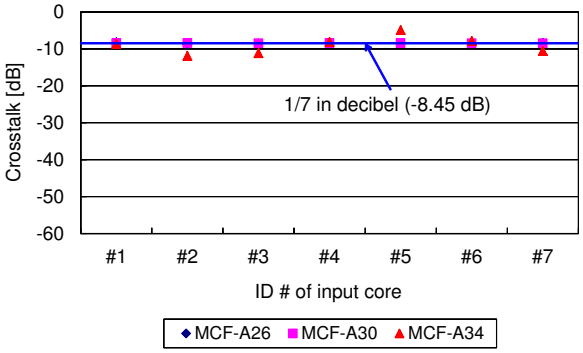

(d) Excited core: Core 5,
Fiber length: 3 km of MCF-A26,
5 km of MCF-A30,
5 km of MCF-A34.

Fig. 2.7: Crosstalk of MCF-A wound on 140-mm-radius bobbin, measured at λ = 1550 nm.

2.2.3 The Reason of the Discrepancy in the Crosstalk between the Prediction and the Measurement Result: Effect of Fiber Bend

Since the discrepancy between the prediction and the measurement results was quite a large, we speculated that the MCF might be heavily longitudinally-perturbed, and the fiber bend is the source of the perturbation. To discuss the effect of the bend perturbation on the XT, we employed the equivalent index model [33]. A bent fiber with a intrinsic refractive index profile n_{int} can be described as the corresponding straight fiber with the equivalent refractive-index profile n_{eq}:

$$n_{\mathrm{eq}}(r,\theta,R_{\mathrm{b}}) \approx n_{\mathrm{int}}(r,\theta)\left(1+\frac{r\cos\theta}{R_{\mathrm{b}}}\right), \qquad (r\cos\theta \ll R_{\mathrm{b}}), \tag{2.9}$$

where (r,θ) is the local polar coordinate in the cross-section of the fiber, $\theta = 0$ in radial direction of the bend, and R_{b} is the bending radius of the MCF. Thus, the equivalent effective index $n_{\mathrm{eff,eq},n}$ of Core n can be represented as

$$n_{\mathrm{eff,eq},n}(r,\theta,R_{\mathrm{b}}) \approx n_{\mathrm{eff}}(r,\theta)\left(1+\frac{r\cos\theta}{R_{\mathrm{b}}}\right), \qquad (r\cos\theta \ll R_{\mathrm{b}}). \tag{2.10}$$

Therefore, as shown in Fig. 2.8, the equivalent effective index of each core of the MCF can be varied by the bend and twist.

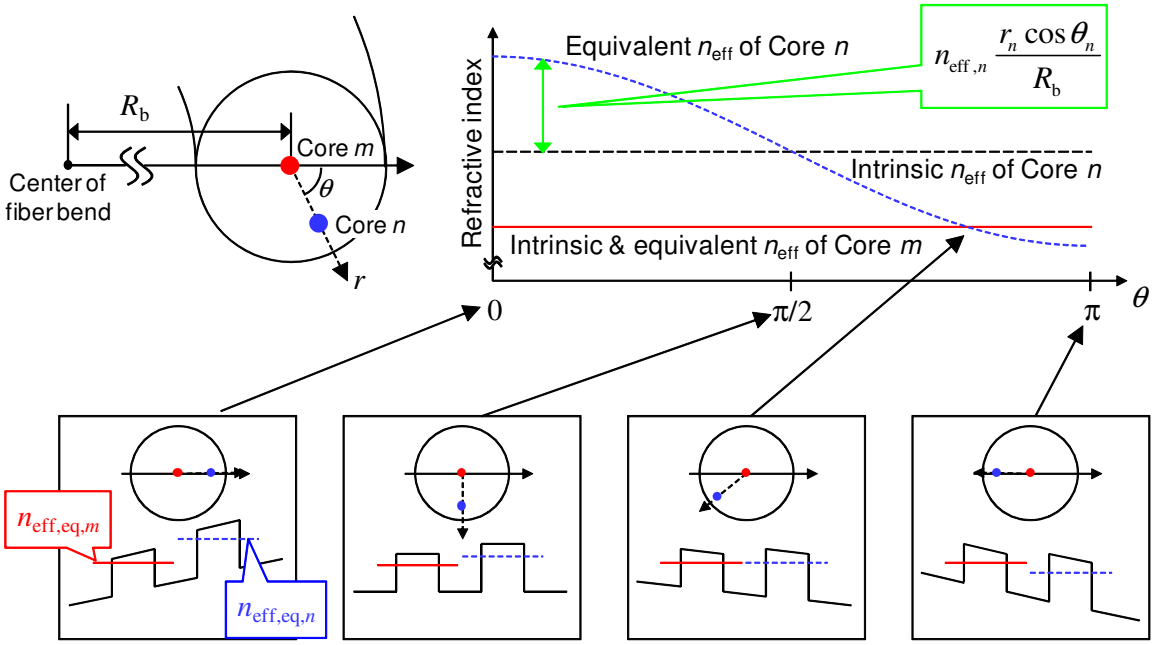

Fig. 2.8: Schematics of equivalent refractive index variation induced by bend and twist. The center of Core m is taken as the origin of the local coordinate for simple description.

The relative refractive index difference Δ_{eq} between the equivalent index and the intrinsic index can be obtained as

$$\Delta_{eq}(r,\theta,R_b) = \frac{n_{eq}^2(r,\theta,R_b) - n_{int}^2(r,\theta)}{2n_{eq}^2(r,\theta)} = \frac{2\frac{r\cos\theta}{R_b} + \left(\frac{r\cos\theta}{R_b}\right)^2}{2\left(1+\frac{r\cos\theta}{R_b}\right)^2} \tag{2.11}$$

$$\approx \frac{r\cos\theta}{R_b}, \qquad (r\cos\theta \ll R_b), \tag{2.12}$$

which is independent of n_{int}. Figure 2.9 shows the relationship between $r\cos\theta$, R_b, and Δ_{eq}, calculated from Eq. 2.11. Ref. [17] reported that the XT can be suppressed when the core pitch is larger than 30 μm and the difference of core Δ between neighboring cores is more than ±0.005%; however, Δ_{eq} exceeds 0.02% when r is larger than 30 μm even at the large R_b of 140 mm. Therefore, consideration on the bend perturbation is necessary for estimating the XT of the MCF.

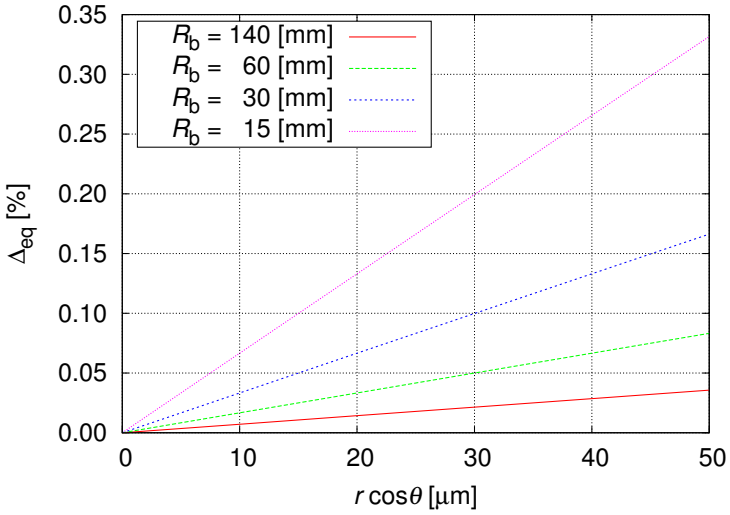

Fig. 2.9: The relationship between $r\cos\theta$, R_b, and Δ_{eq}.

Let R_{pk} be the threshold bending radius whether or not the difference between the equivalent effective indices of Core 1 and that of Core n can become zero, R_{pk} is the maximum radius where the difference of equivalent effective indices between Core 1 and Core n,

$$\delta n_{eff,eq} = n_{eff,1} - n_{eff,n}\left(1 + \frac{d_{1n}}{R_b}\cos\theta_n\right), \tag{2.13}$$

can have zero points; accordingly, R_{pk} can be obtained as

$$R_{\mathrm{pk}} = d_{1n} \frac{n_{\mathrm{eff},n}}{\left| n_{\mathrm{eff},1} - n_{\mathrm{eff},n} \right|}, \tag{2.14}$$

where d_{1n} represents the core pitch between Core 1 and Core n. Therefore, the XT is considered to degrade when the MCF is bent at a radius smaller than R_{pk}.

2.2.4 Experimental Trial for Crosstalk Suppression: Avoidance of the Phase Matching Induced by Fiber Bend

Based on the above discussion, we designed a new MCF (MCF-B) that have a large difference in the core diameters. MCF-B had the design that is basically the same with MCF-A but the diameter of the center core was thinned compared to MCF-A. The core diameters were designed to be 8.1 μm for the center core and to be 9.4 μm for the outer cores, so that the Δ between the effective indices of the center core and the outer cores was designed to be about 0.035%, and the R_{pk} was to be about 87 mm. Therefore, the XT of MCF-B was expected to be suppressed when MCF-B was wound on a 140-mm-radius bobbin.

Similarly to the fabrication of MCF-A, we drew three kinds of MCFs which has different cladding diameters from one preform; Table 2.2 shows the design properties of the MCF-B with three kinds of thickness. A cross-section of MCF-B30 is shown in Fig. 2.10.

Table. 2.2: Design properties of MCF-B.

		MCF-B26	MCF-B30	MCF-B34
Core Δ [%]		0.38		
Core pitch [μm]		26	30	34
Diameter [μm]	Center core	7.0	8.1	9.2
	Outer cores	8.1	9.4	10.7
	Cladding	108.3	125	141.7

The XT of MCF-B was measured in the same method described in Section 2.2.2. We measured the XT of 3.3-km-long MCF-B26, and 5-km-long MCF-B30 and MCF-B34. The MCFs were wound on 140-mm-radius bobbins. Figure 2.11 shows the measurement results. Compared with the case of MCF-A, the XT was suppressed, as we expected. When Core 1 was excited, the output powers did not converge to equilibrium even for the case of MCF-B26 (shortest core pitch and highest XT), although the XT of the kilometers-long MCFs were so high that the output powers converged to equilibrium in the case of MCF-A (Fig. 2.7c). In case of MCF-B34, the XT from Core 1 to the outer cores were less than −25 dB even after 5-km propagation.

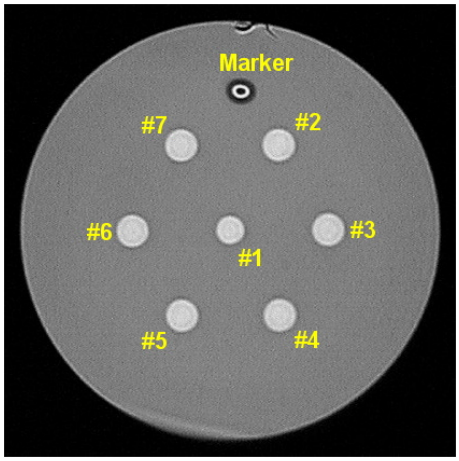

Fig. 2.10: A cross-section of the fabricated MCF-B30.

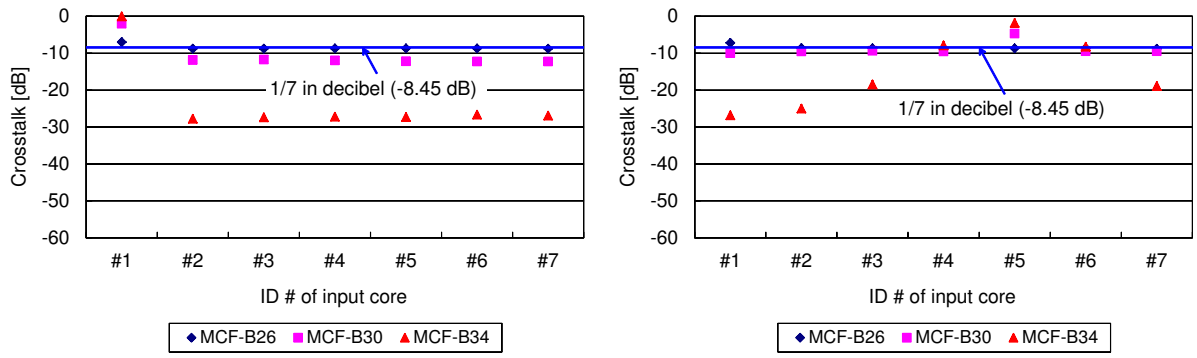

(a) Excited core: Core 1,
Fiber length: 3 km of MCF-B26,
5 km of MCF-B30,
5 km of MCF-B34.

(b) Excited core: Core 5,
Fiber length: 3 km of MCF-B26,
5 km of MCF-B30,
5 km of MCF-B34.

Fig. 2.11: Crosstalk of MCF-B wound on 140-mm-radius bobbin, measured at λ = 1550 nm.

2.2.5 The Dependence of the Crosstalk on Fiber Bend Radius

We investigated the dependences of the XT on R_b with the cases of MCF-A30 and MCF-B30, in detail. Table 2.3 shows the comparison of the design properties between MCF-A30 and MCF-B30.

Table. 2.3: Comparison of the design properties of MCF-A30 and MCF-B30.

		MCF-A30	MCF-B30
Core Δ [%]		0.38	
Core pitch [μm]		30	
Diameter [μm]	Center core	8.9	8.1
	Outer cores	9.4	
	Cladding	125	

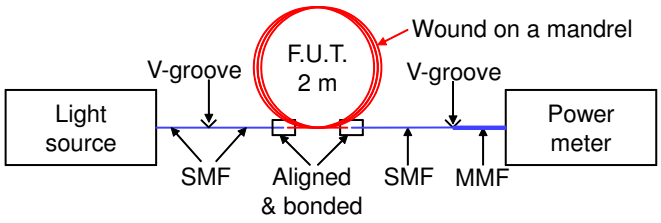

Fig. 2.12: The crosstalk measurement setup.

The measurement setup is shown in Fig. 2.12, which is slightly different from Fig. 2.6. Two single mode fibers (SMF) were aligned and bonded to the 2-m-long MCF with ultraviolet curable adhesive, to keep the bend radius R_{b} constant by winding the MCF on a mandrel from the end to end of the MCF. In this measurement, we dealt with the XT from Core 1 to an outer core, and Core 5 was taken as a representative of outer cores. So, the XT was defined to be the ratio of output power of Core 5 divided by that of Core 1 when Core 1 was excited. The radii of the mandrels were 40, 55, 76, 85, and 140 mm. The MCF was also twisted in order to avoid bias of bending effect due to a direction of core arrangement against a radial direction of the bend. The twist rate was four turns per two meters in this measurement. The XT was measured ten times repeatedly and each of the ten measurements was performed after the MCF was rewound, in order to average the measurement results, because we considered that the XT is a stochastic parameter, as described and shown in the following Section 2.2.6 and Fig. 2.14. Since we bonded the SMFs to the MCFs, the output power of Core 1 and that of Core 5 were not measured simultaneously, which did not affect the results because the output power of Core 1 was not affected by the XT, due to the low XT of the short MCF samples.

Relationships between the bending radius and the XT are shown in Fig. 2.13. Square plots represent average of ten times measurements and error bars indicate maximum and minimum values of the measurements. The results clearly demonstrated that the XT significantly depends on the bending radius and on the fiber structure.

2.2.6 Coupled-Mode Equation with Equivalent Index Model

In order to consider the measurement results quantitatively, we developed the simulation scheme based on the coupled-mode theory combined with the equivalent index model. Since the equivalent propagation constants are variable along propagation distance z, $\boldsymbol{E}$ can be expressed as

$$\boldsymbol{E} = \exp[-j\boldsymbol{\phi}(z)]\boldsymbol{A}, \tag{2.15}$$

$$\boldsymbol{\phi}(z) = \int_0^z \boldsymbol{\beta}_{\mathrm{eq}}\left(z'\right) dz', \tag{2.16}$$

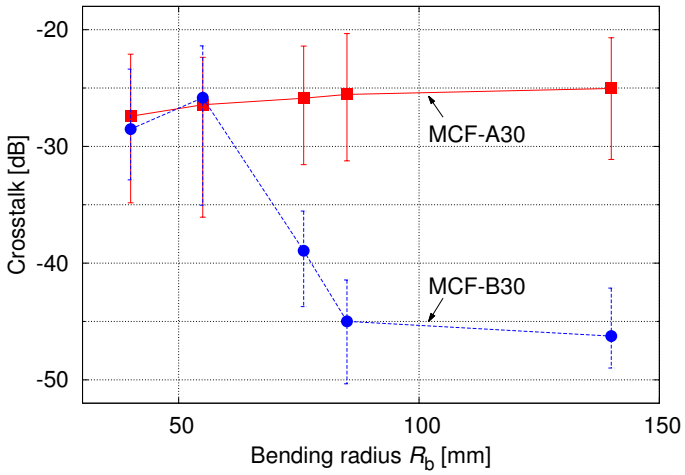

Fig. 2.13: Dependences of the measured crosstalk on fiber bend radius

where $\boldsymbol{\phi} = \mathrm{diag}\,(\phi_1, \phi_2, \ldots, \phi_N)$ and $\boldsymbol{\beta}_{\mathrm{eq}} = \mathrm{diag}\left(\beta_{\mathrm{eq},1}, \beta_{\mathrm{eq},2}, \ldots, \beta_{\mathrm{eq},N}\right)$ are the $N \times N$ diagonal matrices which include the accumulated phases ϕ_n and the equivalent propagation constants $\beta_{\mathrm{eq}} = (2\pi/\lambda) n_{\mathrm{eff,eq}}$ of each core, respectively. Therefore, Eq. 2.1 can be rewritten as

$$\frac{d\boldsymbol{A}}{dz} = -j \exp\left[j\boldsymbol{\phi}(z)\right] \boldsymbol{\kappa} \exp\left[-j\boldsymbol{\phi}(z)\right] \boldsymbol{A}. \tag{2.17}$$

Thus, a component of Eq. 2.5 is represented as

$$\frac{dA_n}{dz} = \sum_m -j\kappa_{nm} \exp\left\{j\left[\phi_n(z) - \phi_m(z)\right]\right\} A_m. \tag{2.18}$$

In the case of the fabricated MCFs, Eq. 2.16 can be expressed as

$$\phi_n(z) = \begin{cases} \beta_{\mathrm{int},1} z, & (n = 1), \\ \displaystyle\int_0^z \beta_{\mathrm{int},n} \left[1 + \frac{d}{R_{\mathrm{b}}} \cos\theta_n\left(z'\right)\right] dz', & (n = 2, \ldots, 7), \end{cases} \tag{2.19}$$

where β_{int} is the intrinsic propagation constant. For the experiments described in Section 2.2.5, $\theta_n(z)$ can be expressed as

$$\theta_n(z) = 2\pi f_{\mathrm{twist}} z + (n-2)\frac{\pi}{3} + \theta_{\mathrm{offset}}, \qquad (n = 2, \ldots, 7), \tag{2.20}$$

where f_{twist} is the twist rate [turns/unit length], and θ_{offset} the offset of the twist angle at $z = 0$.

Figure 2.14 shows an example of longitudinal variations of $\delta n_{\mathrm{eff,eq}}$ and the coupled power, or $|A_n|^2$, in the case

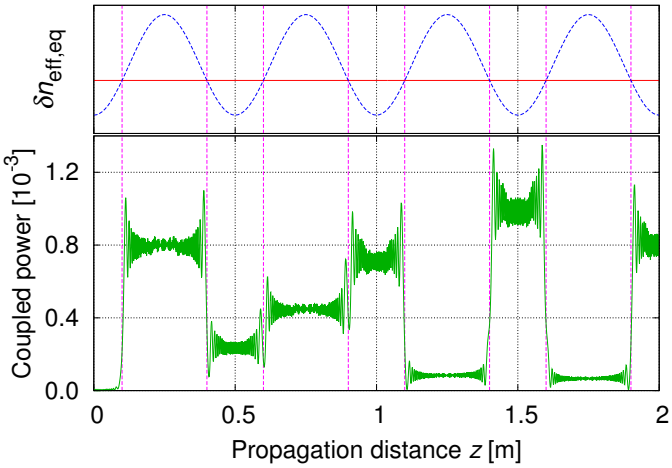

Fig. 2.14: An example of longitudinal variations of simulated coupled power and the difference of the equivalent effective indices $\delta n_{\mathrm{eff,eq}}$.

where MCF-A30 is bent at a radius of 76 mm and twisted at f_{twist} of 2 turns/m. The evolution of the coupled power was numerically calculated using Eqs. 2.18–2.20. Discrete-like dominant changes are observed eight times at zero points of $\delta n_{\mathrm{eff,eq}}(z)$—that is, the phase-matching points— along the propagation distance. These dominant changes look like random because phase differences between Core 1 and Core n,

$$\delta\phi_{n1}(z) = \phi_n(z) - \phi_1(z), \tag{2.21}$$

are different for every phase-matching point. The phase difference variation is deterministic in the simulation but can be easily fluctuated in practice by slight fluctuations of parameters such as the bending radius, the propagation constants, and the twist rate. Therefore, the XT variations at every phase-matching point are stochastic variations practically. In order to take account of such randomness, we introduced random phase shifts into the simulation. The random phase shifts are applied to all cores at every midpoint between the phase-matching points. In the case of the measurements in this chapter, it means that $\phi_n(z)$ of all cores are fluctuated individually in a random manner at every point where $\theta_n(z)$ of any core is a multiple of π.

In this theoretical scheme, distributions of the XT, or $|A_n|^2/|A_1|^2$, were obtained by Monte Carlo simulation. Each distribution contains the XT values from Core 1 to Cores 2–7 over 100 instances. Comparisons between the measured and the simulated XT are shown in Fig. 2.15. Averages and variations of the measured values are plotted as points and error bars. Averages and maximums of the simulated XT are plotted as solid and dashed lines respectively. Lines for minimum values are not plotted because the values can take zero. Lines of R_{pk} are also plotted in Fig. 2.15. The values of R_{pk} of MCF-A30 and MCF-B30 were calculated to be 245 mm and 65 mm

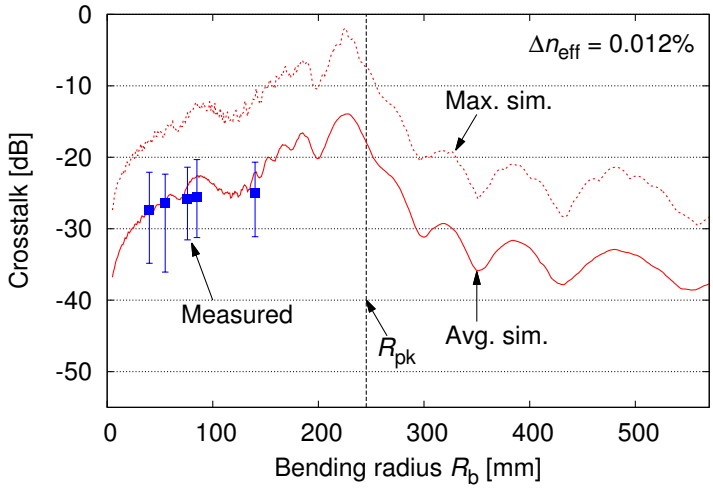

(a) MCF-A30

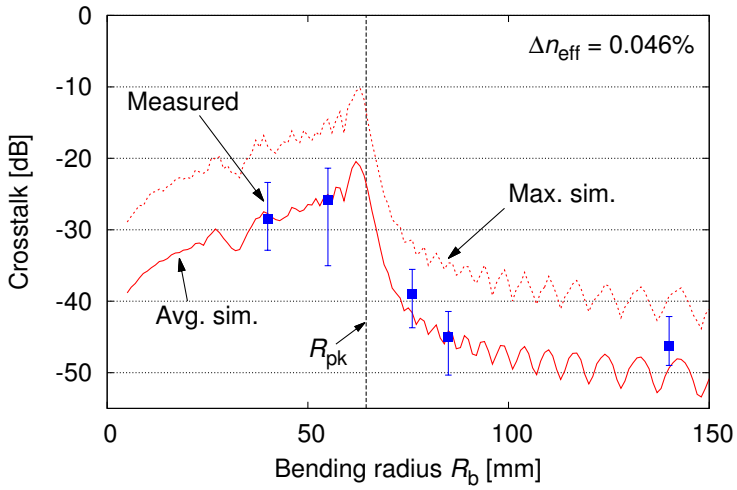

(b) MCF-B30

Fig. 2.15: Comparisons between the measured and simulated crosstalk of the fabricated MCFs.

respectively using the full-vectorial FE-ID-BPM [32], from refractive index profiles of the fabricated MCF-A30 and MCF-B30 measured with the refracted near field measurements. Δn_{eff} stands for a relative index difference of effective indices between Core 1 and Cores 2–7. From the measured refractive indices, the mode-coupling coefficients were calculated as κ_{1n} = 1.29 [/m], κ_{n1} = 1.78 [/m], and κ_{nm} = 2.23 [/m] for MCF-A30; and κ_{1n} = 0.36 [/m], κ_{n1} = 1.43 [/m], and κ_{nm} = 0.94 [/m] for MCF-B30, where Core n and Core m are the neighboring outer cores[*1]. The measured and the simulated XT are observed to have a good agreement; therefore, the theoretical

[*1] The reciprocity ($\kappa_{n1} = \kappa_{1n}$) of the mode-coupling coefficients are required for the power conservation, but the non-reciprocities in these simulations did not induce significant effects on the results shown in Fig. 2.15, because the XT was low enough. The non-reciprocities

scheme was validated.

So far, we dealt with MCFs twisted at 2 turns/m. In order to check the dependence of the XT distribution on the twist rate, distributions of the XT of MCF-A30 at R_b of 76 mm are shown in Fig. 2.16 in cases of several twist rates. From the simulated distributions, it is observed that a difference of the twist rate does not induce a significant difference on the XT distribution if the fiber is twisted at least 2 turns in total. From the measured distributions, the XT distribution is also observed to be independent of the twist rate. A discrepancy between simulated and measured distribution especially in the case of 1 turn per 2 meters is considered to be due to the lack of the number of the discrete-like random couplings, which occur at every phase-matching point. XT independence on the twist rate is also affirmed in several conditions other than the case of Fig. 2.16. Even in the case of a fiber which is not intentionally twisted, the fiber may be twisted randomly and sufficiently in actual if the fiber is adequately long. Therefore, this simulation may be applicable to the general case.

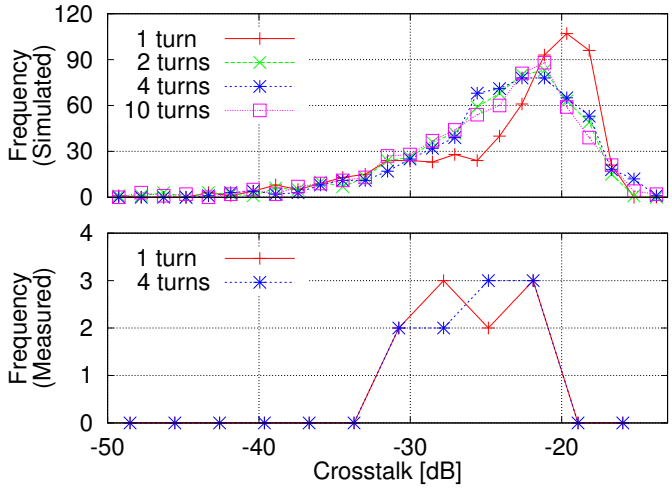

Fig. 2.16: Comparison of the statistical distributions of the crosstalk, between the measurements and the simulations.

2.2.7 Design and Fabrication of a Low-Crosstalk Heterogeneous MCF, Taking Account of the Bend Effect

Based on the validated theoretical scheme, we designed and fabricated a heterogeneous MCF—MCF-C— where all pairs of neighboring cores are dissimilar, as shown in Fig. 2.17. The XT of MCF-C were expected to be suppressed between the all neighboring cores.

MCF-C was designed based on MCF-B. The diameter of the center core was 8.1 μm, and that of Cores 2, 4, and

between κ_{n1} and κ_{1n} in this calculation was mainly due to the improper treatment of the measured refractive index profiles—especially of the (measurement) fluctuations in the cladding. However, when the coupled cores are dissimilar, the reciprocity of $\kappa_{n1} = \kappa_{1n}$ cannot completely holds even if the measured index profiles are properly treated, because the coupled-mode expressions are just an approximation of the exact solution of the Maxwell's equations. A coping technique to this problem is reviewed in Section 6.2.

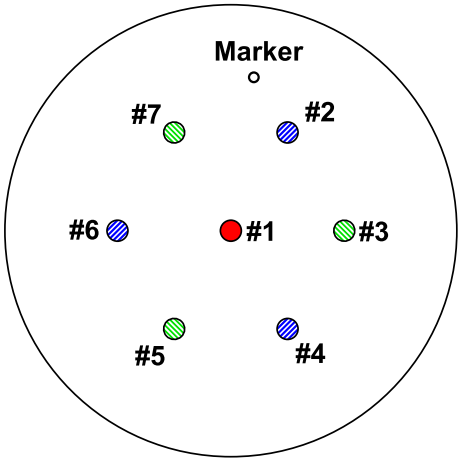

Fig. 2.17: Schematic cross-section of the designed heterogeneous MCF.

6 was 9.4 μm, which were the same with MCF-B. The only difference is the diameter of Cores 3, 5, and 7, which was designed to be 7.0 μm. Δ between the effective indices of the center core and "Cores 3, 5, and 7" was designed to be more than 0.035%, and the R_{pk} was to be less than 87 mm. Therefore, the XT of MCF-C was expected to be suppressed when MCF-C was wound on a 140-mm-radius bobbin, as with MCF-B.

We drew two kinds of MCFs which has different cladding diameters from one preform; Table 2.4 shows the design properties of the MCF-C with two kinds of cladding diameters. A cross-section of MCF-C30 is shown in Fig. 2.18. We can observe the differences of the diameters of three kinds of cores.

The XT of MCF-C was measured in the same method described in Section 2.2.2. Figure 2.19 shows the measurement results. We measured the XT of 5-km-long MCF-C30 and MCF-C34. The MCFs were wound on 140-mm-radius bobbins. The XTs from the center core to the outer cores of MCF-C30 were higher than those of MCF-B30, though the designs of MCF-B30 and MCF-C30 are the same except the diameters of Cores 3, 5, and 7. This is caused by unintended variations of core structures. In the case of MCF-B30, the refractive index of the cladding was not flat and higher at around the outer cores—that is, the larger the core diameter was, the higher the surrounding cladding index was. Accordingly, the difference in the effective indices between the cores of the

Table. 2.4: Design properties of MCF-C.

		MCF-C30	MCF-C34
Core Δ [%]		0.38	
Core pitch [μm]		30	34
Diameter [μm]	Center core	8.1	9.2
	Cores 2, 4, 6	9.4	10.7
	Cores 3, 5, 7	7.0	7.9
	Cladding	125	141.7

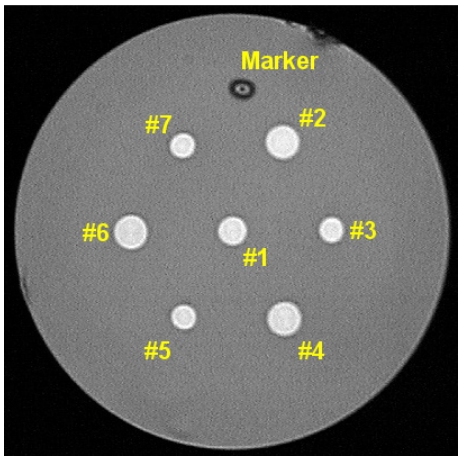

Fig. 2.18: A cross-section of the fabricated MCF-C30.

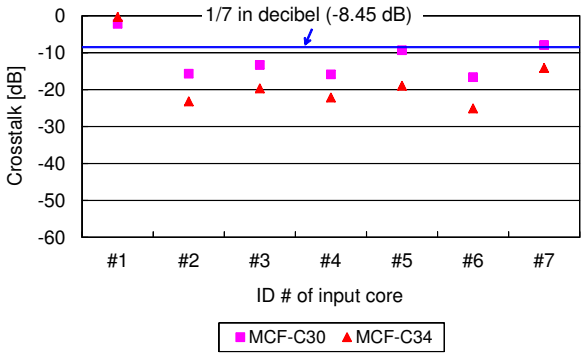

(a) Excited core: Core 1,
Fiber length: 5 km.

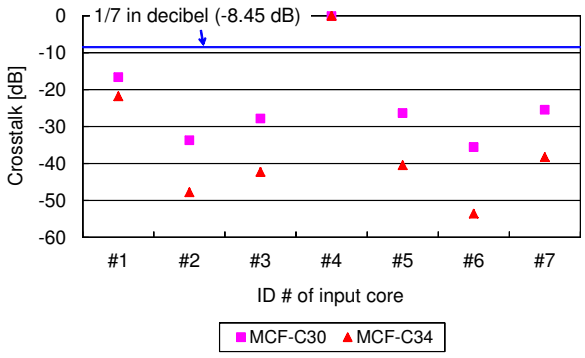

(b) Excited core: Core 4,
Fiber length: 5 km.

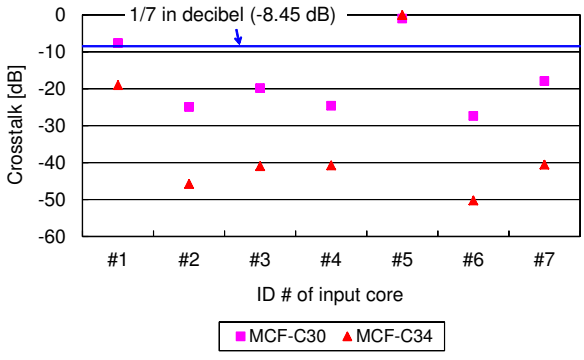

(c) Excited core: Core 5,
Fiber length: 5 km.

Fig. 2.19: Crosstalk of MCF-C wound on 140-mm-radius bobbin, measured at λ = 1550 nm.

fabricated MCF-B30 was larger than that of the designed MCF-B30. On the other hand, in the case of MCF-C30, there were no such index variation in the cladding. Because of this, actual R_{pk} of MCF-B became smaller than that of MCF-C, and the XTs from the center core to the outer cores of MCF-C were higher than those of MCF-B, at R_b = 140 mm. However, the XT between the neighboring outer cores of MCF-C were successfully suppressed, compared with MCF-B.

In the case of MCF-C34, values of the XT between the center core and outer cores after 5-km propagation were about -20 dB, and the values between the neighboring outer cores were around -45 dB. The latter values are smaller than the former values because the differences of core diameters, or effective indices, between neighboring cores were larger in the latter case.

Table 2.5 shows the measured optical properties of representative cores of MCF-C34. Sakaguchi *et al.* conducted a transmission experiment using MCF-C34 by leveraging its low XT characteristics, and investigated signals that were simultaneously multiplexed in space and wavelength divisions for the first time, as reported in Refs. [34].

Although the XT was suppressed in MCF-C34, the optical properties were very different between the neighboring cores for inducing large difference in the effective indices.

Table. 2.5: Measured optical properties of three representative cores of MCF-C34.

	Attenuation [dB/km]	MFD [μm]	A_{eff} [μm^2]	λ_{cc} [nm]	Chromatic dispersion [ps/(nm · km)]	Dispersion slope [ps/(nm^2 · km)]	PMD [ps/km$^{1/2}$]
Core 1	0.212	10.1	80.4	1362	17.5	0.056	0.025
Core 4	0.199	10.6	91.4	1523	19.4	0.058	0.018
Core 5	0.194	9.9	75.9	1147	14.7	0.054	0.043

2.3 Loss Degradation in the Outermost Cores

During the basic study on the XT, we found the loss of the outer cores of the MCF can degrade in some cases. In this section, we reveal the mechanism of this loss degradation.

After the fabrication of MCF-C, we designed and fabricated a new MCF (MCF-D45) with larger core pitch, in order to suppress the XT further from MCF-C34. Table 2.6 shows the comparison of the design properties between MCF-C34 and MCF-D45. The core pitch of MCF-D45 was enlarged to 45.3 μm from that of MCF-C34. The core diameters of MCF-D45 were adjusted to keep "the Δ between the equivalent effective indices of neighboring cores" more than 0.01%, even with the core pitch of 45.3 μm and in the bent condition (R_b = 140 mm).

Table. 2.6: Comparison of design properties between MCF-C34 and MCF-D45.

		MCF-C34	MCF-D45
Core Δ [%]		0.38	
Core pitch [μm]		34	45.3
Diameter [μm]	Center core	9.2	9.7
	Cores 2, 4, 6	10.7	11.8
	Cores 3, 5, 7	7.9	8.2
	Cladding	141.7	

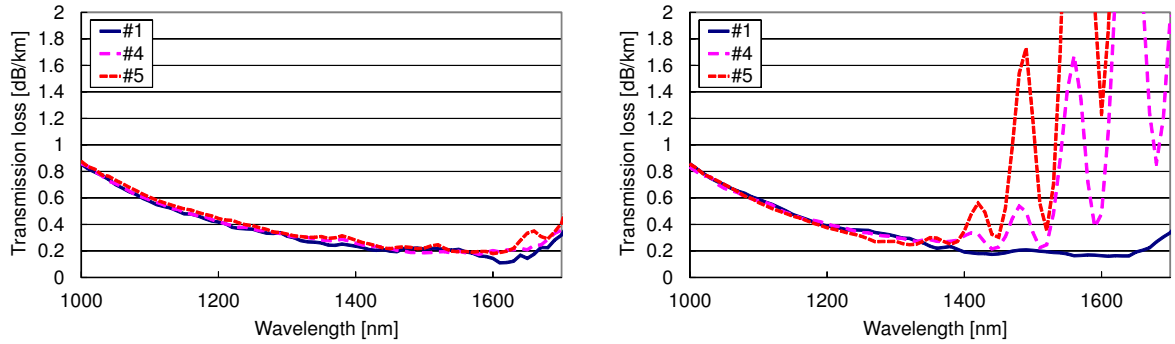

(a) MCF-C34.

(b) MCF-D45.

Fig. 2.20: Measured transmission-loss spectra of MCF-C34 and MCF-D45. Note that the transmission loss was measured using the cut-back method, and output powers from *all cores* were received with a MMF whose core diameter was 105μm.

However, we observed loss degradations in outer cores of MCF-D45. Figure 2.20 shows the transmission loss spectra of MCF-C34 and MCF-D45, which were measured with cut-back method.[*2] The MCFs were wound on 140-mm-radius bobbins. It was clearly observed that the loss values of Cores 4 and 5 of MCF-D45 rapidly increased with the elongation of the wavelength.

The reason of the loss degradation can be explained as follows. Figure 2.21 shows a schematic illustration of a refractive index profile, including a polymer coating layer, of a MCF. The refractive index of the coating is generally much higher than that of silica glass, in order to suppress the propagations of the cladding modes. Therefore, if the outer cores of the MCF is too close to the coating, the power guided in the outer core can be coupled to the leaky modes of the coating, and thus the loss values of the outer cores can be degraded. Figure 2.22 shows comparisons of the measured loss degradations and the calculated loss values of the outer cores induced

[*2] Because we were not able to conduct on-site alignments during the cut-back measurements at the moment of this experiment, output powers from *all cores* were received using a MMF whose core diameter was 105μm. Therefore, the results were slightly affected by the multi-path interference (MPI) due to the XT and the all-core receiving. For example, the fluctuations of the measured loss values around λ = 1600 nm in Fig. 2.20a may be explained by the effect of the MPI. However, the measured transmission loss values basically represent the transmission loss values of excited cores, because the XTs in MCF-C34 and MCF-D45 were low.

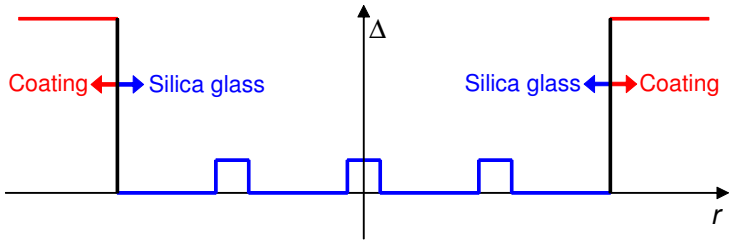

Fig. 2.21: Schematic illustration of a refractive index profile, including a polymer coating layer, of a MCF.

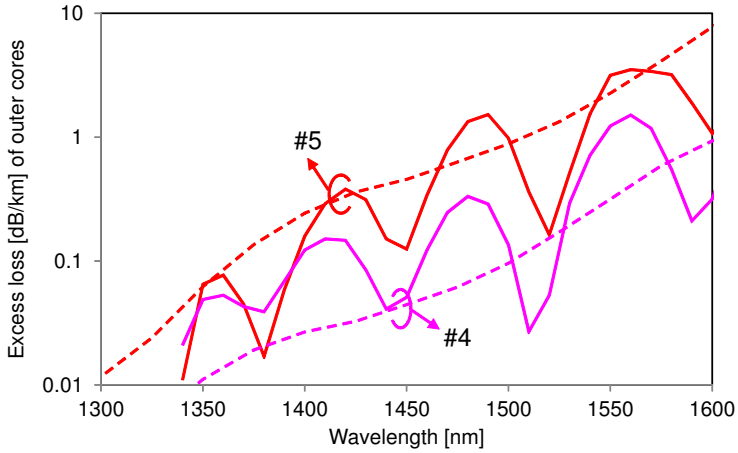

Fig. 2.22: Comparisons of the measured loss degradations and the calculated leakage loss values of the outer cores. Solid lines: the measured loss degradations of the outer cores. Dashed lines: the calculated leakage losses due to the coupling to the coating.

by the leakage to the coating. Solid lines represent the measured loss degradations of the outer cores estimated from the difference between the transmission loss values of the outer cores and those of the center core. Dashed lines represent the leakage loss to the coating, which were calculated in the case of R_b = 140 mm by using the full-vectorial FE-ID-BPM [32]. The measured and calculated loss degradations were in good agreement. The oscillations of the actual degraded loss of Cores 4 and 5 can be considered to be caused by the MPI between the core modes and the so-called "whispering gallery modes [35–37]." Figure 2.23 shows the schematic illustration of the propagation of a whispering gallery mode reflected by the interface between the secondary coating and air. d_{couple} is the distance from the core center to the radial position where the power guided in the core couples to the leaky modes, which can be the position where the effective index of the core equals to the equivalent index of the cladding in the case of bent fiber, or the position of the cladding–coating interface when the core is too close to the coating. The light coupled to the leaky mode can be reflected by the interfaces between the different materials and couples to the core mode again. Thus, the core mode and the whispering gallery modes forms Mach–Zehnder interferometers, and the optical path length differences between them induce the interference pattern. On the

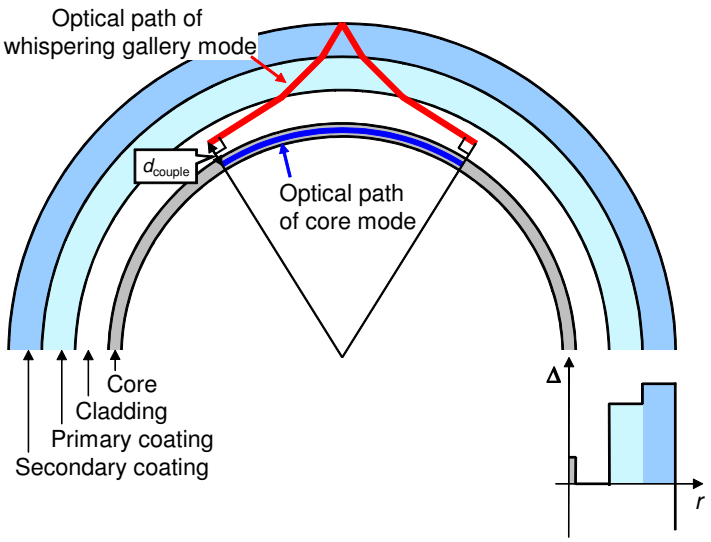

Fig. 2.23: Optical paths of the core mode and a whispering gallery mode in a bent fiber.

other hand, there were no interference pattern in the calculated loss degradation in Fig. 2.22, because the perfectly matched layer (PML) was implemented in the circumference of the primary coating and no leaked power was reflected.

We also calculated the leakage loss of MCF-C34, which were less than 1/100 of those of MCF-D45. This also agrees with the measurement results, as no significant loss difference was observed in MCF-C34.

2.4 Conclusion of This Chapter

We revealed the inter-core XT of the MCF is heavily dependent not only on the fiber structure but also on the fiber bend, from the theoretical and experimental studies. It was also revealed that the XT is a stochastic value.

We also found that the loss values of outer cores of a MCF can be degraded if the outer cores are too close to the coating, because the powers guided in the cores can couple to the coating with high refractive index.

Taking care about the bending effect on the XT and about the stochasticity of the XT is necessary for designing a solid MCF. We need to design MCFs with considerations on the effect of the fiber bend on the XT, and on the effect of “the distance between the outer cores and the cladding–coating interface” on the loss degradation, in order to suppress the degradations specific to the MCF.

Chapter 3

Ultra-Low-Crosstalk Multi-Core Fiber Utilizing Fiber Bend

3.1 Introduction to This Chapter

Based on the effect of the fiber bend on the crosstalk (XT), which was revealed in Section 2.2, careful management of the bend is necessary in heterogeneous MCFs that have only slight differences in the effective indices between cores. Furthermore, very large differences in core structures are necessary for suppressing the XT when the MCF is wound on a commonly used bobbin whose winding radius ranges from 70 to 150 mm. If the XT is not suppressed for MCFs wound on bobbins, then the optical properties of each core of the MCFs may be affected by the XT, and characteristics measurements may not be performed precisely. The MCFs may also be bent at such radii around their connection and splice points. To prevent the XT degradation in such bent condition, large differences in the core structures are needed, and accordingly, the optical properties of each core have to be largely different from one another. However, the existence of some kinds of cores in the MCF can make the management of transmission lines more complicated and difficult.

Therefore, we proposed to utilize the phase mismatch induced by the bend for suppressing the XT in homogeneous MCF in which the optical properties of each core of the MCF are the same. This chapter describes the theoretical aspect of the XT suppression by utilizing the fiber bend, and its demonstration by the design and fabrication of a homogeneous MCF. The method for precisely measuring the statistical properties of ultra-low XT was also developed for the demonstration.

3.2 Crosstalk Suppression by Utilizing Fiber Bend

In the conventional simple coupled-mode theory, the effective indices of the identical cores are the same and constant, as shown in Fig. 3.1a. However, the equivalent effective indices are affected by the bend also in the homogeneous MCF, as with the heterogeneous MCF, as shown in Fig. 3.1b (see also Fig. 2.8). Therefore, the XT in the homogeneous MCF is also affected by the bend. In the case of the bent homogeneous MCF, the XT can change

dominantly at every phase-matching point, as with the case of Fig. 2.14. We can consider that these discrete-like dominant changes of the XT occur not only at the phase-matching *point*—where the equivalent effective index of one core equals to that of another core— but also at phase-matching *region*—where the equivalent effective index of one core *nearly* equals to that of another core. Therefore, we can speculate that the decreasing of R_b enlarges the bend-induced variation of equivalent index difference and shortens the total length of phase-matching regions of MCF, and thus that the bend can be utilized for the XT suppression of homogeneous MCFs.

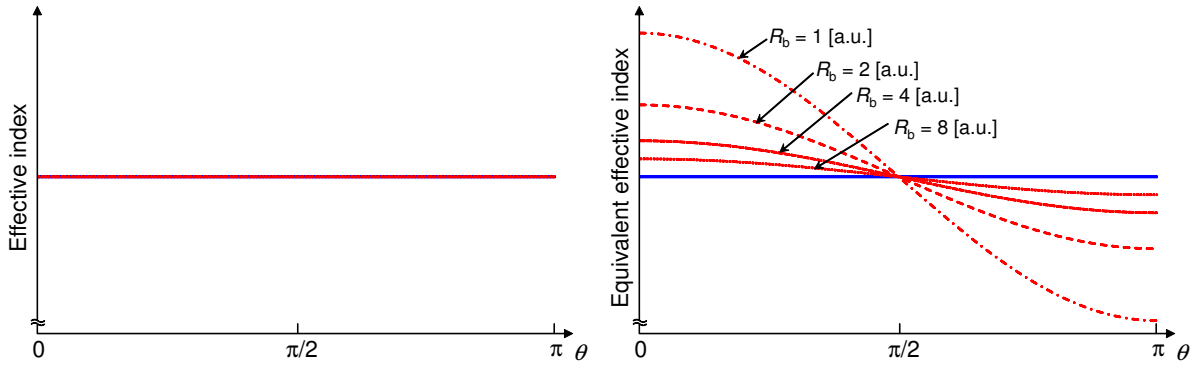

(a) Intrinsic effective indices.

(b) Equivalent effective indices.

Fig. 3.1: The relationship between the bend radius R_b, the twist angle θ, and the (equivalent) effective indices in the homogeneous MCF. Blue solid line: the index of the center core, red non-solid lines: the index of a non-center core. All lines are overlapped in the case of the intrinsic effective indices.

3.3 Approximation Model for Longitudinal Crosstalk Evolution Based on the Coupled-Mode Theory with Equivalent Index Model

Before we design a low-crosstalk homogeneous MCF, we discuss how the XT evolve stochastically and derive an expression for statistical mean of the XT, for setting a target level of the XT and for estimating the XT of designed MCFs, without the simulation described in Section 2.2.6.

Here, we consider the XT between two cores, for simplicity. To deal with the stochastic evolution of the XT, we approximate the dominant XT changes shown in Fig. 2.14 by the following discrete changes:

$$\begin{aligned} A_{n,N} &= A_{n,N-1} - jK_{nm,N}\exp\left[j\phi_{\mathrm{rnd},nm,N}\right]A_{m,N-1} \\ &= A_{n,0} - j\sum_{k=1}^{N} K_{nm,k}\exp\left[j\phi_{\mathrm{rnd},nm,k}\right]A_{m,k-1}, \end{aligned} \tag{3.1}$$

where $A_{n,N}$ represents the complex amplitude of Core n after the N-th phase-matching point, $K_{nm,N}$ the coupling coefficient for the *discrete changes* caused by the mode coupling from Core m to Core n at the N-th phase-matching

point, and $\phi_{\mathrm{rnd},nm,N}$ the phase difference between Core m and Core n at the N-th phase-matching point. We assume $\phi_{\mathrm{rnd},nm,N}$ as a random number, because it significantly varies with slight variations in the bend radius, twist rate of the fiber, among others. In case where only Core m is excited ($A_{m,0}=1$, $A_{n,0}=0$) and the XT is adequately low ($|A_{n,N}| \ll 1$), the approximation that $A_{m,N} \approx A_{m,0} = 1$ holds, and the XT value X can be approximated to be $|A_{n,N}|^2$. Therefore, Eq. 3.1 can be approximated as

$$A_{n,N} \approx -j \sum_{k=1}^{N} K_{nm,k} \exp\left[j\phi_{\mathrm{rnd},nm,k}\right]. \tag{3.2}$$

When ϕ_{rnd} is uniformly distributed over 0–2π radians, $\Re[K_{nm}\exp(j\phi_{\mathrm{rnd})}]$ and $\Im[K_{nm}\exp(j\phi_{\mathrm{rnd})}]$ have a probability distribution of the arcsine distribution:

$$f(x) = \frac{1}{\pi\sqrt{|K_{nm}|^2 - x^2}}, \tag{3.3}$$

and their variances become $|K_{nm}|^2/2$. $\Re[A_{n,N}]$ and $\Im[A_{n,N}]$ are the sums of $\Re[K_{nm}\exp(j\phi_{\mathrm{rnd})}]$ and $\Im[K_{nm}\exp(j\phi_{\mathrm{rnd})}]$, respectively, for all phase-matching points from first to N-th point. If ϕ_{rnd} have no correlation between the phase-matching points and N is adequately large, from the central limit theorem, the probability density function (PDF) of $\Re[A_{n,N}]$ and $\Im[A_{n,N}]$ converge to the normal distribution whose variance $\sigma_{2\mathrm{df}}^2$ is $\sum|K_{nm}|^2/2$. Based on that the PDF of l random numbers, whose PDFs are the standard normal distribution, is the chi-square distribution with l degrees of freedom (df), the PDF of the XT $X(\approx |A_{n,N}|^2 = \Re[A_{n,N}]^2 + \Im[A_{n,N}]^2)$ be expressed as

$$f(X) = f_{2\mathrm{df}}\left(\frac{X}{\sigma_{2\mathrm{df}}^2}\right)\left|\frac{d}{dX}\left(\frac{X}{2\sigma_{2\mathrm{df}}^2}\right)\right| = \frac{1}{2\sigma_{2\mathrm{df}}^2}\exp\left(-\frac{X}{2\sigma_{2\mathrm{df}}^2}\right), \tag{3.4}$$

and its cumulative distribution function (CDF) is

$$F(X) = F_{2\mathrm{df}}\left(\frac{X}{\sigma_{2\mathrm{df}}^2}\right) = 1 - \exp\left(-\frac{X}{\sigma_{2\mathrm{df}}^2}\right), \tag{3.5}$$

where $f_{l\mathrm{df}}(x)$ is the chi-square distribution with l df, and $F_{l\mathrm{df}}(x)$ is the CDF corresponding to $f_{l\mathrm{df}}(x)$.

The above discussion assumes single polarization, or no polarization mode coupling; however, generally, polarization modes randomly couple and are not preserved in actual fiber. Consequently, the coupled power can be statistically distributed equally between the two polarization modes. Therefore, the variances $\sigma_{4\mathrm{df}}^2$ in $\Re[A_{n,N}]$ and $\Im[A_{n,N}]$ of the two polarization modes can be obtained as $\sum|K_{nm}|^2/4$ Since X is the sum of the powers of $\Re[A_{n,N}]$

and $\Im[A_{n,N}]$ of the two polarization modes, the PDF of X, or the XT distribution, can be expressed as

$$f(X) = f_{4\mathrm{df}}\left(\frac{X}{\sigma_{4\mathrm{df}}^2}\right)\left|\frac{d}{dX}\left(\frac{X}{\sigma_{4\mathrm{df}}^2}\right)\right| = \frac{X}{4\sigma_{4\mathrm{df}}^4}\exp\left(-\frac{X}{2\sigma_{4\mathrm{df}}^2}\right), \tag{3.6}$$

and its cumulative distribution function (CDF) is

$$F(X) = F_{4\mathrm{df}}\left(\frac{X}{\sigma_{4\mathrm{df}}^2}\right) = 1 - \left(1 + \frac{X}{2\sigma_{4\mathrm{df}}^2}\right)\exp\left(-\frac{X}{2\sigma_{4\mathrm{df}}^2}\right). \tag{3.7}$$

Irrespective of whether the polarization modes are preserved or randomly couple, the ensemble average (mean) μ_X of X—i.e., the mean XT— can be obtained as

$$\mu_X = 2\sigma_{2\mathrm{df}}^2 = 4\sigma_{4\mathrm{df}}^2 = \sum_{k=1}^{N}\left|K_{nm,k}\right|^2. \tag{3.8}$$

Especially in case where the cores have identical structures and the MCF is bent at a constant radius and twisted continuously at a constant rate $\omega_{\mathrm{twist}} = 2\pi f_{\mathrm{twist}}$ [radians/unit length], Eq. 3.8 can be rewritten as

$$\mu_X = N\left|K_{nm}\right|^2, \tag{3.9}$$

and $|K|$ can be analytically derived as follows (see Appendix 3.A):

$$|K_{nm}| = |K_{mn}| = |K| = \sqrt{\frac{\kappa^2}{\beta_{\mathrm{int}}}\frac{R_{\mathrm{b}}}{d_{nm}}\frac{2\pi}{\omega_{\mathrm{twist}}}} = \sqrt{\frac{\kappa^2}{\beta_{\mathrm{int}}}\frac{R_{\mathrm{b}}}{d_{nm}}\frac{1}{f_{\mathrm{twist}}}}, \qquad (\kappa_{nm} = \kappa_{mn} = \kappa). \tag{3.10}$$

Therefore, Eq. 3.8 can be obtained as

$$\mu_X = \kappa_{nm}^2\frac{2R_{\mathrm{b}}}{\beta_{\mathrm{int}}d_{nm}}L = \kappa_{nm}^2\frac{\lambda R_{\mathrm{b}}}{\pi n_{\mathrm{eff}}d_{nm}}L, \tag{3.11}$$

where L is the fiber length, and we assumed $N = 2f_{\mathrm{twist}}L$. In this case, the power-coupling coefficient H of the homogeneous MCF can be expressed as

$$H = \kappa_{nm}^2\frac{2R_{\mathrm{b}}}{\beta_{\mathrm{int}}d_{nm}} = \kappa_{nm}^2\frac{\lambda R_{\mathrm{b}}}{\pi n_{\mathrm{eff}}d_{nm}}. \tag{3.12}$$

The q-quantile of the distribution of X can be expressed as

$$X_q = \sigma_{l\mathrm{df}}^2 F_{l\mathrm{df}}^{-1}(q) = \frac{\mu_X}{l}F_{l\mathrm{df}}^{-1}(q), \tag{3.13}$$

$$X_q^{[\mathrm{dB}]} = 10\log_{10}\sigma_{l\mathrm{df}}^2 + 10\log_{10}F_{l\mathrm{df}}^{-1}(q) = 10\log_{10}\frac{\mu_X}{l} + 10\log_{10}F_{l\mathrm{df}}^{-1}(q), \tag{3.14}$$

where $F_{l\mathrm{df}}^{-1}$ is the inverse function of $F_{l\mathrm{df}}$. Based on Eq. 3.14, the shape of the XT distribution on the decibel scale is independent of the mean XT μ_X. For example, regarding the case of 4 df, the 0.9999-quantile of the XT distribution can be obtained by adding $\sim$7.69 dB to μ_X on the decibel scale.

Because the mean XT is linearly proportional to variance, and because the variance of the sum of statistically independent variables is the sum of the variances of the variables, the mean XT from multiple cores to a certain core can be represented as a sum of the mean XT from each of the multiple cores to the certain core. Accordingly, in a seven-core fiber whose cores are arranged in a hexagonal lattice, its center core is surrounded by six outer cores so that the mean XT of the center core is the worst and can be expressed as

$$\mu_{X,\mathrm{WC}} = 6HL = 6\kappa_{nm}^2\frac{\lambda R_\mathrm{b}}{\pi n_\mathrm{eff}\Lambda}L, \tag{3.15}$$

where Λ denotes the core pitch or the pitch of the lattice. Since the $\mu_{X,\mathrm{WC}}$ is proportional to the bend radius R_b and the fiber length L for the homogeneous MCF, a XT coefficient, which is defined as

$$\mathrm{XT}_\mathrm{coeff} \equiv \frac{\mu_{X,\mathrm{WC}}}{R_\mathrm{b}L} \propto \frac{H}{R_\mathrm{b}}, \tag{3.16}$$

can be employed as a performance factor of the XT of the homogeneous MCF.

It should be noted again that the equations in this section hold when the XT is adequately low.

3.4 Design of a Homogeneous Low-Crosstalk MCF

For the application for long-distance high-capacity networks, we designed a homogeneous seven-core fiber with the following conditions:

I. Attenuation of each core should be less than that of the standard single-mode fiber (SSMF),
II. Mode field diameter (MFD) of each core should range from 9.5 to 10.5 μm at λ= 1550 nm,
III. Cable cutoff wavelength (λ_cc) of each core should be less than 1530 nm,
IV. 0.9999-quantile of XT of the center core should be less than -30 dB after 100-km propagation at λ= 1625 nm and R_b< 200 mm,
V. Loss degradations of the outermost cores should be less than 0.001 dB/km.

The targets of the attenuation and MFD were determined so that the optical amplification noise and nonlinear interference noise in each core can be less than those of the SSMF, because these noises are important limiting factors for the transmission capacity in digital coherent transmissions [6]. The MFD target corresponds to an effective area (A_{eff}) of $\sim$80 μm^2. A larger A_{eff} decreases the nonlinearity, but weakens the confinement of power in each core, which makes the XT suppression difficult. Therefore, as a first step, we employed A_{eff} equivalent to that of SSMF and did not employ A_{eff} larger than 100 μm^2. The target of λ_{cc} was determined after ITU-T G.654 so that it is much longer than λ_{cc} of SSMF. We elongated λ_{cc} for improving the power confinement, because ultra-high-capacity transmissions had been demonstrated using only C- and L-bands (C+L band, i.e., 1530–1625 nm) [38–40], due to the limited bandwidths of the amplifiers and the relatively high attenuation of the other bands. The target of the XT was determined at λ = 1625 nm, by considering the application for the C+L band. Because longer wavelengths weaken the confinement, the XT increase in longer wavelength. The condition on R_{b} was determined so that low XT can be achieved when the MCF is wound on a bobbin. Of course, the loss degradation of the outer cores should be suppressed.

Various approaches, such as MCF with hole-assisted structures [41], may be adopted for suppressing the XT whilst keeping the other optical properties suitable for transmissions. In this study, we employed a trench-assisted profile (see Fig. 3.2), which is simple to fabricate and can reduce the mode-coupling coefficients while achieving the conditions on MFD and λ_{cc}. Table 3.1 lists the designed optical properties of each core at λ = 1550 nm. λ_{cc}

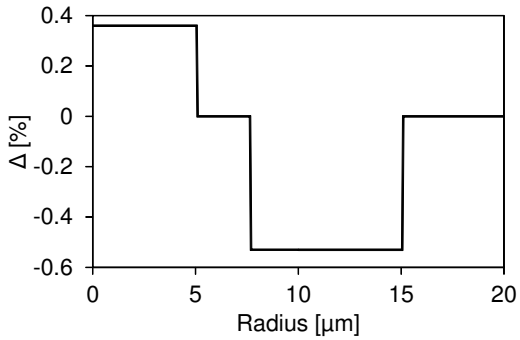

Fig. 3.2: Designed refractive index profile of each MCF core.

Table. 3.1: Designed optical properties of each MCF core at λ = 1550 nm.

Parameters	Designed value
λ_{cc}	1496 nm
MFD	9.86 μm
A_{eff}	79.6 μm^2
D_{chrom}	23.3 ps/(nm $\cdot$ km)
D_{chrom} slope	0.063 ps/(nm^2 $\cdot$ km)

and MFD were designed to meet the target conditions and A_{eff} was ∼80 μm^2. Chromatic dispersion D_{chrom} was moderately higher than that of conventional SMFs. The higher dispersion can induce larger phase mismatches between wavelength channels so that the nonlinear effects can be more suppressed [6, 42]. The dispersion slope was 0.063 ps/(nm^2 · km). We set the core pitch Λ to 45 μm, because the condition on the XT can be achieved at Λ > 39.2 μm for the designed core, as shown in Fig. 3.3.

The loss degradation of outer cores of MCFs was reported to be due to microbend loss [43, 44], and/or due to power coupling to the coating [45] induced by the high refractive index of the coating. However, as described in Section 2.3, we considered that the latter factor is the cause of the loss degradation. The microbend loss dependence on fiber diameter is induced by the change of fiber rigidity rather than that of cladding thickness [46–49]. Figure 3.4 shows the relationships between the cladding diameter and the loss degradation at R_{b} = 140 mm and λ = 1625 nm, which were simulated with the designed MCF structure in the case where the simulated outer

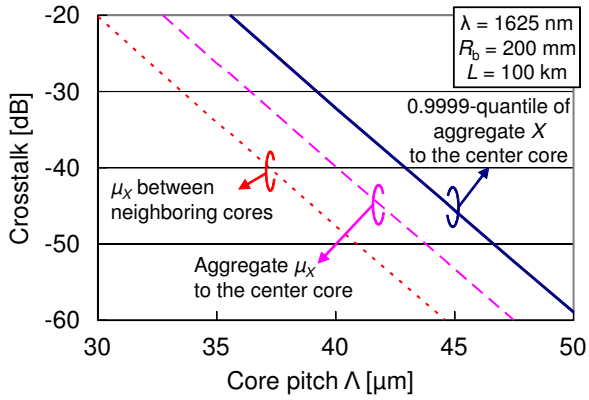

Fig. 3.3: Relationship between the core pitch Λ and the crosstalk for the designed core.

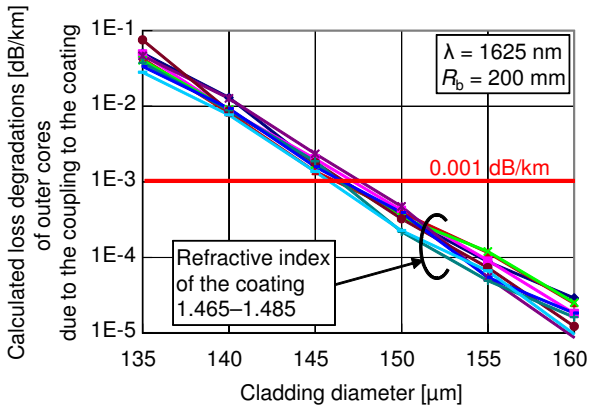

Fig. 3.4: Relationship between the cladding diameter and the loss degradation of the outer core for the designed MCF.

core is positioned at the outermost side of the bend. To meet Condition V, the cladding diameter was designed to be 150 μm so that the loss degradation of Cores 2–7 can be less than 0.001 dB/km. The calculation results in this section were obtained using a full-vector finite-element method [32].

3.5 Fabrication of the Designed MCF and Measurements of Optical Properties of Each Core

Based on the design, we fabricated MCF (MCF-E) with pure-silica cores for reducing the attenuation of each core. The cross-section of the MCF in Fig. 3.5 shows the seven trench-assisted cores and a marker for core identification. The actual core pitch, cladding diameter, and coating diameter were 45 μm, 150 μm, and 256 μm, respectively. The attenuation spectra are shown in Fig. 3.6. Very low loss (0.175–0.181 dB/km at λ = 1550 nm, 0.192–0.202 dB/km over the C+L band) was observed for each core, and no distinctive degradations for the outer cores were observed.

It was confirmed that each core was fabricated as we designed, from good agreement between the designed and measured values of the optical properties shown in Table 3.2. Macrobend losses were observed to be very low due to the trench-assisted structure and the long λ_{cc}.

3.6 Evaluation of the Crosstalk Characteristics of the Fabricated MCF

As for the XT evaluation, at first, we measured the XT of MCF-E by using the measurement setup shown in Fig. 2.6 with no averaging by rewinding, because the iterations of rewinding and measurement require a lot of

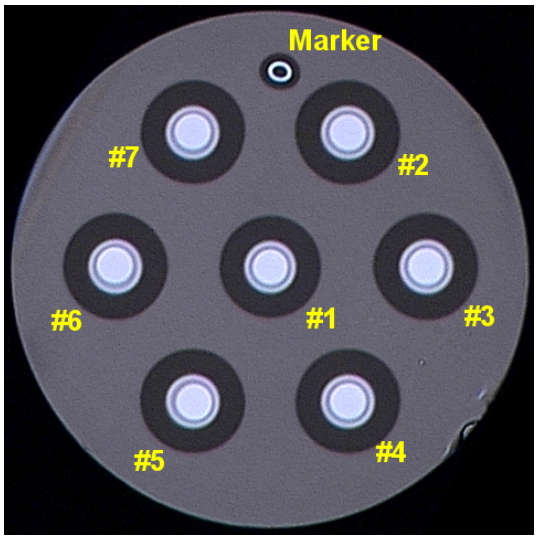

Fig. 3.5: Cross-section of MCF-E.

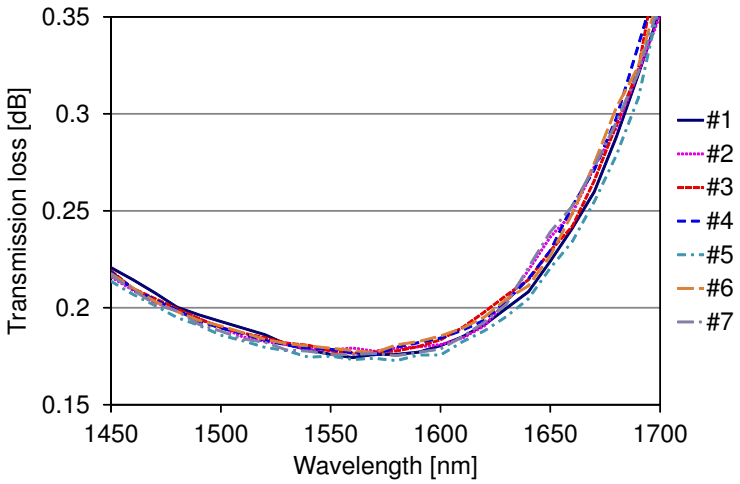

Fig. 3.6: Spectra of transmission losses of cores of MCF-E.

Table. 3.2: Measured optical properties of each core of MCF-E.

	Attenuation [dB/km]		MFD [μm]	A_{eff} [μm^2]	λ_{cc} [nm]	Chromatic disp. [ps/(nm · km)]	Disp. slope [ps/(nm^2 · km)]	Bend loss [dB/turn] at R_{b} = 5 mm	
λ [nm]	1550	1625	1550	1550	N/A	1550	1550	1550	1625
Design	N/A	N/A	9.86	79.6	1496	23.3	0.063	0.010	0.021
Core 1	0.176	0.196	9.83	80.2	1509	22.2	0.062	0.011	0.020
Core 2	0.179	0.197	9.76	80.2	1500	22.2	0.062	0.010	0.020
Core 3	0.181	0.202	9.88	81.3	1504	22.2	0.062	0.010	0.020
Core 4	0.177	0.199	9.85	80.8	1498	22.2	0.062	0.011	0.021
Core 5	0.175	0.192	9.74	79.0	1485	22.2	0.062	0.011	0.022
Core 6	0.179	0.200	9.80	79.9	1483	22.1	0.062	0.011	0.022
Core 7	0.177	0.197	9.72	78.2	1498	22.2	0.062	0.010	0.019
Avg.	0.178	0.197	9.79	79.9	1497	22.2	0.062	0.010	0.021
Max.	0.181	0.197	9.88	81.3	1509	22.2	0.062	0.011	0.022
Min.	0.175	0.197	9.72	78.2	1483	22.1	0.062	0.010	0.019

time for the long MCF. Measured values of the XT of MCF-E after 17.6-km propagation are shown in Fig. 3.7. The XT was defined as the ratio of the output power of a certain core to sum of output power of all cores. The MCF was wound on a bobbin whose winding radius was 140 mm, during the measurement. The average values of the XT between neighboring cores were -60.7 dB at λ = 1550 nm, and -59.9 dB at λ = 1625 nm.

However, each of those values was obtained from one measured value without any statistic treatments, as mentioned above. Furthermore, they are largely discrepant from the mean XT (μ_X) calculated from the theoretical approximation model described in Section 3.3, as shown in Fig. 3.8.

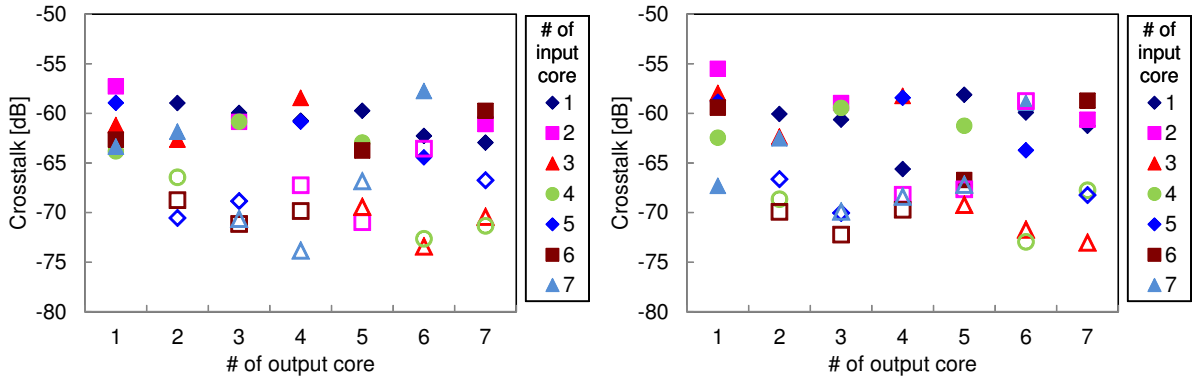

(a) λ = 1550 nm. (b) λ = 1625 nm.

Fig. 3.7: Measured crosstalk of MCF-E after 17.6-km propagation. Filled marks: XT between neighboring cores, open marks: XT between non-neighboring cores.

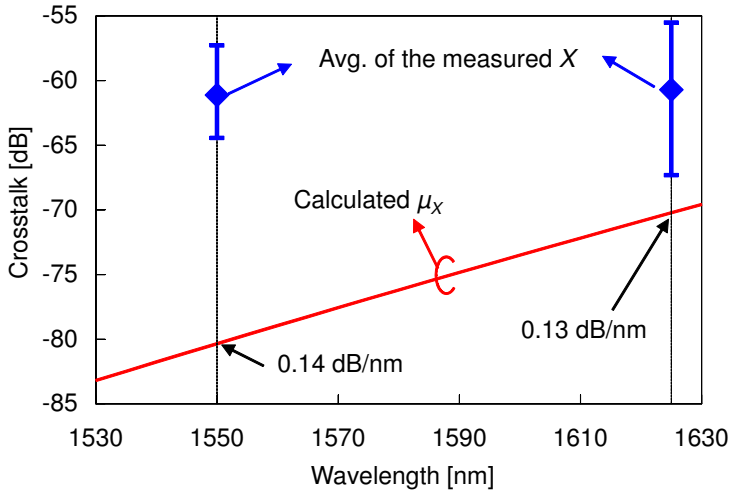

Fig. 3.8: Difference between the measured crosstalk and the mean crosstalk calculated using Eq. 3.11. Diamonds: averages of the measured values, error-bars: the maximum and the minimum of the measured values, solid line: calculated mean crosstalk (μ_X).

3.6.1 Suppression of Measurement Floor for Low-Crosstalk Measurement

We speculated that the XT discrepancy can be caused by unexpected XT that occurred at a butt joint between the MCF and a receiving single-core fiber. So, we investigated the unexpected XT at the butt joint by measuring power coupled at the butt joint between two single-core single-mode fiber (SMF), because receiving the power of unexcited core of the very-low-XT MCF can be regarded as receiving the power of a SMF with a large misalignment of the core pitch of the MCF, as shown in Fig. 3.9, if the power coupling at the butt joint is dominant. Figure 3.10 shows relationships between misalignment and normalized power coupled at a butt joint of two SMFs

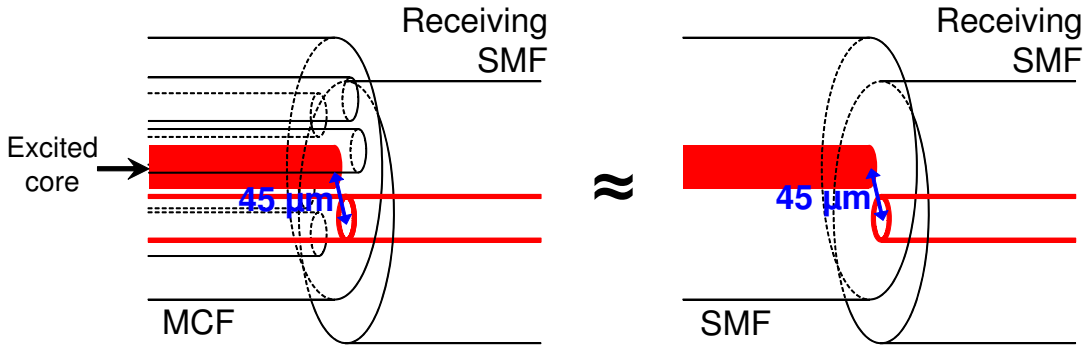

Fig. 3.9: Comparison between the coupling from a MCF to a receiving SMF and that from another SMF to the receiving SMF. Receiving the power of an unexcited core of a very-low-XT MCF may be regarded as receiving the power of a SMF with a large misalignment, if the power coupling at the butt joint is dominant.

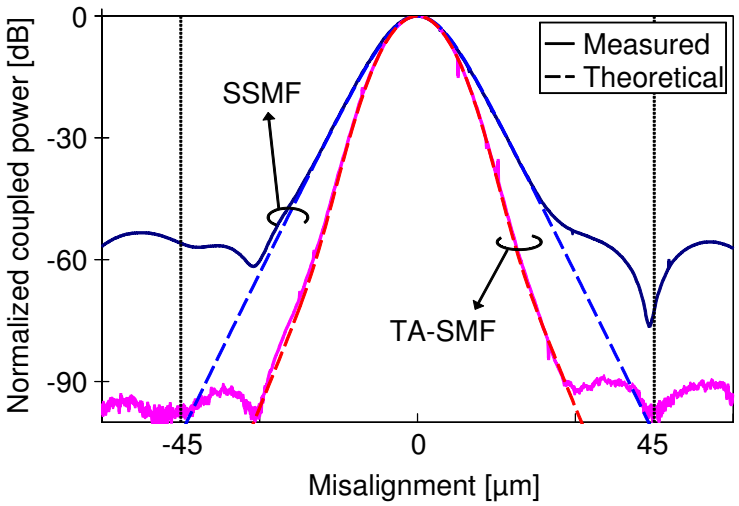

Fig. 3.10: Normalized power coupled at a butt joint between two single-core SMFs at 1550 nm.

at λ = 1550 nm. SSMF and TA-SMF denote standard SMF and trench-assisted SMF, respectively. Solid and dashed lines represent measured and theoretical profiles, respectively. The latter were calculated by the overlap integral between fundamental modes of the two SMFs by using the following equation:

$$C_{nm} = \frac{\left| \iint E_n E_m \, dx\, dy \right|^2}{\iint |E_n|^2 \, dx\, dy \iint |E_m|^2 \, dx\, dy}, \tag{3.17}$$

where C_{nm} is the power coupling coefficient of a butt joint between Core m and Core n. The measured profiles were observed to have power floors. The floor for SSMFs was about -60 dB, and that for TA-SMFs was less than

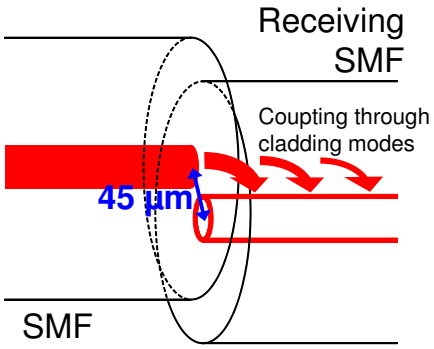

Fig. 3.11: A schematic of the coupling through the cladding modes at a butt joint between two SMFs.

−90 dB. We consider that the floor was caused by coupling from cladding modes to a core mode during propagation in the receiving SMF—Fig. 3.11 shows the schematics—, which can be the cause of the XT discrepancy and can be suppressed by a trench layer. According to these results, we employed TA-SMFs, which have almost the same core profile with cores of the MCF, as a launching fiber and a receiving fiber in the measurements.

3.6.2 Development of the Statistical Measurement Method for the Crosstalk

3.6.2.1 Possible Measurement Error due to the Wavelength Dependence of the Mean Crosstalk

Since the XT can be the stochastic parameter as described in Section 3.3, we need to evaluate the XT statistically. In the measurement described in Chapter 2, we had rewound MCFs for perturbing their twist and bend, but this method is unpractical to obtain an actual distribution with a large number of samples of XT values from a long MCF, which requires many times of rewinding and consumes a lot of time. However, the phase differences can be varied not only by the variations of the bend and twist but also by the variations of propagation constants that depend on the wavelength. Therefore, we developed the method for randomizing the phase differences by utilizing wavelength dependences of the phase differences. By scanning the wavelength, the phase differences at every phase-matching points can be randomized, and the statistical distribution of the XT can be obtained.

However, the wavelength dependences of κ must be cared in this method, because they affect how the XT is distributed, as shown in Eqs. 3.6, 3.8, and 3.11. So, we investigated the effect of the wavelength dependences of κ on the shape and mean of the XT distribution. Based on Fig. 3.8, we assumed that the mean XT μ_X can be approximated to be exponentially—linearly in the decibel scale— proportional to the wavelength as shown in Fig. 3.12; thus, the wavelength dependence of μ_X can be represented as

$$\mu_{X,0}(\delta\lambda) = \mu_X(\lambda_0+\delta\lambda) = \mu_X(\lambda_0)\,10^{\frac{s_{\mu X}\delta\lambda}{10}}, \tag{3.18}$$

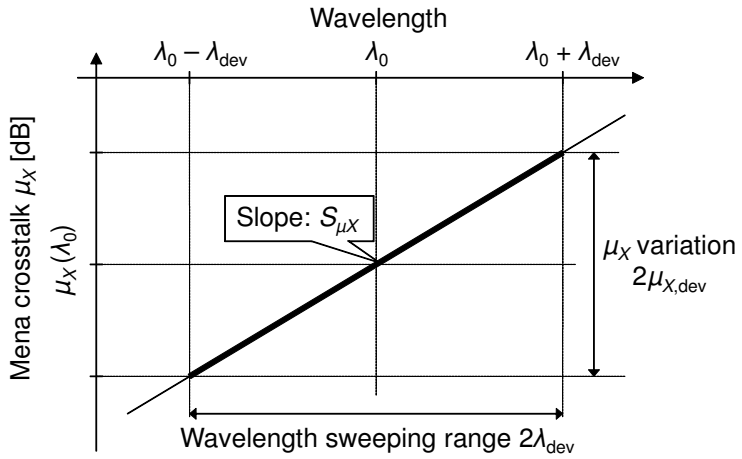

Fig. 3.12: A schematic of the wavelength dependence of mean crosstalk.

where $\mu_{X,0}(\delta\lambda)$ is μ_X at $\lambda_0+\delta\lambda$, and $S_{\mu X}$ is the slope of μ_X against the wavelength in the decibel scale, respectively. The mean value $\mu_{X,\mathrm{meas}}$ of the XT distribution measured over the wavelength range from $\lambda_0-\lambda_{\mathrm{dev}}$ to $\lambda_0+\lambda_{\mathrm{dev}}$ can be represented as

$$\begin{aligned}\mu_{X,\mathrm{meas}} &= \frac{1}{2\lambda_{\mathrm{dev}}}\int_{-\lambda_{\mathrm{dev}}}^{\lambda_{\mathrm{dev}}} \mu_{X,0}(\delta\lambda)\, d\delta\lambda \\ &= \mu_{X,0}(\lambda_0)\,\mathrm{sinhc}\left(\frac{\ln 10}{10}\mu_{X,\mathrm{dev}}\right),\end{aligned} \tag{3.19}$$

where $\mu_{X,\mathrm{dev}}$ equals to $S_{\mu X}\lambda_{\mathrm{dev}}$, and

$$\mathrm{sinhc}(z) \equiv \begin{cases} \dfrac{\sinh z}{z} & (z\neq 0) \\ 1 & (z=0). \end{cases} \tag{3.20}$$

Since $\sigma_{4\mathrm{df}}^2$ is linearly proportional to μ_X, the XT distribution at $\lambda_0+\lambda_{\mathrm{dev}}$ in the case of 4 df can be represented as

$$f_0(X,\delta\lambda) = \frac{X}{\left(2\sigma_{4\mathrm{df}}^2 10^{\frac{S_{\mu X}\delta\lambda}{10}}\right)^2}\exp\left(-\frac{X}{2\sigma_{4\mathrm{df}}^2 10^{\frac{S_{\mu X}\delta\lambda}{10}}}\right). \tag{3.21}$$

Accordingly, the XT distribution to be measured over the wavelength range from $\lambda_0-\lambda_{\mathrm{dev}}$ to $\lambda_0+\lambda_{\mathrm{dev}}$ can be

obtained as (see Appendix 3.B):

$$
\begin{aligned}
f_{\mathrm{meas}}(X) &= \frac{1}{2\lambda_{\mathrm{dev}}} \int_{-\lambda_{\mathrm{dev}}}^{\lambda_{\mathrm{dev}}} f_0(X, \delta\lambda)\, d(\delta\lambda) \\
&= \frac{10}{\ln 10} \frac{1}{2\mu_{X,\mathrm{dev}}} \left[\left(\frac{1}{X} + \frac{1}{2\sigma_{4\mathrm{df}}^2 10^{\frac{\mu_{X,\mathrm{dev}}}{10}}} \right) \exp\left(- \frac{X}{2\sigma_{4\mathrm{df}}^2 10^{\frac{\mu_{X,\mathrm{dev}}}{10}}} \right) \right. \\
&\qquad \left. - \left(\frac{1}{X} + \frac{1}{2\sigma_{4\mathrm{df}}^2 10^{\frac{-\mu_{X,\mathrm{dev}}}{10}}} \right) \exp\left(- \frac{X}{2\sigma_{4\mathrm{df}}^2 10^{\frac{-\mu_{X,\mathrm{dev}}}{10}}} \right) \right],
\end{aligned}
\tag{3.22}
$$

The estimated measurement error—$\mu_{X,\mathrm{meas}}/\mu_X$ in decibels— of μ_X for the variation width $2\mu_{X,\mathrm{dev}}$ in the wavelength scanning range, and the XT distributions estimated to be measured for several $2\mu_{X,\mathrm{dev}}$ are shown in Figs. 3.13 and 3.14, respectively. $2\mu_{X,\mathrm{dev}}$ of a few decibels induces the measurement error less than 0.1 dB and negligible change in the shape of the XT distribution. Therefore, we determined the wavelength scanning range for MCF-E as 10 nm; $2\mu_{X,\mathrm{dev}}$ was less than 1.4 dB based on Fig. 3.8.

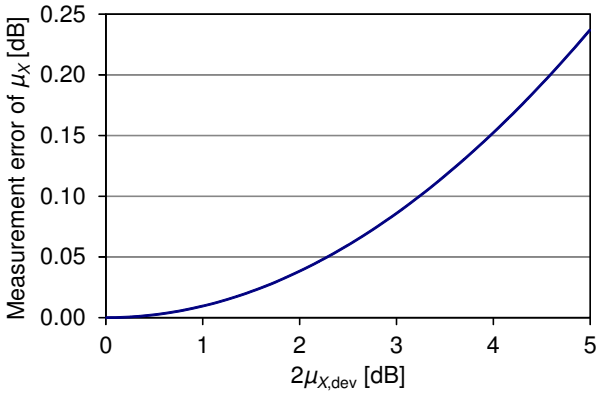

Fig. 3.13: The dependence of the expected measurement error of the mean crosstalk μ_X on the μ_X variation width $2\mu_{X,\mathrm{dev}}$ in the wavelength scanning range.

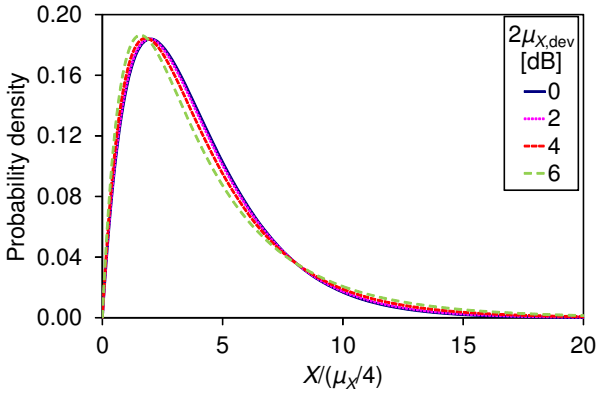

Fig. 3.14: XT distributions expected to be measured with the wavelength scanning, for several μ_X variation widths $2\mu_{X,\mathrm{dev}}$.

3.6.2.2 *Measured Spectrum and Statistical Distribution of the Crosstalk*

We obtained XT distributions of MCF-E, whose length was 17.4 km and bend radius was 140 mm, at λ = 1550 nm and λ = 1625 nm by sweeping the laser wavelength in ranges of $\lambda \pm 5$ nm with 5 pm step. An averaging time for each wavelength step was one millisecond. The typical linewidth of the laser was specified as 100 kHz. The spectrum of the measured XT from Core 1 to Core 5 of the MCF around λ = 1625 nm are shown in Fig. 3.15, as an example. The XT was measured to be heavily dependent on the wavelength, so that the phase differences were considered to be adequately randomized; there was no specific cycle length in the XT spectrum. The XT distribution obtained from the same data of Fig. 3.15 is shown in Fig. 3.16. The measured XT distribution was well fitted with a scaled chi-square distribution with 4 df expressed in Eq. 3.6.

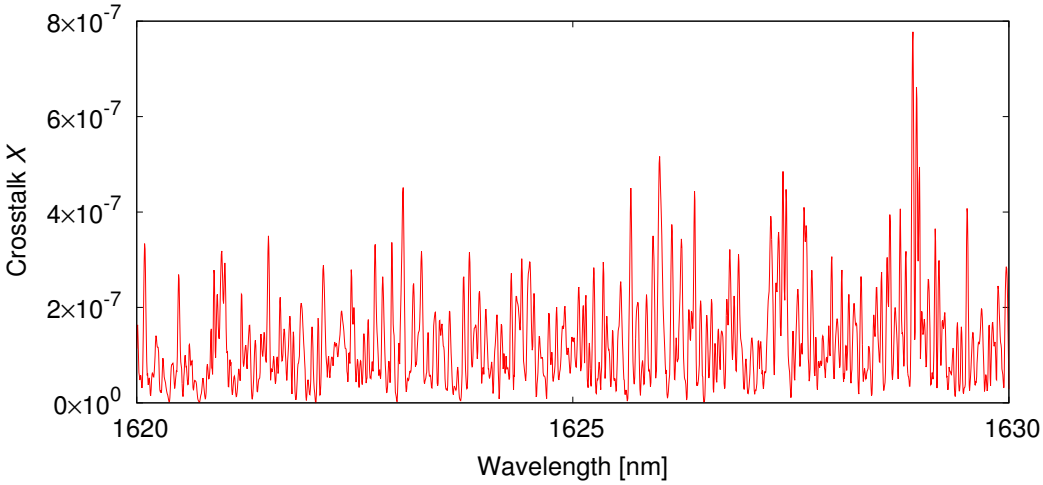

Fig. 3.15: The measured spectrum of the crosstalk from Core 1 to Core 5 of MCF-E.

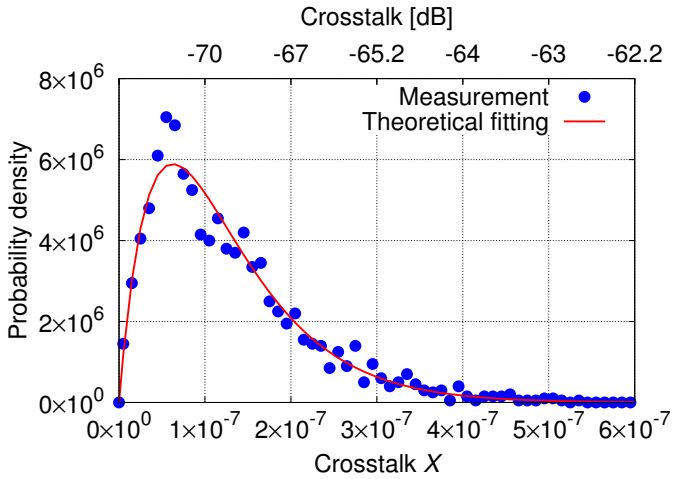

Fig. 3.16: The crosstalk distribution obtained from the data of Fig. 3.15.

3.6.3 Measured Mean Crosstalk of the Fabricated MCF

The values of the mean crosstalk between the neighboring cores of MCF-E obtained by fitting the measured XT distributions with Eq. 3.6 are plotted in Fig. 3.17. The average and maximum values of the measured mean XT were -79.5 dB and -77.6 dB, respectively, at λ = 1550 nm, and -69.8 dB and -67.7 dB, respectively, at λ = 1625 nm. The values between non-neighboring cores were too low to measure. The mean XT to the center core, which was coupled from six outer cores, was -72.3 dB at λ = 1550 nm and -62.1 dB at λ = 1625 nm from the sums of the measured values. The measured values were in good agreement with the calculated ones. Variations in the measured values are considered to be due to variations in core pitches and index profiles between the cores. By using the wavelength scanning method, the XT of MCF-E was statistically confirmed to be extremely low.

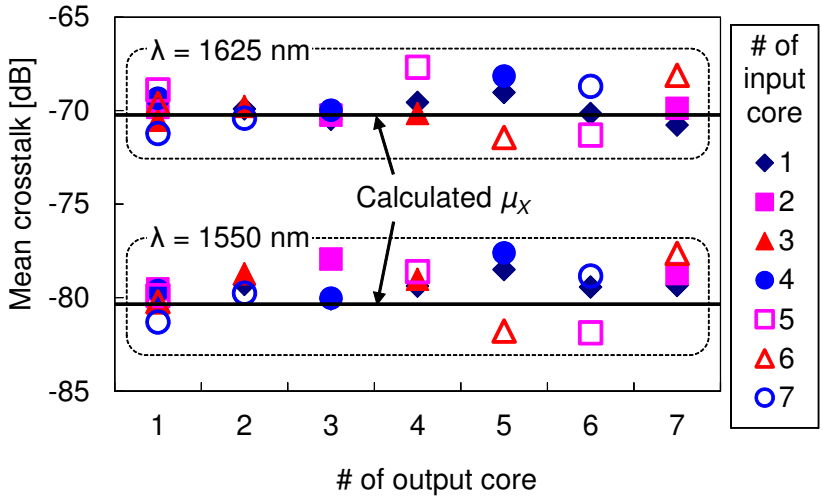

Fig. 3.17: Measured mean crosstalk of MCF-E after 17.4-km propagation at R_b = 140 mm.

Bend radius dependences of the mean XT were also observed between combinations of Cores 1, 4, and 5. Figure 3.18 shows the results at λ = 1625 nm. The number of radii, where the mean XT was measured, was two. When the origin of the coordinates are included, the mean XT was observed to be linearly proportional to the bend radius, as predicted in Eq. 3.11. Slight difference of the mean XT of opposite directions in the each graph of Figs. 3.18a–3.18c is considered to be caused by measurement error due to the extremely low XT.

From the results, the theoretical approximation model described in Section 3.3 was validated, and the XT of MCF-E was confirmed to be extremely low.

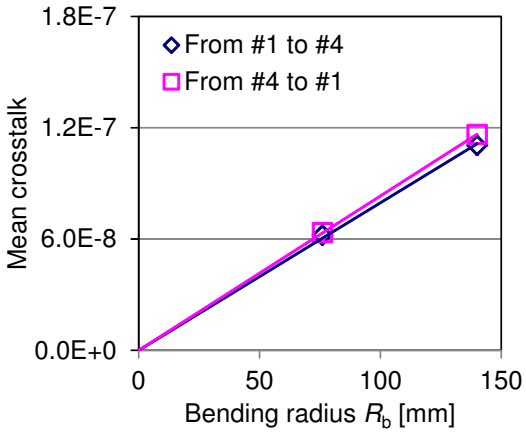

(a) Between Cores 1 and 4.

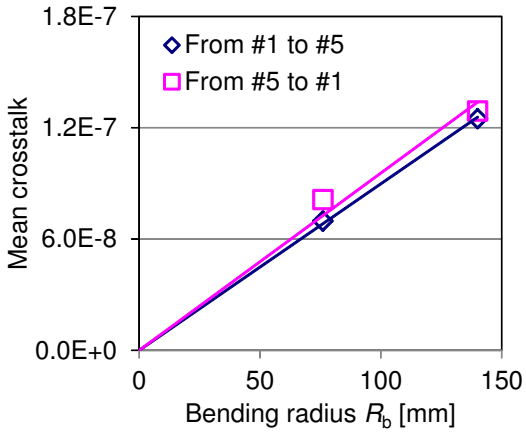

(b) Between Cores 1 and 5.

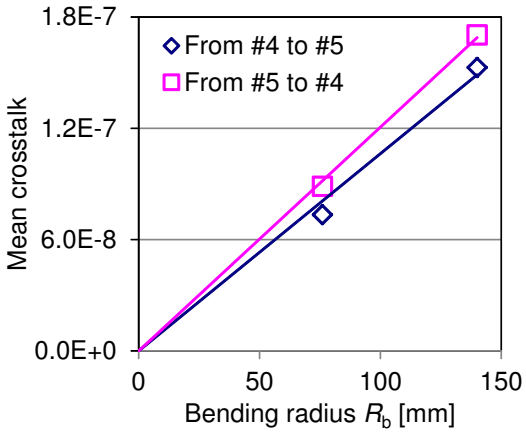

(c) Between Cores 4 and 5.

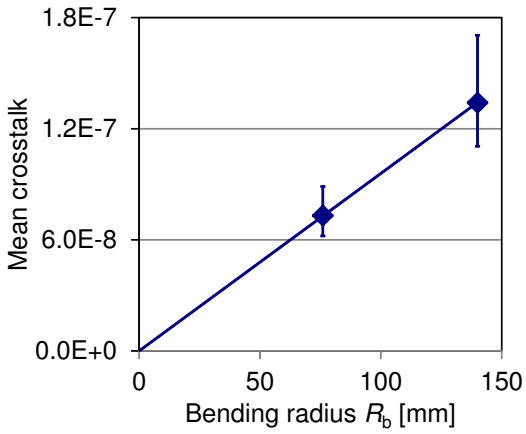

(d) Average of the mean crosstalk between Cores 1, 4, and 5.

Fig. 3.18: Bend radius dependence of the measured mean crosstalk of MCF-E after 17.4-km propagation at λ = 1625 nm.

3.7 Estimation of the Crosstalk of the Fabricated MCF After Long-Distance Propagation

Based on Eq. 3.16, the dependence of the mean XT of MCF-E on propagation length L [km] and bend radius R_b [mm] can be estimated. The XT coefficients XT_{coeff} for the XT to the center core were 2.41×10^{-11}/(km · mm) at λ = 1550 nm and 2.56×10^{-10}/(km · mm) at λ = 1625 nm. The relationship between L, R_b, and the mean XT are shown in Fig. 3.19. The mean XT after 10,000-km propagation at λ = 1625 nm can be less than −30 dB if R_b is less than ∼39 cm. Such bend radii can be applied to MCFs by appropriate cabling, e.g., the fiber ribbon cable with helical slots. The 0.9999-quantile of the XT distribution (μ_X + 7.7 [dB]) after 100-km propagation was estimated to be less than −30 dB.

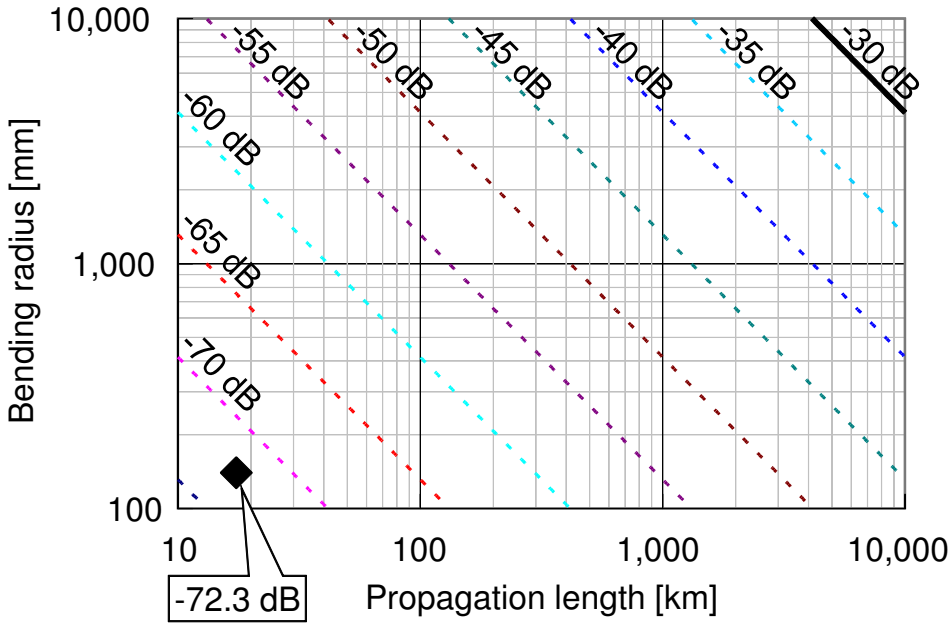

(a) λ = 1550 nm.

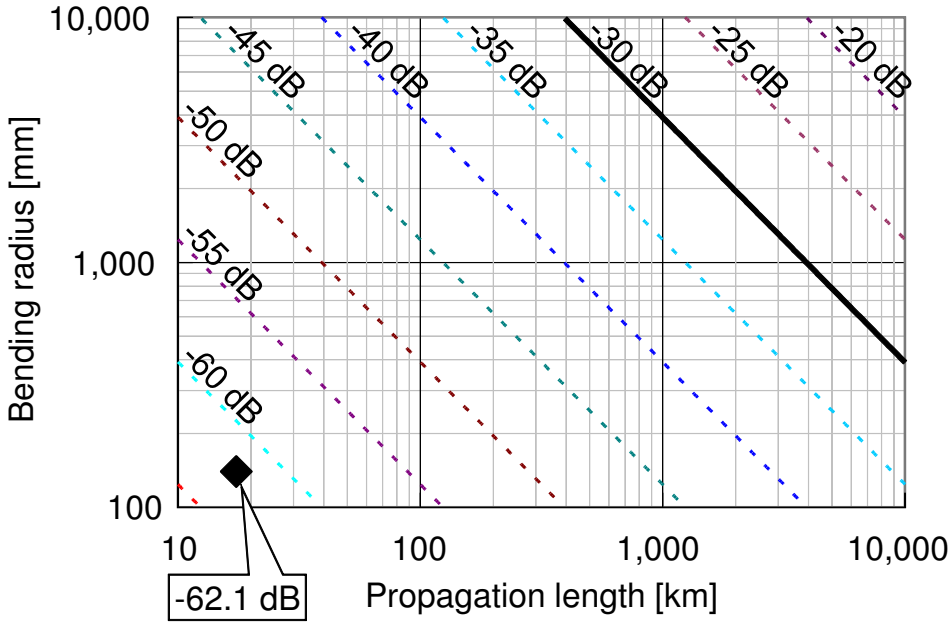

(b) λ = 1625 nm.

Fig. 3.19: Relationship between the propagation length L, the bend radius R_{b}, and the mean crosstalk μ_X to the center core of MCF-E. The filled diamonds represent L and R_{b} where μ_X was measured. Contour lines represent the estimated μ_X from the measurement values and Eq. 3.16

3.8 Conclusion of This Chapter

In this chapter, we reported the design and fabrication of an ultra-low-XT and low-loss MCF. To deal with a random longitudinal evolution of the XT, we developed an approximation model, and derived analytical expressions of the statistical distribution and mean of the XT. Considering a homogeneous MCF, the mean XT was linearly proportional to the bend radius and fiber length. We designed a trench-assisted seven-core MCF based on the above theoretical scheme. We fabricated the MCF with pure-silica cores, and achieved, to the best of our knowledge, the lowest attenuation for the MCF, 0.175–0.181 dB/km at λ = 1550 nm, and 0.192–0.202 dB/km over the C+L band. We obtained the statistical distributions of the XT of the fabricated MCF, and the measurement results were in good agreement with the developed model. The mean XT between the neighboring cores was found to be less than -77.6 dB at λ = 1550 nm and less than -67.7 dB at λ = 1625 nm when the MCF was wound on a 140-mm-radius bobbin. The mean XT from six outer cores to one center core was -72.3 dB at λ = 1550 nm and -62.1 dB at λ = 1625 nm calculated from sums of the measured values. From the measurement results and the validated model, the mean XT from the six outer cores to the center core at λ = 1625 nm even after the 10,000-km propagation was estimated to be less than -30 dB in a practical applicable bend radius range of the MCF.

By leveraging MCF-E's extremely low XT, very low transmission loss, and moderate A_{eff}, some of the world-first transmission experiments have been conducted by using MCF-E. Sakaguchi *et al.* conducted the transmission experiment that achieved the transmission capacity more than 100 Tb/s per fiber for the first time, by using MCF-E [50]. Awaji *et al.* conducted the transmission experiment where signals were multiplexed on Laguerre-Gaussian modes—orbital angular momentum modes— and transmitted through the optical fiber for the first time, by using MCF-E [25, 51].

3.A Appendix: Derivation of Eq. 3.10

By assuming that $A_{n,0} = 0$ and $A_{m,0} = 1$, Eq. 3.2 can be rewritten as

$$A_{n,1} = -jK_{nm} \exp\left[j\phi_{\mathrm{rnd},nm,1}\right]. \tag{3.23}$$

Here, $\phi_{\mathrm{rnd},nm,1}$ does not affect the absolute value of $A_{n,1}$; thus, we assume $\phi_{\mathrm{rnd},nm,1} = 0$. Accordingly, K_{nm} can be expressed as

$$K_{nm} = jA_{n,1} \tag{3.24}$$

based on Eq. 3.2 $A_{n,1}$ is the amplitude of Core n after the first phase-matching point and can be derived from Eqs. 2.18 and 2.19. Equation 2.18 for Core m and Core n can be rewritten as

$$A_n(z) = -j\int_0^z \kappa_{nm}\exp\left\{j\left[\phi_n(z') - \phi_m(z')\right]\right\}A_m(z')\,dz', \tag{3.25}$$

where $A(z)$ represents the amplitude evolution along the longitudinal axis z of the fiber. Here, we assume that the fiber is twisted continuously at a constant rate $\omega_{\text{twist}} = 2\pi f_{\text{twist}}$ [radians/unit length]; hence, Eq. 2.19 can be rewritten as

$$\phi(z) = \begin{cases} \beta_{\text{int},m} z, \\ \displaystyle\int_0^z \beta_{\text{int},n}\left(1 + \frac{d_{nm}}{R_{\text{b}}}\cos\omega_{\text{twist}} z'\right)dz'. \end{cases} \tag{3.26}$$

In this case, the first and second phase-matching points exist at $z = \frac{\pi}{2}\frac{1}{\omega_{\text{twist}}}$, and $z = \frac{3\pi}{2}\frac{1}{\omega_{\text{twist}}}$, respectively. Therefore, $A_{n,1}$ can be expressed as $A_n\left(\frac{\pi}{2}\frac{1}{\omega_{\text{twist}}}\right)$ and Eq. 3.24 can be rewritten as

$$K_{nm} = jA_n\left(\frac{1}{2f_{\text{twist}}}\right) \tag{3.27}$$

By assuming the low XT case—$A_m(z) \approx A_m(0) = 1$—, Eq. 3.27 can be derived as follows:

$$\begin{aligned} K_{nm} &= \kappa_{nm}\int_0^{\frac{\pi}{\omega_{\text{twist}}}} \exp\left\{j\left[\phi_n(z') - \phi_m(z')\right]\right\}dz' \\ &= \kappa_{nm}\int_0^{\frac{\pi}{\omega_{\text{twist}}}} \exp\left[j\left(\beta_{\text{int},n} - \beta_{\text{int},m}\right)z'\right]\exp\left[j\frac{\beta_{\text{int},n} d_{nm}}{\omega_{\text{twist}} R_{\text{b}}}\sin\left(\omega_{\text{twist}} z'\right)\right]dz' \\ &= \kappa_{nm}\int_0^{\frac{\pi}{\omega_{\text{twist}}}} \exp\left[j\left(\beta_{\text{int},n} - \beta_{\text{int},m}\right)z'\right]\sum_{\nu} J_\nu\left(\frac{\beta_{\text{int},n} d_{nm}}{\omega_{\text{twist}} R_{\text{b}}}\right)\exp\left(j\nu\omega_{\text{twist}} z'\right)dz' \\ &= \kappa_{nm}\sum_{\nu} J_\nu\left(\frac{\beta_{\text{int},n} d_{nm}}{\omega_{\text{twist}} R_{\text{b}}}\right)\int_0^{\frac{\pi}{\omega_{\text{twist}}}} \exp\left[j\left(\beta_{\text{int},n} - \beta_{\text{int},m} + \nu\omega_{\text{twist}}\right)z'\right]dz', \end{aligned} \tag{3.28}$$

by using the following equation (obtained by substituting $t = \exp(j\theta)$ to Eq. (11.2) in Ref. [52]):

$$\exp(jx\sin\theta) = \sum_{\nu=-\infty}^{\infty} J_\nu(x)\exp(j\nu\theta), \tag{3.29}$$

where $J_\nu(x)$ denotes the Bessel function of the first kind of order ν, and ν is an integer. Assuming that $\beta_{\text{int}} = \beta_{\text{int},n} = \beta_{\text{int},m}$, we obtain

$$K_{nm} = \kappa\left[\frac{\pi}{\omega_{\text{twist}}} J_0\left(\frac{\beta_{\text{int}} d_{nm}}{\omega_{\text{twist}} R_{\text{b}}}\right) + \frac{j}{\omega_{\text{twist}}}\sum_{\nu\neq 0}\frac{(-1)^\nu - 1}{\nu} J_\nu\left(\frac{\beta_{\text{int}} d_{nm}}{\omega_{\text{twist}} R_{\text{b}}}\right)\right]. \tag{3.30}$$

Eq. 3.30 can be rewritten as

$$K_{nm} \simeq \sqrt{\frac{\kappa^2}{\beta_{\rm int}}\frac{R_{\rm b}}{d_{nm}}\frac{2\pi}{\omega_{\rm twist}}}\left[\cos\left(\frac{\beta_{\rm int}d_{nm}}{\omega_{\rm twist}R_{\rm b}}-\frac{\pi}{4}\right)+\frac{j}{\pi}\sum_{\nu\neq 0}\frac{(-1)^{\nu}-1}{\nu}\cos\left(\frac{\beta_{\rm int}d_{nm}}{\omega_{\rm twist}R_{\rm b}}-\nu\frac{\pi}{2}-\frac{\pi}{4}\right)\right], \tag{3.31}$$

using the following equation (Eqs. (11.137) and (11.138) in Ref. [52]):

$$J_{\nu}(x) \simeq \sqrt{\frac{2}{\pi x}}\cos\left[x-\left(\nu+\frac{1}{2}\right)\frac{\pi}{2}\right], \qquad \left(8x \gg 4\nu^2-1\right). \tag{3.32}$$

Assuming that $\beta_{\rm int}\sim 10^7$, $d_{nm}\sim 4\times 10^{-5}$, $\omega_{\rm twist}\sim 1$, and $R_{\rm b} <\sim 1$, Eq. 3.32 holds for small ν. Eq. 3.32 does not hold for large ν, but the Bessel function in the second term of the right-hand side of Eq. 3.30 is divided by ν so that Eq. 3.31 holds. The summation term in the imaginary part in the square brackets of Eq. 3.31 can be rewritten as

$$\begin{aligned}\sum_{\nu\neq 0}\frac{(-1)^{\nu}-1}{\nu}\cos\left(x-\nu\frac{\pi}{2}-\frac{\pi}{4}\right) &= \sum_{\nu\neq 0}\frac{(-1)^{\nu}-1}{\nu}\left[\cos\left(x-\frac{\pi}{4}\right)\cos\left(\nu\frac{\pi}{2}\right)+\sin\left(x-\frac{\pi}{4}\right)\sin\left(\nu\frac{\pi}{2}\right)\right]\\ &= \sin\left(x-\frac{\pi}{4}\right)\sum_{\nu\neq 0}\frac{(-1)^{\nu}-1}{\nu}\sin\left(\nu\frac{\pi}{2}\right).\end{aligned} \tag{3.33}$$

The summation term of the cosine on the right-hand side of Eq. 3.33 is odd in the variable ν and equals zero, and the remaining terms on the right-hand side is even in the variable ν. Thus, it can be rewritten as

$$\begin{aligned}\sin\left(x-\frac{\pi}{4}\right)\sum_{\nu\neq 0}\frac{(-1)^{\nu}-1}{\nu}\sin\left(\nu\frac{\pi}{2}\right) &= 2\sin\left(x-\frac{\pi}{4}\right)\sum_{\nu=1}^{\infty}\frac{(-1)^{\nu}-1}{\nu}\sin\left(\nu\frac{\pi}{2}\right)\\ &= 2\sin\left(x-\frac{\pi}{4}\right)\sum_{\nu'=0}^{\infty}\frac{-2}{2\nu'+1}\sin\left[(2\nu'+1)\frac{\pi}{2}\right]\\ &= -\pi\sin\left(x-\frac{\pi}{4}\right),\end{aligned} \tag{3.34}$$

by using the following equation (see p. 888 in Ref. [52]):

$$\sum_{\nu=0}^{\infty}\frac{\sin(2\nu+1)x}{2\nu+1} = \begin{cases}\pi/4, & (0<x<\pi),\\ -\pi/4, & (-\pi<x<0).\end{cases} \tag{3.35}$$

By using Eqs. 3.33 and 3.34, Eq. 3.31 can be rewritten as

$$K_{nm} \simeq \sqrt{\frac{\kappa^2}{\beta_{\mathrm{int}}}\frac{R_{\mathrm{b}}}{d_{nm}}\frac{2\pi}{\omega_{\mathrm{twist}}}}\left[\cos\left(\frac{\beta_{\mathrm{int}}d_{nm}}{\omega_{\mathrm{twist}}R_{\mathrm{b}}}-\frac{\pi}{4}\right)-j\sin\left(\frac{\beta_{\mathrm{int}}d_{nm}}{\omega_{\mathrm{twist}}R_{\mathrm{b}}}-\frac{\pi}{4}\right)\right]$$
$$\simeq \sqrt{\frac{\kappa^2}{\beta_{\mathrm{int}}}\frac{R_{\mathrm{b}}}{d_{nm}}\frac{2\pi}{\omega_{\mathrm{twist}}}}\exp\left[-j\left(\frac{\beta_{\mathrm{int}}d_{nm}}{\omega_{\mathrm{twist}}R_{\mathrm{b}}}-\frac{\pi}{4}\right)\right]. \tag{3.36}$$

Thus, $|K_{nm}|$ can be derived as Eq. 3.10. As shown in Fig. 3.20, Eq. 3.10 was also validated by comparing the values of $|K_{nm}|$ obtained using Eq. 3.10 and those numerically calculated using Eqs. 3.25–3.27 for two identical step-index cores for the combinations of core Δ (0.35, 0.4%), d_{nm} (35, 40 μm), R_{b} (60, 120, 180, 240, 300 mm), and f_{twist} (0.01, 0.1, 1, 10 turns/m).

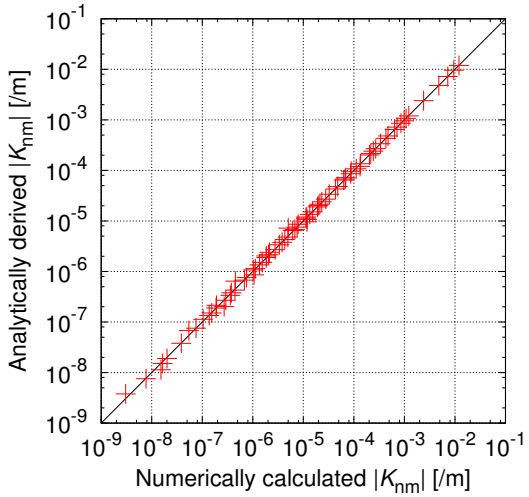

Fig. 3.20: Comparison between values of $|K_{nm}|$ obtained by using the analytically derived Eq. 3.10 and those numerically calculated using Eqs. 3.25–3.27.

3.B Appendix: Derivation of Eq. 3.22

Based on Eq. 3.21 and the first line of Eq. 3.22, $f_{\mathrm{meas}}(X)$ can be derived as

$$
\begin{aligned}
f_{\mathrm{meas}}(X) &= \frac{1}{2\lambda_{\mathrm{dev}}} \int_{-\lambda_{\mathrm{dev}}}^{\lambda_{\mathrm{dev}}} \frac{X}{\left(2\sigma_{4\mathrm{df}}^2 10^{\frac{S_{\mu X}\delta\lambda}{10}}\right)^2} \exp\left(-\frac{X}{2\sigma_{4\mathrm{df}}^2 10^{\frac{S_{\mu X}\delta\lambda}{10}}}\right) d(\delta\lambda) \\
&= \frac{1}{2S_{\mu X}\lambda_{\mathrm{dev}}} \frac{10}{\ln 10} \frac{1}{X} \int_{\frac{X}{2\sigma_{4\mathrm{df}}^2 10^{\frac{S_{\mu X}\lambda_{\mathrm{dev}}}{10}}}}^{\frac{X}{2\sigma_{4\mathrm{df}}^2 10^{\frac{-S_{\mu X}\lambda_{\mathrm{dev}}}{10}}}} t\exp(-t)\, dt \\
&= \frac{1}{2\mu_{X\mathrm{dev}}} \frac{10}{\ln 10} \frac{1}{X} \left[\Gamma\left(2, \frac{X}{2\sigma_{4\mathrm{df}}^2 10^{\frac{\mu_{X\mathrm{dev}}}{10}}}\right) - \Gamma\left(2, \frac{X}{2\sigma_{4\mathrm{df}}^2 10^{\frac{-\mu_{X\mathrm{dev}}}{10}}}\right)\right],
\end{aligned}
\tag{3.37}
$$

by substituting

$$
t = \frac{X}{2\sigma_{4\mathrm{df}}^2 10^{\frac{S_{\mu X}\delta\lambda}{10}}}, \tag{3.38}
$$

and using the incomplete gamma function:

$$
\Gamma(a,x) = \int_x^{\infty} t^{a-1}\exp(-t)\, dt. \tag{3.39}
$$

When a is an integer n, the incomplete gamma function can be rewritten as (see p. 527 in Ref. [52]):

$$
\Gamma(n,x) = (n-1)!\exp(-x)\sum_{k=0}^{n-1}\frac{x^k}{k!}. \tag{3.40}
$$

By using Eq. 3.40, Eq. 3.37 can be rewritten as the last line of Eq. 3.22.

Chapter 4

Effect of Inter-Core Crosstalk on Transmission Quality

4.1 Introduction to This Chapter

In Chapter 3, the target level of the crosstalk (XT) suppression was set such that the 0.9999-quantile of the statistical distribution should be less than -30 dB, after the earlier studies [17, 18] which set the target as the XT less than -30 dB. However, this target level did not necessarily have the theoretical grounding. Therefore, we studied on the behavior of the XT as a noise, and its effect on the transmission quality, or Q-factor. The investigation of the effect of the XT on the transmission quality is already underway [53, 54]; however, the stochasticity of the XT has not been taken into account.

In this chapter, we discuss how the XT behaves stochastically, reveal the behavior of the XT as a noise, and consider and quantify the effect of the XT on Q-factor.

4.2 Stochastic Behavior of the Crosstalk

Due to the various longitudinally-varying perturbations, the XT of the MCF is a stochastic parameter, as described in Sections 2.2.6, 3.3, and 3.6.2.2. In this section, the stochastic behavior of the XT are further described, to understand how the XT behaves as a noise. For explanation simplicity, we deal with the case where the bend-induced perturbation is dominant, as with Sections 2.2.6, 3.3, and 3.6.2.2.

As described in Sections 3.3 and 3.6.2.2, the XT evolution on the in-phase–quadrature (I–Q) plane depends on the phase difference between cores, and is a kind of the random walks because the phase difference can be randomized by the changes of various parameters such as the fiber bend and twist.

The probability density function (PDF) of the XT on the I–Q plane converges to the Gaussian distribution from the central limit theorem, if the MCF is adequately long, or adequately many phase matchings occur along the MCF. Since the PDF of l random numbers, whose PDFs are the standard normal distribution, is the chi-square distribution with l degrees of freedom (df), the PDF of the XT in power—that is, the sum of the in-phase (I) and

the quadrature (Q) components of two polarization modes— converges to the chi-square distribution with 4 df.

The XT X vary with wavelength. Figure 4.1 shows the XT spectra for 200-GHz ($\sim$1.76-nm) span of MCF-E, which were plotted from 10-nm-span spectra measured for evaluating the mean XT in Chapter 3. The XT values showed significant fluctuations only within tens of gigahertz. This is because the longitudinal profile of the phase difference between the cores varies with wavelength.

The XT vary not only with wavelength but also with time. Figure 4.2a shows the time variation of X at the wavelength of 1625 nm and its measurement interval was 15 minutes. In order to induce the large variation of the phase difference, we changed the ambient temperature during the measurement as shown in Fig. 4.2b. Time variation of X is considered to be caused by the slight variations of the refractive index profile, which can be caused by the variations of temperature, (residual) external stress, and so on. Random variation of X value can also be seen in Fig. 4.2a.

Figure 4.3 shows the probability distributions of X, to be precise, X normalized with $\mu_X/4$. Blue diamonds represent the probability distribution of X varied with wavelength, obtained by using the data plotted in Fig. 4.3 (XT from Core 1 to Core 5) as the population (its sample number was 353). Red squares represent the probability distribution of X varied with time, obtained by using the data plotted in Fig. 4.2a as the population (its sample number was 130). Since both the probability density distributions obtained from the wavelength variation and the time variation are in good agreement with the chi-square distribution with 4 df, X can be considered to be normally distributed on the I–Q planes of two polarization modes. For organizing the stochasticity of the XT, the variation, averages, and probability distribution of X are illustrated schematically in Fig. 4.4. Though we measured the X variation under the large perturbation in the long time span as shown in Fig. 4.2, we also measured the X spectrum variation in short time span to know the XT behavior under stable environment as shown in Fig. 4.5. The X spectrogram was measured for 1-nm span, in long time after winding the MCF on the bobbin. Under the stable environment, it can be seen that the XT X of the MCF varies very gradually, because the time variation of temperature and residual external stress changes very gradually.

So far, we discussed the case where the bend perturbation is dominant. However, even if the bend perturbation is small, the phase correlations between the cores exponentially decay in longitudinal direction with a correlation length of only several centimeters [55]; accordingly, the phase differences between the cores are uncorrelated between the adequately separated different longitudinal points. Therefore, if the MCF length is adequately long, the PDF of the XT in the MCF can be considered to converge to the normal distribution on the I–Q plane, also in cases where the bend perturbation is small. Based on these discussions, we can understand that X varies with wavelength and time, and its PSD on the I–Q plane is the chi-square distribution.

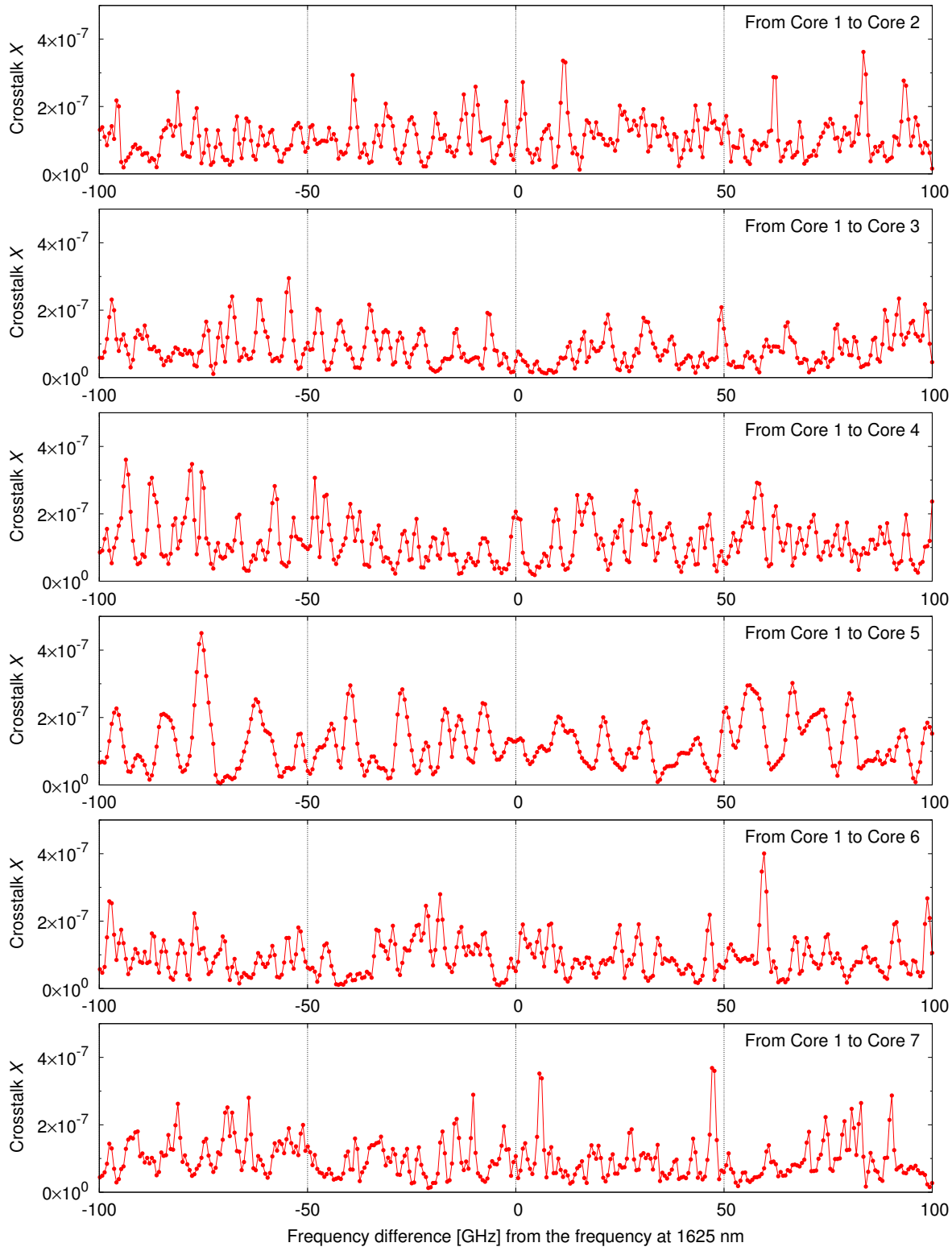

Fig. 4.1: The crosstalk spectrum of MCF-E ($L = 17.4$ km) for 200-GHz ($\sim$1.76-nm) span around 1625 nm. The measurement step: 5 pm ($\sim$0.6 GHz).

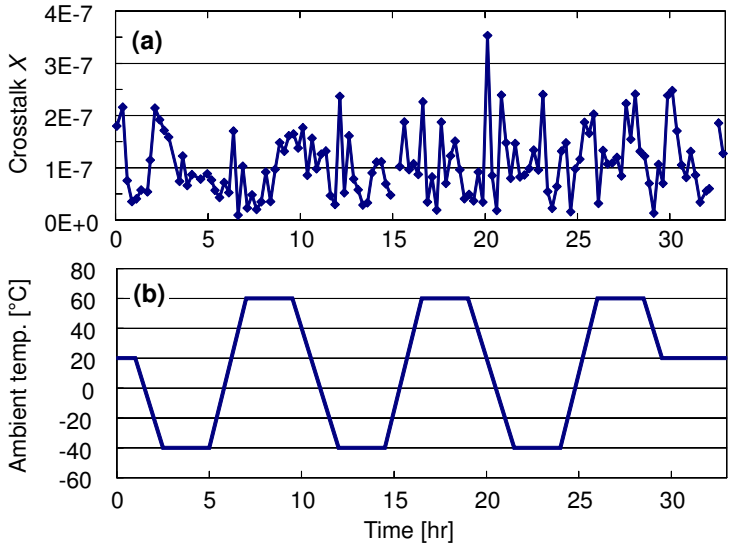

Fig. 4.2: (a) Measured time variation of the crosstalk of MCF-E, under (b) the change of the ambient temperature. The measurement interval: 15 min.

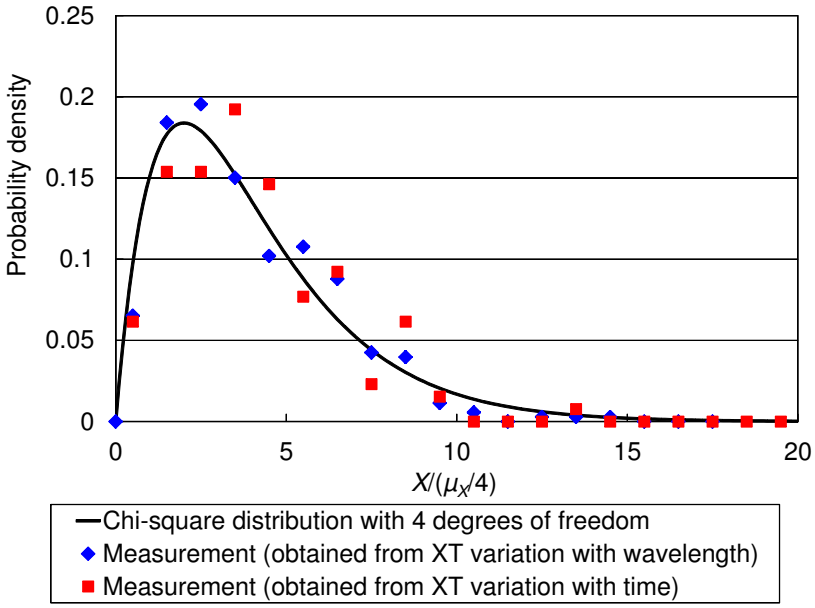

Fig. 4.3: Probability distributions of the crosstalk of MCF-E.

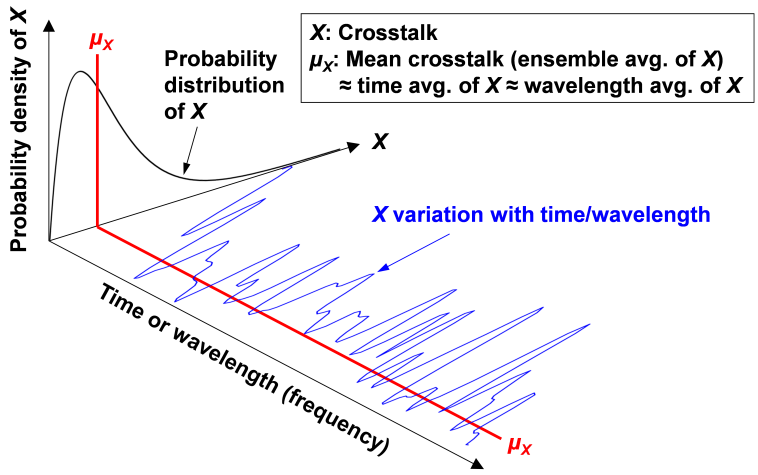

Fig. 4.4: Schematic illustration on the statistical characteristics of the crosstalk.

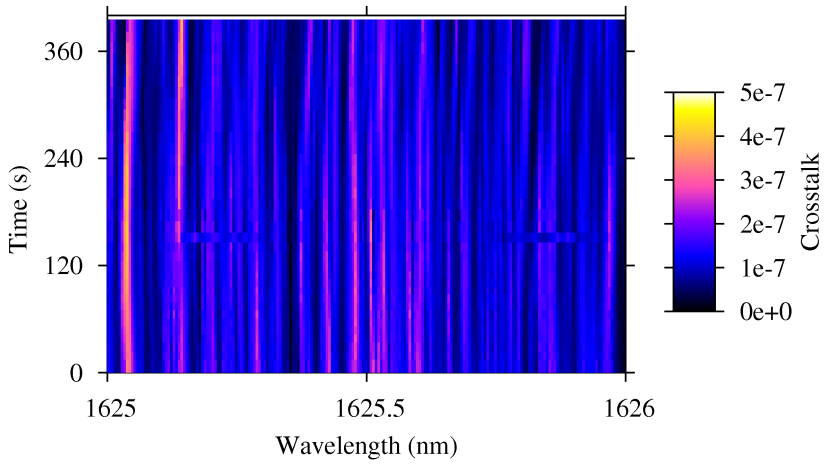

Fig. 4.5: Time variation of the crosstalk spectrum of MCF-E. (measurement interval: ∼11 sec.)

4.3 Effect of the Crosstalk on *Q*-Factor

Based on the stochastic behavior of the XT described in Section 4.2, the behavior of the XT as a noise can be considered to depend on the bandwidth of a signal light. From the short-period variation of the XT spectrum shown in Fig. 4.1, XT may behave as Gaussian-distributed noise on the I–Q plane in cases where the bandwidth of the signal light is adequately broad, because the instantaneous frequency of the signal light may rapidly vary with time, due to the modulation or the phase noise of the signal light. When the bandwidth becomes narrower, the XT distribution on the I–Q plane can become more distorted from the Gaussian distribution. Moreover, if the bandwidth is adequately narrow, the XT may behave as an effectively static coupling, since the variation of X is very gradual compared to the ordinary symbol rate in the order of picoseconds to nanoseconds, based on

the time variation of the XT spectrum shown in Fig. 4.5. However, this static coupling may gradually vary with time, and its PSD obeys the chi-square distribution in the power—that is, the normal distribution in the complex amplitude—, as shown in Figs. 4.3–4.4. In the following, we discuss the effect of XT on the transmission quality, or Q-factor, in the simple cases of the adequately broad and adequately narrow bandwidth of the signal light, as the first step.

4.3.1 Case of Adequately Broad Bandwidth of the Signal Light

In the case of adequately broad bandwidth, the XT can be approximated as the virtual additive white Gaussian noise (AWGN) on the I–Q plane, like amplified spontaneous emission (ASE) noise [56] and nonlinear interference noise [57]; thus, we can discuss very simply the relationship between the mean XT (μ_X) and Q-factor. Q-factor is defined as [58]:

$$Q = \frac{|\mu_1 - \mu_2|}{\sigma_1 + \sigma_2}, \tag{4.1}$$

by using the average positions μ_i and standard deviations σ_i of the nearest neighboring constellation points on a constellation diagram. The decibel value of the Q-factor can be expressed as

$$Q_{\mathrm{dB}} = 20\log_{10} Q = 10\log_{10} Q^2. \tag{4.2}$$

Therefore, hereinafter, we will discuss the Q^2-factor instead of the Q-factor. If we assume $\sigma_{\mathrm{noise}} = \sigma_1 = \sigma_2$, and let $S = |\mu_1 - \mu_2|$ the nearest distance between the constellation symbols, the Q^2-factor can be expressed as

$$Q^2 = \left(\frac{|\mu_1 - \mu_2|}{\sigma_1 + \sigma_2}\right)^2 = \frac{S^2}{4\sigma_{\mathrm{noise}}^2}. \tag{4.3}$$

Thus, the Q^2-factor without the XT noise can be expressed as

$$Q^2_{\mathrm{w/oXT}} = \frac{S^2}{4\sigma^2_{\mathrm{w/oXT}}}, \tag{4.4}$$

where $\sigma_{\mathrm{w/oXT}}$ is σ_{noise} without the XT. When we consider the total mean XT $\mu_{X,\mathrm{total}}$ from other cores, where the mean XT is defined as the average power of the XT light divided by that of the signal power P_{signal}, the variance σ^2_{XT} of the XT light on the I–Q planes can be expressed as

$$\sigma^2_{\mathrm{XT}} = P_{\mathrm{signal}} \frac{\mu_{X,\mathrm{total}}}{4}. \tag{4.5}$$

Since "the variance of the sum of statistically independent variables" equals to "the sum of the variances of the statistically independent variables," the noise variance including the XT can be considered to be the sum of $\sigma^2_{\mathrm{w/oXT}}$ and σ^2_{XT}. Therefore, the Q^2-factor affected by the XT can be obtained from Eqs. 4.3–4.5 as

$$Q^2_{\mathrm{w/XT}} = \frac{S^2}{4\left(\sigma^2_{\mathrm{w/oXT}} + \sigma^2_{\mathrm{XT}}\right)} = \left(\frac{1}{Q^2_{\mathrm{w/oXT}}} + \frac{P_{\mathrm{signal}}}{S^2}\mu_{X,\mathrm{total}}\right)^{-1}, \tag{4.6}$$

and XT-induced Q^2-penalty can be expressed as

$$\frac{Q^2_{\mathrm{w/oXT}}}{Q^2_{\mathrm{w/XT}}} = 1 + Q^2_{\mathrm{w/oXT}}\mu_{X,\mathrm{total}}\frac{P_{\mathrm{signal}}}{S^2} = \left(1 - Q^2_{\mathrm{w/XT}}\mu_{X,\mathrm{total}}\frac{P_{\mathrm{signal}}}{S^2}\right)^{-1}, \tag{4.7}$$

where P_{signal}/S^2 is the value determined by the modulation format. Values of P_{signal}/S^2 for typical ideal modulation formats are shown in Table 4.1 (see Fig. 4.6 for their constellations). The values were calculated by assuming

Table. 4.1: Values of P_{signal}/S^2 for the typical modulation format.

Modulation format	P_{signal}/S^2
PDM-QSPK	1
PDM-8PSK	$2^{1/2}/(2^{1/2}-1)$
PDM-16QAM	5
PDM-32QAM	10
PDM-64QAM	21
PDM-128QAM	41

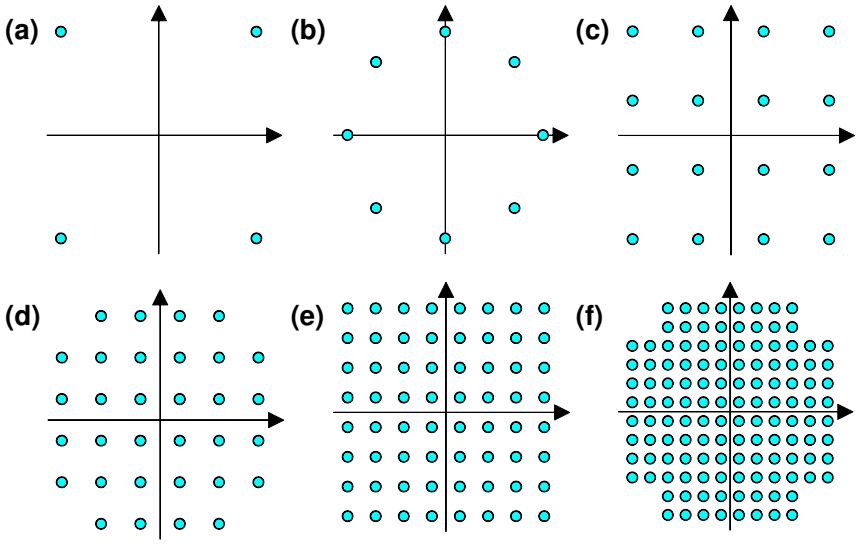

Fig. 4.6: Constellation diagrams for (a) QPSK, (b) 8PSK, (c) 16QAM, (d) 32QAM, (e) 64QAM, and (f) 128QAM, considered in this chapter.

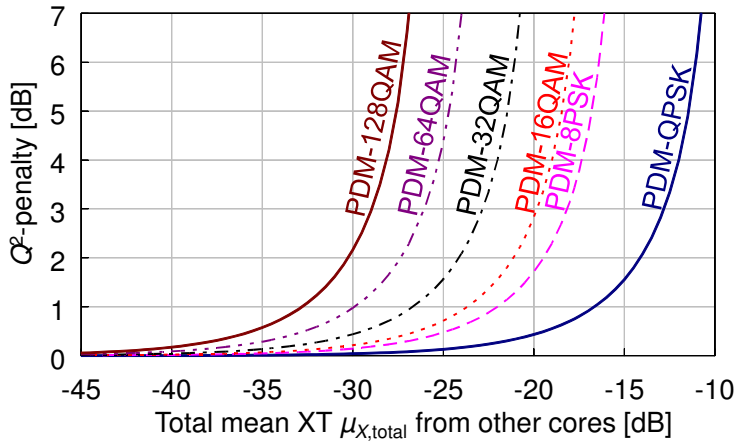

Fig. 4.7: Crosstalk-induced Q^2-penalty at $Q^2_{\text{w/XT}} = 9.8$ dB.

Table. 4.2: Maximum $\mu_{X,\text{total}}$ acceptable for suppressing the XT-induced Q^2-penalty no more than 1 dB when $Q^2_{\text{w/XT}} = 9.8$ dB.

Modulation format	$\mu_{X,\text{total}}$ [dB]
PDM-QPSK	-16.7
PDM-8PSK	-22.0
PDM-16QAM	-23.7
PDM-32QAM	-26.7
PDM-64QAM	-29.9
PDM-128QAM	-32.8

that the signals are equally distributed on each constellation point.

Figure 4.7 shows the XT-induced Q^2-penalty at $Q^2_{\text{w/XT}} = 9.8$ dB (bit-error rate BER = 1×10^{-3}), which was calculated using Eq. 4.7, and Table 4.2 shows maximum $\mu_{X,\text{total}}$ acceptable for suppressing the XT-induced Q^2-penalty of no more than 1 dB when $Q^2_{\text{w/XT}} = 9.8$ dB. The Q^2-penalty does not change if $Q^2_{\text{w/oXT}}\mu_{X,\text{total}}$ or $Q^2_{\text{w/XT}}\mu_{X,\text{total}}$ is unchanged; therefore, for example for the case of $Q^2_{\text{w/XT}} = 8.5$dB (-1.3 dB from 9.8 dB), the relationships shown in Fig. 4.7 are offset in $\mu_{X,\text{total}}$ of +1.3 dB, and $\mu_{X,\text{total}}$ values in Table 4.2 are added +1.3dB.

4.3.2 Case of Adequately Narrow Bandwidth of the Signal Light

In the case of adequately narrow bandwidth, the XT may behave as the static coupling, as we discussed in Section 4.2. Accordingly, in this case, the relationships between X and the Q^2-factor can be equivalent to those investigated in Ref. [53]—in Ref. [53], the effect of the XT on the signal-to-noise ratio was investigated numerically by assuming the XT as a static coupling, and experimentally by realizing the XT as an effectively static coupling using optical couplers and variable optical attenuators. Reference [53] reported that XT-induced penalty

at the BER of 1×10^{-3} is less than 1 dB, when the XT—corresponding to X in this thesis— is less than -18 dB for QPSK, -24 dB for 16QAM, -32 dB for 64QAM. These X values are similar to the $\mu_{X,\mathrm{total}}$ values shown in Table 4.2; however, these X values are the acceptable X values and not the acceptable $\mu_{X,\mathrm{total}}$ values. As discussed in Section 4.2, the X values can change temporally in the obedience to the distribution of Eq. 3.4 or 3.6, even in cases where X can be regarded as effectively static; therefore, we have to consider the relationship between the XT and the Q^2-penalty, based on q-quantile X_q of X, where $1-q$ is the probability that X will exceed X_q. Since X may change very gradually with time, it can take a long time for Q^2-factor to recover, once the Q^2-factor has fallen below the threshold value of the error correction. Therefore, it can be preferable to take an adequately low "$1-q$" value. As derived in Section 3.3, X_q can be expressed as Eqs. 3.13 and 3.14. Equation 3.14 can be rewritten as

$$X_q^{[\mathrm{dB}]}=\mu_X^{[\mathrm{dB}]}+\Delta X_q,\quad \Delta X_q=10\log_{10}\frac{F_{l\mathrm{df}}^{-1}(q)}{l}. \tag{4.8}$$

As shown in Eq. 4.8, X_q can be obtained by adding an appropriate value ΔX_q to the mean XT μ_X. Table 4.3 shows the values of ΔX_q for several values of q and $1-q$, and Fig. 4.8 shows the relationships between ΔX_q and $1-q$, in cases where the polarization modes randomly couple (4 df) and of no polarization mode coupling (2 df). Note that the case of 4 df can be applied for most of the general MCFs which do not maintain polarization modes. From Table 4.3, ΔX_q can range from $\sim$7 dB to $\sim$11 dB at the range of adequately low $1-q$ from 10^{-3} to 10^{-10}.

From this section, it was confirmed that "the mean XT $\mu_{X,\mathrm{total}}$ that induces 1-dB penalty at the BER of 1×10^{-3} for the adequately broad bandwidth" is similar to "the XT X that induces 1-dB penalty at the BER of 1×10^{-3} for the adequately narrow bandwidth." Furthermore, some additional margin may be required for cases of adequately narrow bandwidth, compared to cases of adequately broad bandwidth, based on the fact that a small $1-q$ of 10^{-10} to 10^{-3} requires a relatively large ΔX_q of $\sim$7 dB to $\sim$11 dB.

Table. 4.3: Difference ΔX_q between the q-quantile X_q and the mean μ_X of the XT X.

q	$1-q$	ΔX_q [dB] (4 df)	ΔX_q [dB] (2 df)
0.999	10^{-3}	6.6	8.4
0.9999	10^{-4}	7.7	9.6
0.99999	10^{-5}	8.5	10.6
0.999999	10^{-6}	9.2	11.4
0.9999999	10^{-7}	9.8	12.1
0.99999999	10^{-8}	10.3	12.7
0.999999999	10^{-9}	10.8	13.2
0.9999999999	10^{-10}	11.2	13.6

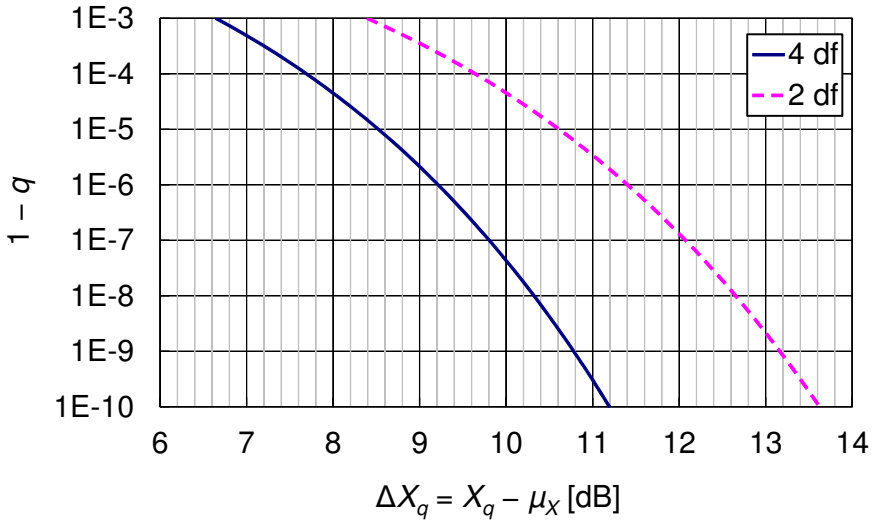

Fig. 4.8: Relationships between $\Delta X_q = X_q - \mu_X$ and $1-q$, or the probability that X exceeds X_q.

4.4 Conclusion of This Chapter

We discussed how the XT of the MCF behaves stochastically, revealed the behavior of the XT as a noise, and investigated the effect of the XT on Q-factor. When the bandwidth of the signal light is adequately broad, XT may behave as a virtual AWGN on the I–Q plane, like ASE and nonlinear noises.

If we assume the signal is equally distributed on every constellation point, the XT-induced Q^2-penalty at the Q^2 of 9.8 dB—the BER of 1×10^{-3}— can be less than 1 dB, when the aggregate mean XT from the other cores is less than -16.7 dB for PDM-QPSK, -23.7 dB for PDM-16QAM, and -29.9 dB for PDM-64QAM.

When the bandwidth of the signal light is adequately narrow, XT X can behave as an effectively static coupling, compared to the symbol rate, but can change very gradually with time. So, the margin for the gradual temporal change has to be considered for setting the target level of the XT for the system with adequately narrow bandwidth signal light.

It should be investigated in detail in the future, whether the XT distributions on the I–Q planes are Gaussian enough or somewhat distorted in actual transmission conditions, and further studies are necessary to reveal the dependence of "relationship the signal light bandwidth and crosstalk behavior" on "the MCF length and structure." However, it can be speculated that the more couplings occur, the more rapidly X changes with wavelength. Based on the X spectra shown in Fig. 4.1—where X was coupled only from one core for only 17 km—, X that are coupled from many cores for long distance—e.g., hundreds or thousands of kilometers— has the possibility to vary much more rapidly with wavelength than X shown in Fig. 4.1. Thus, X may be considered as the virtual AWGN in cases of high-capacity long-haul transmissions where modulation symbol rates are in the order of tens of gigahertz or

more. On the other hand, the adequately narrow bandwidth should be less than a gigahertz, even in the case of Fig. 4.1. So, a possible example where virtual static couplings can occur is the orthogonal frequency division modulation (OFDM) with narrow-bandwidth subcarriers. In such case, X and Q^2-factor of the each subcarrier are possible to be very different from those of other subcarriers.

Based on this study, progress of understanding on results of transmission experiments using the MCF is expected.

Chapter 5

Enhancement of Signal-to-Noise Ratio of Multi-Core Fiber

5.1 Introduction to This Chapter

Recent transmission systems, using digital coherent detection and digital signal processing, can mitigate the linear distortions such as the chromatic dispersion and the polarization mode dispersion. Therefore, the suppressions of the amplified spontaneous emission (ASE) noise and the nonlinear interference (NLI) noise are very important for the high-capacity long-haul transmission over the single-core single-mode fiber (SMF), and the recent high-capacity single-mode transmission experiments have been conducted by using SMFs whose transmission loss was lowered for suppressing the ASE noise and effective area (A_{eff}) was enlarged for suppressing the NLI noise [5,59].

Though the crosstalk (XT) of MCF-E was adequately suppressed, suppressions of other noises are also very important for the high-capacity long-haul transmission. However, the transmission loss was higher than the conventional pure-silica-core SMF whose transmission loss is ≤ 0.17 dB/km, though the loss of MCF-E was lower than standard SMF and the lowest among the reported MCFs. The A_{eff} of MCF-E was approximately equal to and not enlarged from that of standard SMF. The MCFs reported by other groups also had not realized low loss and large A_{eff} simultaneously superior to the standard SMF [60–64]. Furthermore, the effect of the XT on the signal-to-noise ratio (SNR) had not been investigated well; therefore, it had been unclear whether or not enlarging of A_{eff} is effective to improving the SNR of the MCF.

In this chapter, we report the design and fabrication of a seven-core MCF that achieves low loss and large A_{eff} simultaneously. The transmission loss of the fabricated MCF was observed to be 0.163–0.172 dB/km (average: 0.168 dB/km), which is the lowest among the reported MCFs at the time of writing, to the best of our knowledge. In addition, we discuss how this result enhances the SNR in multi-core transmission systems.[*1]

[*1] To be precise, we discuss an optical SNR (OSNR) with the noise bandwidth equivalent to the signal bandwidth. This OSNR is different from the SNR because the OSNR does not include the effect of the back-to-back penalty, which is induced by the noise in transceivers, modulation imbalance, and so on. However, it can be confusing to call *the OSNR with the noise bandwidth equivalent to the signal bandwidth* just as *the OSNR*, since *the OSNR* is quite widely used as *the OSNR with the noise bandwidth of 0.1 nm*. Therefore, *the OSNR with the noise bandwidth equivalent to the signal bandwidth* is referred to as *the SNR* in this thesis.

5.2 Fiber Design

We designed an uncoupled seven-core MCF that has identical and hexagonally-arranged pure-silica cores. A trench-assisted core design was employed to confine the power strongly into the core for achieving both large A_{eff} and low XT. Figure 5.1 shows the designed relative refractive index difference (Δ) profile of the core. The core was designed to have A_{eff} of $\sim$130 $\mu\mathrm{m}^2$, cable cutoff wavelength (λ_{cc}) of 1460 nm, and the Rayleigh scattering coefficient lower than that of the MCF in Chapter 3. As for the design of the XT, based on Eq. 3.11, Λ of the MCF was designed to be 52 μm so that μ_X from six outer cores to the center core (center-core μ_X (= $6HL$)) can be less than -30 dB after 80-km propagation at 1625 nm when the MCF are wound on a 140-mm-radius bobbin. The cladding diameter was designed to be 187.5 μm so that excess loss of the outer cores (loss induced by coupling to coating modes) can be lower than 0.001 dB/km at 1625 nm.

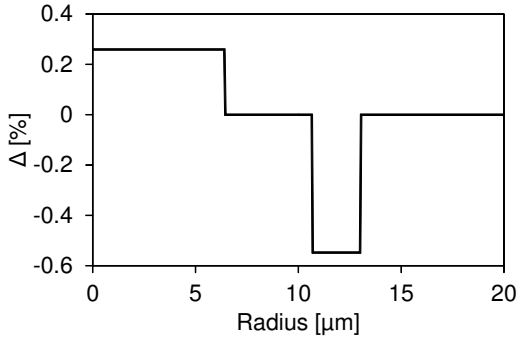

Fig. 5.1: A design profile of relative refractive index difference Δ. A refractive index of the cladding was taken as the reference of the relative refractive index difference Δ.

We should pay attention to the XT of uncoupled MCF also for lowering loss. The power coupling from Core n to other cores can be understood as power loss of Core n due to the XT:

$$\alpha_{\mathrm{XT},n} \approx \sum_{m \neq n} H_{mn}, \tag{5.1}$$

where the $\alpha_{\mathrm{XT},n}$ is the power loss coefficient [/unit length], and the H_{mn} is the power coupling coefficient [/unit length] from Core n to Core m. In the homogeneous seven-core fiber, the power loss coefficient due to the XT in the center core can be approximated to be $6H$ (the sum of the power-coupling coefficients to six outer cores). Thus, the XT-induced power loss coefficient $\alpha_{\mathrm{XT,dB}}$ in the unit of [dB/unit length] of the center core can be represented as

$$\alpha_{\mathrm{XT,dB}} = \frac{10}{\ln 10} 6H, \tag{5.2}$$

whose relationship is shown in Fig. 5.2. To suppress $\alpha_{\mathrm{XT,dB}}$ lower than 0.001 dB/km, $6H$ should be less than

2.30×10^{-4} /km (corresponding to the center-core μ_X less than -17.3 dB at $L = 80$ km), so that the XT target was appropriate in terms of loss.

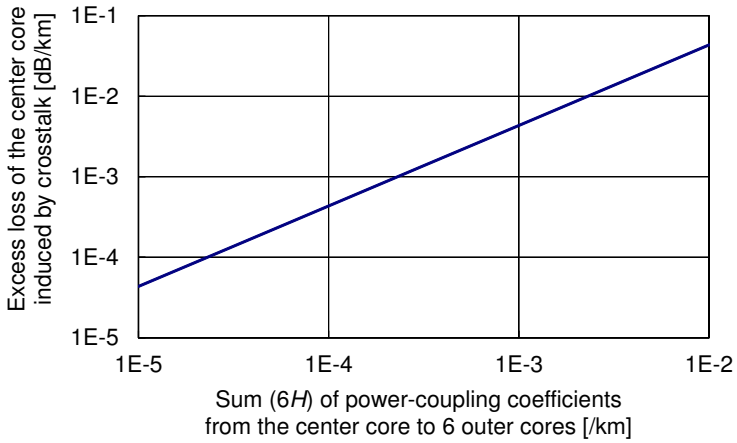

Fig. 5.2: A relationship between the aggregate power-coupling coefficient from the center core to six outer cores and the excess loss in the center core induced by the crosstalk.

5.3 Fabrication

We fabricated a pure-silica-core homogeneous seven-core fiber (MCF-F) based on the design. Figure 5.3 shows a cross-section of the MCF-F. The core pitch was 51 μm. The cladding diameter was 188 μm. The coating diameter was 334 μm. The fiber length was 6.99 km. Figure 5.4 and Table 5.1 show transmission loss spectra and optical properties of MCF-F. The transmission losses of the individual cores were observed to be very low values of 0.163–0.172 dB/km (average: 0.168 dB/km), thanks to the low-loss design and pure-silica core technology. A_{eff}s of the cores were slightly smaller than the design target but all of the A_{eff}s exceeded 120 μm^2. The λ_{cc}s were 1460 ± 10 nm and successfully fabricated as designed. The chromatic dispersions (D_{chrom}) were 21.7 ps/(nm · km). The bend losses were also well suppressed.

Figure 5.5 shows the μ_Xs between adjacent two cores of MCF-F, which were measured as wavelength averages of the XTs by using the wavelength scanning technique described in Section 3.6.2. Values of averages, maximums, and minimums of the μ_Xs between the adjacent two cores, and of total μ_Xs to the center core are shown in Table 5.2. The measured MCF was 6.99 km long and wound on a 140-mm-radius bobbin. The center-core μ_Xs for $L = 80$ km are also shown in Table 5.2, which were calculated based on the linear accumulation of the XT. The center-core μ_Xs can be less than -30 dB for L shorter than 1.4×10^3 km at 1550 nm, 8.7×10^2 km at 1565 nm, and 2.0×10^2 km at 1625 nm.

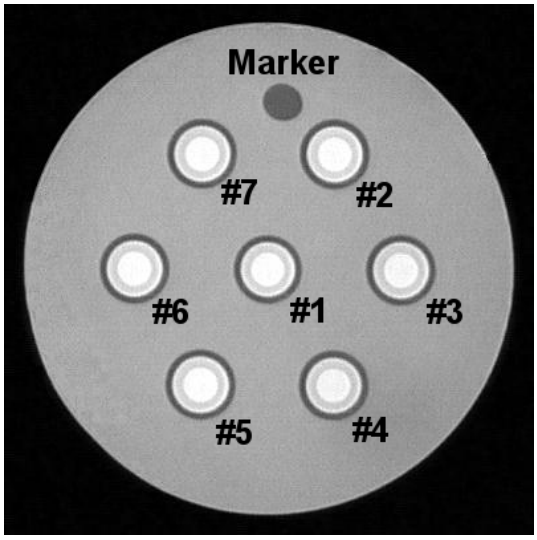

Fig. 5.3: A cross-section of MCF-F.

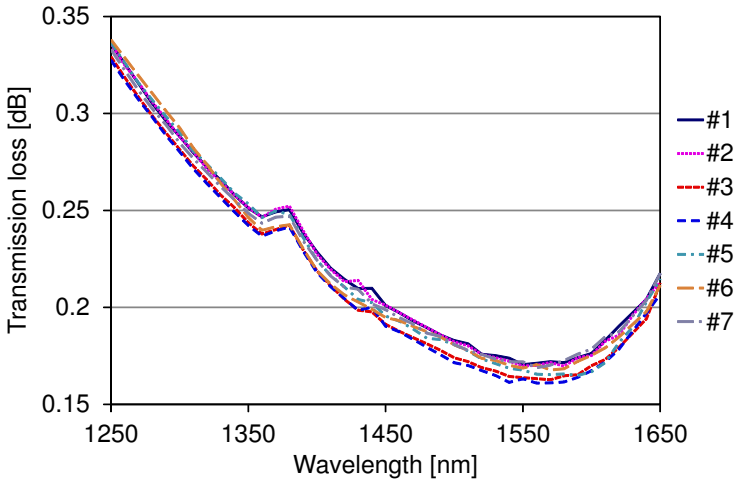

Fig. 5.4: Transmission loss spectra of the individual cores of MCF-F.

Table. 5.1: Measured optical properties of MCF-F

	Transmission loss [dB/km]		λ_{cc} [nm]	A_{eff} [μm^2]	MFD [μm]	D_{chrom} [ps/(nm · km)]	D_{chrom} slope [ps/(nm^2 · km)]	Bend loss [dB/turn] at R_b = 10 mm	
λ [nm]	1550	1625		1550				1550	1625
Design			1460	129.3	12.5	22.5	0.064		
Core 1	0.170	0.194	1458	121.3	12.2	21.7	0.062	0.08	0.21
Core 2	0.170	0.191	1458	123.5	12.2	21.7	0.063	0.08	0.20
Core 3	0.164	0.183	1468	125.9	12.3	21.7	0.063	0.11	0.26
Core 4	0.163	0.183	1459	124.3	12.2	21.7	0.063	0.11	0.26
Core 5	0.168	0.186	1470	126.9	12.4	21.7	0.063	0.11	0.27
Core 6	0.169	0.188	1457	122.4	12.1	21.7	0.063	0.10	0.27
Core 7	0.172	0.191	1466	124.1	12.2	21.7	0.063	0.12	0.30
Avg.	0.168	0.188	1462	124.1	12.2	21.7	0.063	0.10	0.26
Max.	0.172	0.194	1470	126.9	12.4	21.7	0.063	0.12	0.30
Min.	0.163	0.183	1457	121.3	12.1	21.7	0.062	0.08	0.20

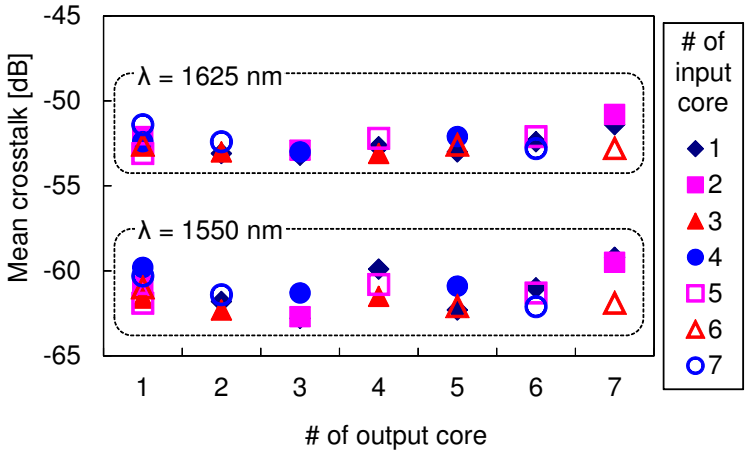

Fig. 5.5: Measured mean crosstalk between neighboring cores of MCF-F.

Table. 5.2: Measured mean crosstalk of MCF-F for L = 6.99 km and R = 140 mm.

λ	μ_X [dB] between adjacent cores			Total μ_X [dB] to the center core	Total μ_X [dB] to the center core estimated for L = 80 km
[nm]	Avg.	Min.	Max.		
1550	−61.3	−62.8	−59.2	−53.1	−42.5
1565	−59.2	−60.6	−56.9	−51.0	−40.4
1625	−52.5	−53.2	−50.8	−44.5	−34.0

5.4 Discussion on Signal-to-Noise Ratio Affected by Inter-Core Crosstalk

5.4.1 Effects of Fiber Parameters, System Parameters, and Crosstalk on SNR

To realize high-capacity and long-distance transmission, SNRs in MCF cores is an important factor as with single-core fibers. However, a proper suppression level of XT, where lowering loss and/or enlarging A_{eff} can be effective, has not been investigated yet. So, in this section, we will discuss the effects of system parameters and fiber parameters including the XT on SNRs in uncoupled MCF systems, and investigate how the SNR can be improved in the MCF systems. When assuming an ideal filtering (a noise bandwidth is equivalent to a signal bandwidth) and Nyquist limit of WDM, SNR of dispersion-uncompensated single-core (SC) transmission link with discrete optical amplifiers can be expressed as [42]:

$$\mathrm{SNR}_{\mathrm{SC}} = \frac{P_{\mathrm{Tx},ch}}{P_{\mathrm{ASE}}|_{B_{\mathrm{noise}}=R_{\mathrm{symbol}}} + P_{\mathrm{NLI}}|_{B_{\mathrm{noise}}=R_{\mathrm{symbol}}}}, \tag{5.3}$$

$$P_{\mathrm{ASE}} = N_{\mathrm{span}} F \left(e^{\alpha L_{\mathrm{span}}} - 1\right) \mathrm{h}\nu B_{\mathrm{noise}}, \tag{5.4}$$

$$P_{\mathrm{NLI}} = a_{\mathrm{NLI}} P_{\mathrm{Tx},ch}^3, \tag{5.5}$$

$$a_{\mathrm{NLI}} = \left(\frac{2}{3}\right)^3 N_{\mathrm{span}} \gamma^2 L_{\mathrm{eff}} \frac{\ln\left(\pi^2 |\beta_2| L_{\mathrm{eff}} B_{\mathrm{WDM}}^2\right)}{\pi |\beta_2| R_{\mathrm{symbol}}^3} B_{\mathrm{noise}}, \tag{5.6}$$

where the symbols are explained in Table 5.3.

Based on the characteristics of XT in MCF discussed in Chapter 4, XT in MCFs may be regarded as a virtual additive white Gaussian noise by assuming adequately broad bandwidth of signal light. Thus, SNR in a certain core in dispersion-uncompensated multi-core (MC) transmission link with uncoupled MCF can be simply expressed as

$$\begin{aligned}\mathrm{SNR}_{\mathrm{MC}} &= \frac{P_{\mathrm{Tx},ch} - P_{\mathrm{XT}}}{P_{\mathrm{ASE}}|_{B_{\mathrm{noise}}=R_{\mathrm{symbol}}} + P_{\mathrm{NLI}}|_{B_{\mathrm{noise}}=R_{\mathrm{symbol}}} + P_{\mathrm{XT}}} \\ &\approx \frac{P_{\mathrm{Tx},ch}}{P_{\mathrm{ASE}}|_{B_{\mathrm{noise}}=R_{\mathrm{symbol}}} + P_{\mathrm{NLI}}|_{B_{\mathrm{noise}}=R_{\mathrm{symbol}}} + P_{\mathrm{XT}}}, \qquad \left(P_{\mathrm{Tx},ch} \gg P_{\mathrm{XT}}\right),\end{aligned} \tag{5.7}$$

where P_{XT} is the power of the XT from or to the certain core. In Eq. 5.7, $P_{\mathrm{Tx},ch}$s equivalent between all cores and losses equivalent between all cores are assumed. "$-P_{\mathrm{XT}}$" in the numerator represents the XT from the certain core to other cores, and "$+P_{\mathrm{XT}}$" in the denominator represents the XT from other cores to the certain core. However, "$-P_{\mathrm{XT}}$" is negligible in the case of low XT ($P_{\mathrm{Tx},ch} \gg P_{\mathrm{XT}}$). Depending on system capability, P_{XT} may have some different definitions. If skew between cores is small and thus pulse broadening due to multi-path interference (MPI) can be mitigated by digital signal processing, P_{XT} can simply be the power of light that is input to all cores

Table. 5.3: The symbols in Eqs. 5.3–5.6.

Symbols	Definitions
$P_{\mathrm{Tx},ch}$	The average power of transmitted light per channel.
P_{ASE}	The average power of the ASE noise within the bandwidth B_{noise}.
P_{NLI}	The average power of the nonlinear interference (NLI) within the bandwidth B_{noise}.
B_{noise}	The OSNR noise bandwidth.
N_{span}	The number of spans.
L_{span}	The span length.
F	The noise figure of optical amplifier.
α	The power loss coefficient [/(unit length)].
h	The Planck's constant.
ν	The center frequency of WDM comb.
γ	The nonlinear coefficient. $\gamma = 2\pi n_2/(\lambda A_{\mathrm{eff}})$, where n_2 is the nonlinear refractive index.
L_{eff}	The effective length. $L_{\mathrm{eff}} = \left[1-\exp\left(-\alpha L_{\mathrm{span}}\right)\right]/\alpha$.
β_2	The second derivative [(unit time)^2/(unit length)] of β with respect to ω, which is related to the chromatic dispersion D_{chrom} as $\beta_2 \equiv \frac{d^2\beta}{d\omega^2} = -\lambda^2 \frac{D_{\mathrm{chrom}}}{2\pi c}$.
N_{ch}	The number of WDM channels.
R_{symbol}	The symbol rate.
B_{WDM}	The WDM bandwidth. $B_{\mathrm{WDM}} = N_{\mathrm{ch}} R_{\mathrm{symbol}}$ in this chapter, because the Nyquist WDM is assumed.

except the certain core and output from the certain core. If the skew is very large and thus the MPI cannot be mitigated, P_{XT} can be the power of light that is input to all cores, coupled between cores, and output from the certain core. But in either case, if the XT is adequately low (i.e., $\mu_X <\sim 0.01$), P_{XT} can be related to $P_{\mathrm{Tx},ch}$ by μ_X as

$$P_{\mathrm{XT}} \approx \mu_X P_{\mathrm{Tx},ch}. \tag{5.8}$$

In the following discussion, we discuss the case of a core (the worst core) to which total μ_X from other cores is highest. When the XT is adequately low and XT between non-adjacent cores is negligible, the total μ_X ($\mu_{X,\mathrm{WC}}$) to the worst core can be approximated as

$$\mu_{X,\mathrm{WC}} \approx H_{\mathrm{WC}} N_{\mathrm{span}} L_{\mathrm{span}}, \tag{5.9}$$

$$H_{\mathrm{WC}} \approx N_{\mathrm{nc}} H, \tag{5.10}$$

where H_{WC} is the aggregate power-coupling coefficient to the worst core, and N_{nc} is the maximal number of the

neighboring cores. Equations 5.3, 5.7–5.10 yield

$$\begin{aligned}\mathrm{SNR}_{\mathrm{MC}}^{-1} &\approx \mathrm{SNR}_{\mathrm{SC}}^{-1} + \mu_{X,\mathrm{WC}} \\ &\approx \mathrm{SNR}_{\mathrm{SC}}^{-1} + H_{\mathrm{WC}} N_{\mathrm{span}} L_{\mathrm{span}}.\end{aligned} \tag{5.11}$$

Then SNR penalty due to XT can be expressed as

$$\frac{\mathrm{SNR}_{\mathrm{SC}}}{\mathrm{SNR}_{\mathrm{MC}}} \approx 1 + \mathrm{SNR}_{\mathrm{SC}} \mu_{X,\mathrm{WC}}. \tag{5.12}$$

Figures of merit of fibers can be evaluated by comparing maximal SNRs achievable in the same system using the different fibers. In both of the SC and MC cases, SNRs are maximized at

$$P_{\mathrm{Tx},ch} = \left(\frac{P_{\mathrm{ASE}}}{2a_{\mathrm{NLI}}} \right)^{\frac{1}{3}}. \tag{5.13}$$

Therefore, the maximal SNR ($\mathrm{SNR}_{\mathrm{SC,max}}$) achievable in a SC system can be derived as

$$\begin{aligned}\mathrm{SNR}_{\mathrm{SC,max}} &= \left[3 \left(\frac{P_{\mathrm{ASE}}}{2} \right)^{\frac{2}{3}} a_{\mathrm{NLI}}^{\frac{1}{3}} \right]^{-1} \Bigg|_{B_{\mathrm{noise}}=R_{\mathrm{symbol}}} \\ &\approx \left\{ \left[\frac{\left(e^{\alpha L_{\mathrm{span}}} - 1 \right)^{\frac{2}{3}} (\gamma L_{\mathrm{span}})^{\frac{2}{3}}}{(|\beta_2| L_{\mathrm{span}})^{\frac{1}{3}}} \right] \left[\ln \left(\pi^2 |\beta_2| L_{\mathrm{eff}} B_{\mathrm{WDM}}^2 \right) \right]^{\frac{1}{3}} \left[\left(\frac{2}{\pi} \right)^{\frac{1}{3}} N_{\mathrm{span}} (F \mathrm{h} \nu)^{\frac{2}{3}} \right] \right\}^{-1} \\ &\approx \left[\frac{\left(e^{\alpha L_{\mathrm{span}}} - 1 \right)^{\frac{2}{3}} (\gamma L_{\mathrm{eff}})^{\frac{2}{3}}}{(|\beta_2| L_{\mathrm{eff}})^{\frac{1}{3}}} \right]^{-1} \frac{\mathrm{C}_{\mathrm{system}}}{N_{\mathrm{span}}},\end{aligned} \tag{5.14}$$

where $\mathrm{C}_{\mathrm{system}}/N_{\mathrm{span}}$ includes the second and third bracket terms in the second line. When assuming moderately high $|\beta_2|$ and adequately broad B_{WDM}, $\mathrm{C}_{\mathrm{system}}/N_{\mathrm{span}}$ can be cancelled out by taking a ratio of $\mathrm{SNR}_{\mathrm{SC,max}}$s in the same system between different fibers. Accordingly, a figure of merit of a single-core fiber can be expressed only by the bracket term in the last line. Especially in case that , $\mathrm{SNR}_{\mathrm{SC,max}}$s in [dB] can be approximately obtained as

$$\mathrm{SNR}_{\mathrm{SC,max,dB}} \approx \frac{1}{3} \left[10 \log_{10} (|\beta_2|) - 20 \log_{10} (\gamma L_{\mathrm{eff}}) - 2\alpha_{\mathrm{dB}} L_{\mathrm{span}} \right] + 10 \log_{10} \frac{\mathrm{C}_{\mathrm{system}}}{N_{\mathrm{span}}}. \tag{5.15}$$

Based on Eqs. 5.14 and 5.15, a difference ($\Delta\mathrm{SNR}_{\mathrm{SC}}$) between $\mathrm{SNR}_{\mathrm{SC,max,dB}}$ between different fibers can be expressed only with the fiber parameters and L_{span}. From Eqs. 5.11 and 5.14, the maximal SNR ($\mathrm{SNR}_{\mathrm{MC,max}}$) in a

MC system can be expressed as

$$\begin{aligned}
\mathrm{SNR}_{\mathrm{MC,max}} &\approx \left(\mathrm{SNR}_{\mathrm{SC,max}}^{-1} + \mu_{X,\mathrm{WC}}\right)^{-1} \\
&\approx \left\{ \left[\frac{\left(e^{\alpha L_{\mathrm{span}}} - 1\right)^{\frac{2}{3}} (\gamma L_{\mathrm{eff}})^{\frac{2}{3}}}{(|\beta_2| L_{\mathrm{eff}})^{\frac{1}{3}}} \right] \frac{N_{\mathrm{span}}}{\mathrm{C}_{\mathrm{system}}} + \mu_{X,\mathrm{WC}} \right\}^{-1} \\
&\approx \left\{ \left[\frac{\left(e^{\alpha L_{\mathrm{span}}} - 1\right)^{\frac{2}{3}} (\gamma L_{\mathrm{eff}})^{\frac{2}{3}}}{(|\beta_2| L_{\mathrm{eff}})^{\frac{1}{3}}} \right] \frac{1}{\mathrm{C}_{\mathrm{system}}} + H_{\mathrm{WC}} L_{\mathrm{span}} \right\}^{-1} \frac{1}{N_{\mathrm{span}}}.
\end{aligned} \tag{5.16}$$

Based on Eq. 5.16, a difference ($\Delta\mathrm{SNR}_{\mathrm{MC}}$) of $\mathrm{SNR}_{\mathrm{MC,max}}$ in [dB] between different fibers cannot be expressed only with the fiber parameters and L_{span}. Only N_{span} can be cancelled out in $\Delta\mathrm{SNR}_{\mathrm{MC}}$ and other system parameters ($\mathrm{C}_{\mathrm{system}}$) cannot be cancelled out. However, in both SC and MC cases, we can obtain ΔSNR independent of N_{span}, and SNR penalty due to XT independent of N_{span}:

$$\begin{aligned}
\frac{\mathrm{SNR}_{\mathrm{SC,max}}}{\mathrm{SNR}_{\mathrm{MC,max}}} &\approx 1 + \mathrm{SNR}_{\mathrm{SC,max}} \mu_{X,\mathrm{WC}} \\
&\approx 1 + \frac{\mathrm{SNR}_{\mathrm{SC,max}}\big|_{N_{\mathrm{span}}=1}}{N_{\mathrm{span}}} H_{\mathrm{WC}} N_{\mathrm{span}} L_{\mathrm{span}} \\
&\approx 1 + \left(\mathrm{SNR}_{\mathrm{SC,max}}\big|_{N_{\mathrm{span}}=1}\right) \left(H_{\mathrm{WC}} L_{\mathrm{span}}\right).
\end{aligned} \tag{5.17}$$

5.4.2 Comparison of SNRs Between SSMF, Reported MCFs, and the Fabricated MCFs

Based on the above consideration, we can evaluate the effects of the fiber parameters (including the XT) on SNR. Figure 5.6 shows how the $\mathrm{SNR}_{\mathrm{SC,max}}$ and the worst-core μ_X after one span affect SNR penalty due to XT and $\Delta\mathrm{SNR}_{\mathrm{MC}}$ in cases of L_{span} = 80 km and L_{span} = 100 km. In Fig. 5.6, the $\mathrm{SNR}_{\mathrm{SC,max}}$s and the μ_Xs of the various reported MCFs and the fabricated MCFs—their characteristics are listed in Table 5.4— are plotted as red diamonds, and the $\mathrm{SNR}_{\mathrm{SC,max}}$ of SSMF are plotted as dashed lines. The $\mathrm{SNR}_{\mathrm{SC,max}}$s were calculated using Eq. 5.14 in case of B_{WDM} = 10 THz and F_{dB} = 4 dB. The SNR penalty due to XT was calculated using Eqs. 5.14 and 5.17, and shown as blue dot-dashed isolines. As shown in the graphs, $\mathrm{SNR}_{\mathrm{SC,max}}$s—that is, SNR without XT— of many of the reported MCFs were calculated to be improved from that of the SSMF. However, SNR in uncoupled MCFs can be degraded by XT as is shown in the blue dot-dashed lines. In order to preserve the $\Delta\mathrm{SNR}_{\mathrm{MC}}$ unaffected by XT, μ_X per L_{span} of the MCF have to be suppressed adequately lower than ASE and NLI noises per L_{span}. Based on the $\mathrm{SNR}_{\mathrm{SC,max}}$ and the SNR penalty, or on Eq. 5.16, $\Delta\mathrm{SNR}_{\mathrm{MC}}$ from the SSMF can be obtained and are plotted

as solid curves. The XT of the fabricated MCF was well suppressed, and ΔSNR_{MC} of the MCF can be achieved to be 2.4 dB for L_{span} = 80 km and 2.9 dB for L_{span} = 100 km compared to the SSMF, which are the highest in reported MCFs, to the best of our knowledge. The SNR penalties due to XT were calculated to be 0.4 dB for L_{span} = 80 km and 0.2 dB for L_{span} = 100 km.

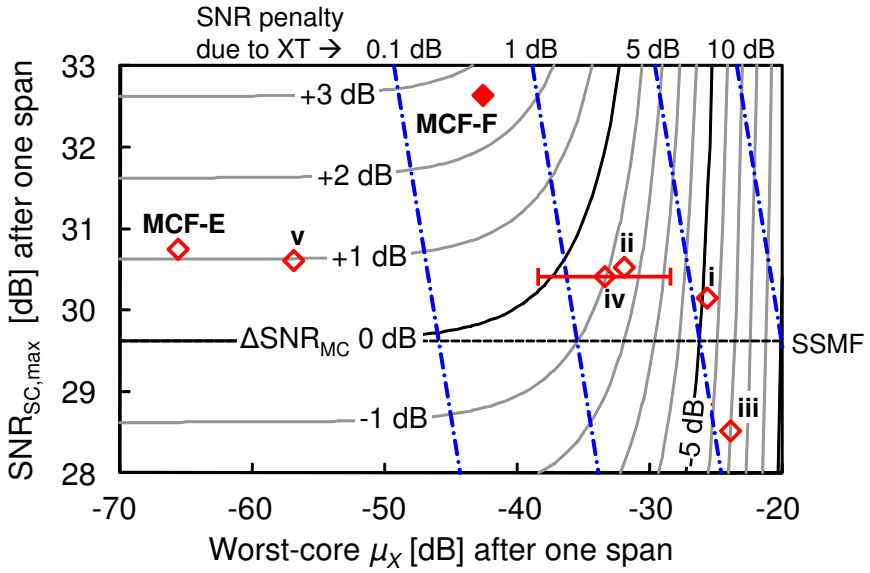

(a) L_{span} = 80 km.

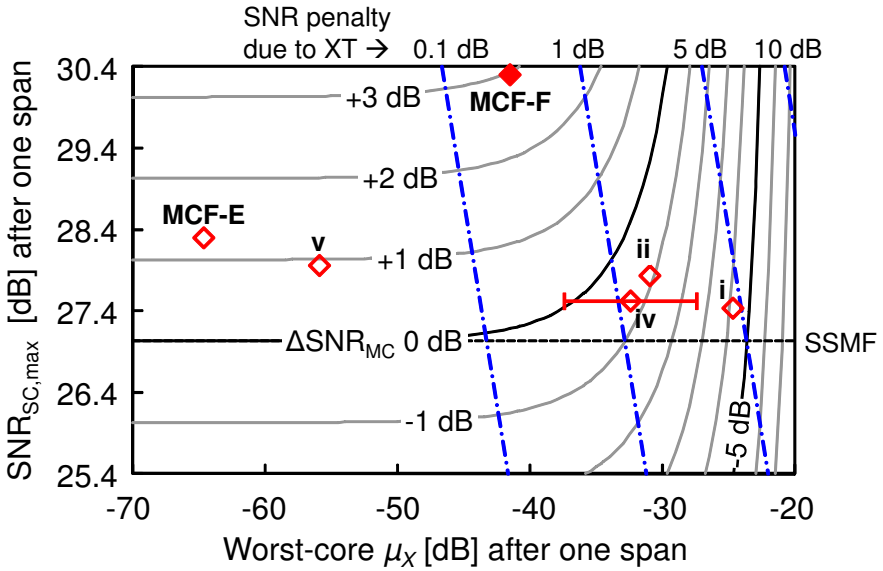

(b) L_{span} = 100 km.

Fig. 5.6: Dependences of SNR penalty due to XT and of relative SNR of MCFs compared to SSMF (ΔSNR_{MC}), on the SNR without XT (SNR_{SC}) and the worst-core μ_X after one span. Dot-dashed lines: isolines of SNR penalty due to XT, solid curves: isolines of ΔSNR_{MC}, dashed lines: $SNR_{SC,max}$ of SSMF.

Table. 5.4: Characteristics of SSMF, reported MCFs, and the fabricated MCFs at 1550 nm.

Notations in Fig. 5.6.	Ref.	Transmission loss [dB/km]	A_{eff} [μm^2]	D_{chrom} [ps/(nm · km)]	μ_X [dB]	L [km]	N_{nc}	Worst-core μ_X [dB] after 80 km	Worst-core μ_X [dB] after 100 km
SSMF		0.19	80	16.7			0		
MCF-E	Chapter 3	0.178[a]	80[a]	22.2[a]	−79.5[a]	17.4	6	−65.7[b]	−64.7[b]
i	[60]	0.20	102	N/A[c]	∼ −53.5	∼ 0.8	6	∼ −25.7	∼ −24.7
ii	[61]	0.198	112.4	N/A[c]	−56	1.905	6	−32	−31
iii	[62]	0.242	116	N/A[c]	−40	3.962	2	−24	−23
iv	[63]	0.214[a]	133.4[a]	20.6[a]	−53.5 to −43.5	5.0	2	−38.4 to −28.4	−37.5 to −27.5
v	[64]	0.195	110	0.7	−65	75	6	−56.9	−56.0
MCF-F	This chapter	0.168[a]	124.1[a]	21.7[a]	−61.3[a]	6.99	6	−42.5[b]	−41.5[b]

[a] Average of all cores.

[b] Calculated directly from the center-core μ_X.

[c] 21 ps/(nm · km)was assumed in the calculation.

[*] n_2 was assumed to be 2.2×10^{-20} m^2/W for PSCF and 2.34×10^{-20} m^2/W for Ge-doped fiber in the calculation.

The appropriate suppression level of the XT may also depend on the system parameters. Figure 5.7 shows the relationships between the worst-core μ_X after one span and the SNR penalty due to XT in an MCF with SSMF core ($\Delta\mathrm{SNR}_{\mathrm{SC}} = 0$ dB), for combinations of system parameters of $F_{\mathrm{dB}} = 3, 4, 5, 6$ dB and $B_{\mathrm{WDM}} = 5, 10$ THz, in the case of $L_{\mathrm{span}} = 80$ km, which is more severe than $L_{\mathrm{span}} = 100$ km. In these traces, the case of $F_{\mathrm{dB}} = 3$ dB and $B_{\mathrm{WDM}} = 5$ THz is the most severe for the SNR penalty suppression, since the ASE and NLI noises are the lowest. In the most severe case, the worst-core μ_X should be less than -46.8 dB after one 80-km span for suppressing the SNR penalty less than 0.1 dB, -39.6 dB for 0.5-dB penalty, and -36.3 dB for 1-dB penalty. Based on Eq. 5.17, the SNR penalty can be constant if an increase in an $\mathrm{SNR}_{\mathrm{SC,max}}$ is cancelled by a decrease in XT. Accordingly, horizontal offsets of the curves in Fig. 5.7 are equivalent to the difference in the $\mathrm{SNR}_{\mathrm{SC,max}}$ between the cases, which can be induced by the SNR improvement from the system parameters or fiber parameters. For example, in the case of MCF-F, since the $\mathrm{SNR}_{\mathrm{SC,max}}$ for $L_{\mathrm{span}} = 80$ km was increased by 2.8 dB from the SSMF ($\Delta\mathrm{SNR}_{\mathrm{SC}} = 2.8$ dB), we need to suppress the worst-core μ_X 2.8 dB further from the above values.

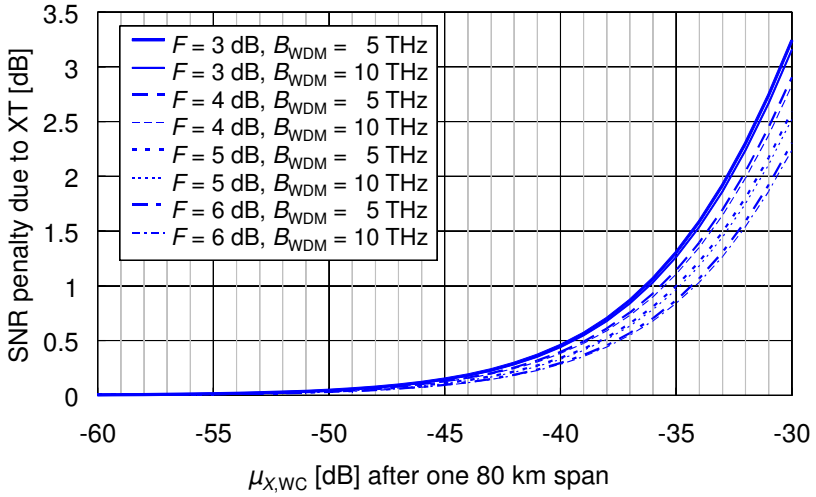

Fig. 5.7: Relationships between the worst-core μ_X after one span and the SNR penalty due to XT for several combinations of system parameters in case of $L_{\mathrm{span}} = 80$ km.

5.5 Conclusion of This Chapter

We designed and fabricated an MCF that simultaneously achieves transmission losses of 0.17 dB/km or lower, effective areas larger than 120 $\mu\mathrm{m}^2$, and a total mean crosstalk to the center core equivalent to -42.5 dB after 80 km, at 1550 nm. We investigated SNR under the existence of inter-core crosstalk in uncoupled MCF, and found that the SNR in the fabricated MCF can be estimated to be improved more than 2 dB from SSMF even under the existence of the crosstalk. Based on the investigation, the total mean crosstalk to the worst core of an MCF should

be less than about -47 dB after 80 km for SNR penalty due to crosstalk less than 0.1 dB, about -40 dB for 0.5-dB penalty, and about -36 dB for 1-dB penalty, even in the case of an MCF with SSMF cores.

Further SNR enhancement in each core of the MCF can be realized by improving transmission loss and by finding a good balance between large effective area and low crosstalk, so that the SNR under crosstalk can be maximized.

Chapter 6

Behavior of Inter-Core Crosstalk: Effects of Macrobend and Structure Fluctuation

6.1 Introduction to This Chapter

After a few years of the intensive research by various groups, the characteristics of inter-core crosstalk (XT) of the multi-core fiber (MCF) have been elucidated, as described in the previous chapters and Refs. [55, 65–67].

In this chapter, we review the essence of these studies on the XT, clarify ambiguous points of the studies, and derive a novel expression of the average power-coupling coefficient, with which we can understand the behavior of the XT and interpret its physical meaning easily. Based on the derived expression, we discuss how the longitudinal fluctuation of fiber structures and the macrobend can affect the XT, and organize the previously-reported methods for XT suppression.

6.2 Brief Review on the Coupled-Mode Theory

Formulations in the previous chapters are based on the conventional coupled-mode theory (CMT) [31], which is called orthogonal CMT, since orthogonality of the core modes is assumed. In the orthogonal CMT, the mode-coupling coefficient is defined as

$$\kappa_{nm} \equiv \frac{\omega\varepsilon_0 \iint \left(n^2 - n_m^2\right) \boldsymbol{e}_n^* \cdot \boldsymbol{e}_m \, dxdy}{\iint \hat{z} \cdot \left(\boldsymbol{e}_n^* \times \boldsymbol{h}_n + \boldsymbol{e}_n \times \boldsymbol{h}_n^*\right) dxdy}, \tag{6.1}$$

where $\omega = 2\pi c/\lambda$ is the angular frequency, c is the speed of light in vacuum, n is the actual index profile, n_m is the index profile of Core m in the absence of the other cores, $\boldsymbol{e}$ and $\boldsymbol{h}$ are the normalized vector core modes of the electric and magnetic fields, respectively, the superscript * indicates the complex conjugate, and $\hat{z}$ is the unit vector of the positive z-axis. Although the mode-coupling coefficients should be symmetric as

$$\kappa_{nm} = \kappa_{mn}^* \tag{6.2}$$

for power conservation in loss-less systems, they are asymmetric between non-identical cores; therefore the orthogonal CMT with non-identical cores is not self-consistent [68]. To cope with such problem, the nonorthogonal CMT was developed [69–71], which was formulated using the cross power term:

$$P_{nm} \equiv \frac{\iint \hat{z} \cdot \left(\boldsymbol{e}_n^* \times \boldsymbol{h}_m + \boldsymbol{e}_m \times \boldsymbol{h}_n^* \right) dx\,dy}{\iint \hat{z} \cdot \left(\boldsymbol{e}_n^* \times \boldsymbol{h}_n + \boldsymbol{e}_n \times \boldsymbol{h}_n^* \right) dx\,dy}. \tag{6.3}$$

In the nonorthogonal CMT, the coupled-mode equation (CME) is expressed as [72]:

$$\boldsymbol{P} \frac{d\boldsymbol{E}}{dz} = -j\boldsymbol{T}\boldsymbol{E}, \tag{6.4}$$

where $\boldsymbol{P}$ is the power matrix associated with the core modes whose elements are expressed as Eq. 6.3—the diagonal elements equal to 1, and the off-diagonal elements are the cross-power due to the mode nonorthogonality—, and $\boldsymbol{T}$ is the overall (Hermitian) transfer/coupling matrix whose elements are represented as

$$T_{nm} = P_{nm}\beta_m + \kappa_{nm}. \tag{6.5}$$

The mode evolutions can be solved by rewriting Eq. 6.4 as

$$\frac{d\boldsymbol{E}}{dz} = -j\boldsymbol{P}^{-1}\boldsymbol{T}\boldsymbol{E}. \tag{6.6}$$

In the simple two core case, Equation 6.6 can be rewritten as

$$\begin{cases} \dfrac{dE_1}{dz} = -j\dfrac{\kappa_{12} - P_{12}\kappa_{22}}{1 - P_{12}P_{21}} E_2 - j\left(\beta_1 + \dfrac{\kappa_{11} - P_{12}\kappa_{21}}{1 - P_{12}P_{21}} \right) E_1, \\ \dfrac{dE_2}{dz} = -j\dfrac{\kappa_{21} - P_{21}\kappa_{11}}{1 - P_{12}P_{21}} E_1 - j\left(\beta_2 + \dfrac{\kappa_{22} - P_{21}\kappa_{12}}{1 - P_{12}P_{21}} \right) E_2, \end{cases} \tag{6.7}$$

or

$$\begin{cases} \dfrac{dA_1}{dz} = -j\dfrac{\kappa_{12} - P_{12}\kappa_{22}}{1 - P_{12}P_{21}} \exp\left[j(\beta_1 - \beta_2) \right] A_2 - j\dfrac{\kappa_{11} - P_{12}\kappa_{21}}{1 - P_{12}P_{21}} A_1, \\ \dfrac{dA_2}{dz} = -j\dfrac{\kappa_{21} - P_{21}\kappa_{11}}{1 - P_{12}P_{21}} \exp\left[j(\beta_2 - \beta_1) \right] A_1 - j\dfrac{\kappa_{22} - P_{21}\kappa_{12}}{1 - P_{12}P_{21}} A_2, \end{cases} \tag{6.8}$$

which are well-known forms of the nonorthogonal CME.

The reciprocity of the coupling coefficients:

$$\frac{\kappa_{12} - P_{12}\kappa_{22}}{1 - P_{12}P_{21}} = \left(\frac{\kappa_{21} - P_{21}\kappa_{11}}{1 - P_{12}P_{21}} \right)^* \tag{6.9}$$

is also necessary for the power conservation in the nonorthogonal CME; however, even in the case of the nonorthogonal CME, Eq. 6.9 cannot completely hold for the heterogeneous MCF, because the coupled-mode expressions with limited modes are just an approximation of the exact solution of the Maxwell's equations. In the case of the low-XT MCF, the cross-power can be negligibly low, thus Eqs. 6.4–6.9 can be reduced to the orthogonal CMT, and the reciprocity assumption of Eq. 6.9 also can be reduced to Eq. 6.2. However, when the power confinements of dissimilar cores are very different as shown in Fig. 6.1, the mode-coupling coefficient cannot be reciprocal, because the mode-coupling coefficient is the overlap integral of the modes within the permittivity perturbation, as shown in Eq. 6.1.

To cope with this problem, Refs. [55, 72, 73] proposed to redefine the coupling coefficients as[*1]

$$\bar{\kappa}_{nm} = \bar{\kappa}_{mn} \equiv \frac{\kappa_{nm} + \kappa_{mn}}{2}. \tag{6.10}$$

In the case of the low-XT MCF, the cross-power can be assumed to be well suppressed; therefore, the orthogonal CMT with the redefined mode-coupling coefficient can be employed for theoretical considerations. In this thesis, the mode-coupling coefficients κ in the equations are not barred explicitly, but the redefined mode-coupling coefficient should be used for the heterogeneous MCF.

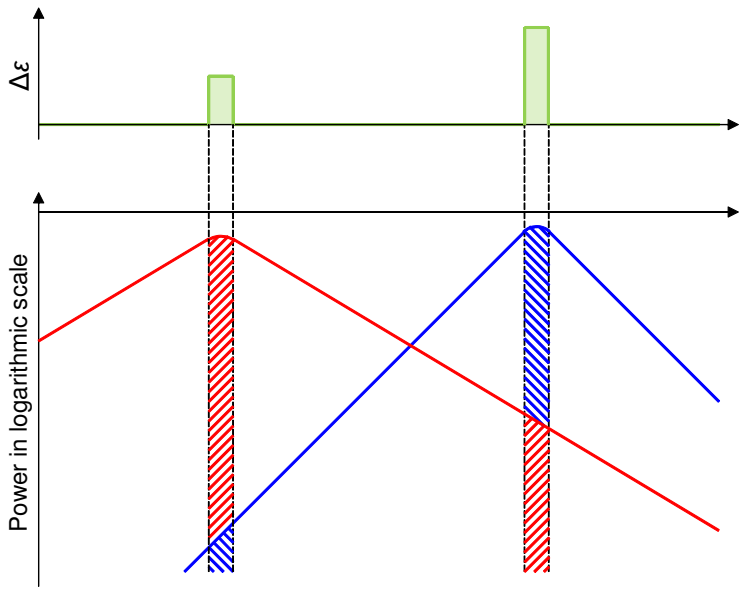

Fig. 6.1: Schematic illustration of the profiles of the the permittivity and the core-mode powers of two dissimilar cores.

[*1] To be exact, Refs. [72, 73] symmetrized the coupling coefficients of nonorthogonal CME by averaging them, and Ref. [55] redefined the coupling coefficients of the nonorthogonal CME so that they can be equal to their average. See the references for more details.

6.3 Review and Clarification of Derivations of Power-Coupling Coefficient in Earlier Studies

In this section, we review the derivation of the power-coupling coefficient between cores from the longitudinally perturbed coupled-mode equation. We also clarify an ambiguous point of the definition of power spectral density in the derivation.

Since the propagation constants of cores in the MCF are perturbed by bend, twist, structure fluctuation, and so on, the coupling between cores in the MCF can be described using the coupled-power equation. The power-coupling coefficient can be derived from the coupled-mode equation with longitudinally perturbed propagation constants. The coupled-mode equation can be expressed as

$$\begin{aligned}\frac{dA_n}{dz} &= -j\kappa_{nm}\exp\left[-j\int_0^z(\beta_m-\beta_n)\,dz\right]A_m \\ &= -j\kappa_{nm}\exp\left[-j\left(\beta_{\mathrm{c},m}-\beta_{\mathrm{c},n}\right)z-j\int_0^z\left(\beta_{\mathrm{v},m}-\beta_{\mathrm{v},n}\right)dz\right]A_m,\end{aligned} \tag{6.11}$$

where A is the complex amplitude, κ_{nm} the mode-coupling coefficient from Core n to Core m, $\beta = 2\pi n_{\mathrm{eff}}/\lambda$ the propagation constant, n_{eff} the effective refractive index, and λ the wavelength. Subscripts c and v of β represent the *constant* part and the *variable* perturbed part of β, respectively.

Based on Eq. 6.11, in the case of low XT, the XT in amplitude within the fiber segment $[z_1, z_2]$ can be expressed as

$$\Delta x_{nm} = \frac{\Delta A_n}{A_m} \approx -j\kappa_{nm}\int_{z_1}^{z_2}\exp\left[-j\left(\beta_{\mathrm{c},m}-\beta_{\mathrm{c},n}\right)z\right]f(z)\,dz, \tag{6.12}$$

by using

$$f(z) \equiv \exp\left\{-j\int_0^z\left[\beta_{\mathrm{v},m}\left(z'\right)-\beta_{\mathrm{v},n}\left(z'\right)\right]dz'\right\}. \tag{6.13}$$

Accordingly, the mean XT increase in power within the segment $[z_1, z_2]$ can be expressed as

$$\begin{aligned}\langle\Delta X_{nm}\rangle &= \left\langle\left|\Delta x_{nm}\right|^2\right\rangle = \left\langle\Delta x_{nm}\Delta x_{nm}^*\right\rangle \\ &\approx \kappa_{nm}^2\int_{z_1}^{z_2}\int_{z_1}^{z_2}\exp\left[-j\left(\beta_{\mathrm{c},m}-\beta_{\mathrm{c},n}\right)\left(z-z'\right)\right]\left\langle f(z)f^*\left(z'\right)\right\rangle dz\,dz' \\ &\approx \kappa_{nm}^2\int_{z_1}^{z_2}\int_{z_1-z'}^{z_2-z'}\exp\left[j\Delta\beta_{\mathrm{c},nm}\zeta\right]\left\langle f\left(z'+\zeta\right)f^*\left(z'\right)\right\rangle d\zeta\,dz' \\ &\approx \kappa_{nm}^2\int_{z_1}^{z_2}dz'\int_{-\infty}^{\infty}R_{ff}(\zeta)\exp\left(j\Delta\beta_{\mathrm{c},nm}\zeta\right)d\zeta \\ &\approx \kappa_{nm}^2\Delta z\int_{-\infty}^{\infty}R_{ff}(\zeta)\exp\left(j\Delta\beta_{\mathrm{c},nm}\zeta\right)d\zeta,\end{aligned} \tag{6.14}$$

where R_{ff} is the autocorrelation function (ACF) of $f(z)$, Δz is $z_2 - z_1$, and the correlation length l_{cor} of R_{ff} is assumed to be adequately shorter than Δz. $R_{ff}(\zeta)$ can be understood as the correlation between the coupled and non-coupled lights that are propagated for the length of ζ after the coupling. For example, where $\zeta \gg l_{\mathrm{cor}}$, the coupled and non-coupled lights lose their coherency even if the lights are very coherent. Based on the Wiener–Khinchin theorem, the power spectrum density (PSD) is the Fourier transform of the ACF:

$$S_{ff}^{(\tilde{\nu})}(\tilde{\nu}) = \int_{-\infty}^{\infty} R_{ff}(\zeta) \exp(j2\pi\tilde{\nu}\zeta)\, d\zeta, \tag{6.15}$$

where $\tilde{\nu} = n_{\mathrm{eff}}/\lambda = \beta/(2\pi)$ represents the wave number (or spatial frequency) in the medium-whereas the propagation constant β is the angular wave number. Note that $\tilde{\nu}$, n_{eff}, and β have common subscripts, e.g., $\tilde{\nu}_{\mathrm{c}} = n_{\mathrm{eff,c}}/\lambda = \beta_{\mathrm{c}}/(2\pi)$. To describe the PSDs with respect to $\tilde{\nu}$ and β with common expressions, we would like to define the PSD with respect to β, whose total power is equivalent to Eq. 6.15. From the Parseval's theorem, the average power of $f(z)$, or expected value of $|f(z)|^2$, is equivalent to the integral of the PSD over whole $\tilde{\nu}$, and the following equation holds between $f(z)$ and the PSDs of $f(z)$:

$$\int_{-\infty}^{\infty} S_{ff}^{(\tilde{\nu})}(\tilde{\nu})\, d\tilde{\nu} = \int_{-\infty}^{\infty} S_{ff}^{(\tilde{\nu})}(\tilde{\nu}) \frac{d\tilde{\nu}}{d\beta} d\beta = \mathrm{E}\left[|f(z)|^2\right] = 1, \tag{6.16}$$

where $\mathrm{E}[\cdot]$ represents the expected value. Therefore, in this paper, the PSD $S_{ff}^{(\beta)}(\beta)$ with the scale of the propagation constant β (the angular wave number in the medium) is defined as:

$$S_{ff}^{(\beta)}(\beta) \equiv S_{ff}^{(\tilde{\nu})}(\tilde{\nu}) \frac{d\tilde{\nu}}{d\beta} = \frac{1}{2\pi} S_{ff}^{(\tilde{\nu})}(\tilde{\nu}) = \frac{1}{2\pi} \int_{-\infty}^{\infty} R_{ff}(\zeta) \exp(j\beta\zeta)\, d\zeta. \tag{6.17}$$

From Eqs. 6.14 and 6.17, the power-coupling coefficient can be expressed as

$$H_{nm} = \frac{\langle \Delta X_{nm} \rangle}{\Delta z} \approx \kappa_{nm}^2 S_{ff}^{(\tilde{\nu})}\left(\frac{\Delta n_{\mathrm{eff,c},nm}}{\lambda}\right) = \kappa_{nm}^2 \left[2\pi S_{ff}^{(\beta)}(\Delta\beta_{\mathrm{c}nm})\right]. \tag{6.18}$$

Figure 6.2 shows the schematics of perturbations on β, or how β_{v} can vary. As shown in Figs. 6.2a and 6.2b, the bend and the structure fluctuation can induce a slight change in β_{v} in one core, which can occur ether in the single-core fiber or in the MCF. In the single-core fiber, by assuming proper R_{ff} or S_{ff} for the perturbations shown in Figs. 6.2a and 6.2b, Eq. 6.18 is utilized for analyzing the power coupling between modes in the multi-mode fiber, microbend loss—power coupling from the core modes to the cladding modes, and so on. In the MCF, as shown in Fig. 6.2c, the bend can induce relatively large β_{v} in a core when assuming another core as a reference of the propagation constant. Fini *et al.* [65] and Hayashi *et al.* [74] assumed that β_{v} in the MCF is induced by the

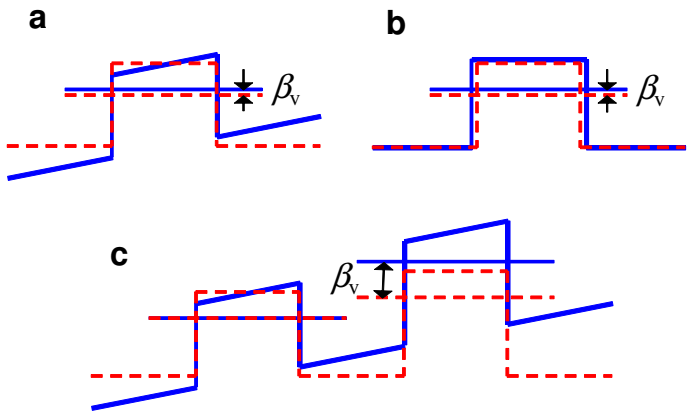

Fig. 6.2: Schematics of perturbations on the propagation constant. (a) a slight change of the propagation constant in a core due to bend, (b) a slight change of the propagation constant in a core due to structure fluctuation, and (c) a bend-induced change of the propagation constant in a core when assuming another core as a reference of the propagation constant.

macrobend and twist of the MCF as

$$\beta_{v,n} = \beta_{c,n} \frac{x_n \cos\theta_{fib}(z) - y_n \sin\theta_{fib}(z)}{R_b(z)} = \beta_{c,n} \frac{r_n \cos\theta_n(z)}{R_b(z)}, \tag{6.19}$$

and investigated the XT characteristics of the MCFs. Here, (x_n, y_n) and (r_n, θ_n) are the local Cartesian and polar coordinates of Core n in a fiber cross-section, respectively, $\theta = 0$ is the radial direction of the macrobend, θ_{fib} the angle between the x-axis and the radial direction of the macrobend, and R_b the macrobend radius of the MCF-that is, the distance between the center of the macrobend and the origin of the local coordinates.

However, it is not easy to assume a proper β_v, R_{ff}, or S_{ff} that can include the perturbations of both the bend and the structure fluctuation. Therefore, by assuming that R_{ff} includes only the effect of structure fluctuation and does not include that of macrobend and twist, Koshiba *et al.* investigated the effects of correlation length l_{cor} and of the shape of the ACF R_{ff} on the mean XT μ_X [55,75]. They investigated some types of R_{ff}, and found that the exponential ACF (EAF):

$$R_{ff}(\zeta) = \exp\left(\frac{-|\zeta|}{l_{cor}}\right) \tag{6.20}$$

is proper for estimating actual μ_X of the MCFs. The EAF have been introduced to microbend loss analysis [76]. Since the PSD of the EAF is the Lorentzian distribution, the power-coupling coefficient was obtained from Eq. 6.15

as [55, 75]:

$$H_{nm}(z) = \kappa_{nm}^2 \frac{1}{\pi} \frac{1/(2\pi l_{\mathrm{cor}})}{1/(2\pi l_{\mathrm{cor}})^2 + \left[\Delta n'_{\mathrm{eff,c},nm}(z)/\lambda\right]^2} = \kappa_{nm}^2 2\pi \frac{1}{\pi} \frac{1/l_{\mathrm{cor}}}{1/l_{\mathrm{cor}}^2 + \left[\beta'_{\mathrm{c},nm}(z)\right]^2}$$
$$= \kappa_{nm}^2 \frac{2l_{\mathrm{cor}}}{1 + \left[\Delta\beta'_{\mathrm{c},nm}(z)\, l_{\mathrm{cor}}\right]^2}, \tag{6.21}$$

where $\Delta\beta'_{\mathrm{c},nm}$ is $\beta'_{\mathrm{c},n} - \beta'_{\mathrm{c},m}$, and β'_{c} is redefined β_{c} that includes the effects of macrobend and twist:

$$\beta'_{\mathrm{c},n} = \beta_{\mathrm{c},n}\left[1 + \frac{x_n \cos\theta_{\mathrm{fib}}(z) - y_n \sin\theta_{\mathrm{fib}}(z)}{R_{\mathrm{b}}(z)}\right] = \beta_{\mathrm{c},n}\left[1 + \frac{r_n \cos\theta_n(z)}{R_{\mathrm{b}}(z)}\right]. \tag{6.22}$$

Mean XT μ_X estimated using coupled-power equation with the power-coupling coefficient of Eq. 6.21 may be valid in the cases where changes of R_{b} and θ are gradual enough compared to l_{cor}, since $\Delta\beta'_{\mathrm{c},nm}$—which is variable and includes macrobend and twist— is substituted to $\Delta\beta_{\mathrm{c},nm}$—which is constant— in Eq. 6.18.

6.4 Derivation of Average Power-Coupling Coefficient

To further understand the behavior and the physical meaning of the XT, we derive an expression of the average power-coupling coefficient, which is averaged over θ, in this section. For simplicity, the center of Core m is taken as the origin of the local coordinate, and accordingly $\Delta\beta'_{\mathrm{c},nm}$ can be written as

$$\Delta\beta'_{\mathrm{c},nm}(R_{\mathrm{b}}, \theta_{nm}) = \Delta\beta_{\mathrm{c},nm} + \Delta\beta_{\mathrm{b},nm}(R_{\mathrm{b}}, \theta_{nm}), \tag{6.23}$$

$$\Delta\beta'_{\mathrm{b},nm}(R_{\mathrm{b}}, \theta_{nm}) = \Delta\beta^{\mathrm{dev}}_{\mathrm{b},nm}(R_{\mathrm{b}}) \cos\theta_{nm}, \tag{6.24}$$

$$\Delta\beta^{\mathrm{dev}}_{\mathrm{b},nm}(R_{\mathrm{b}}) = \beta_{\mathrm{c},n} \frac{d_{nm}}{R_{\mathrm{b}}}, \tag{6.25}$$

where θ_{nm} represents the angle between the radial direction of the bend and a line segment from Core m to Core n, $\beta_{\mathrm{b},nm}$ the difference of β variation between Core m and Core n from the macrobend, $\beta^{\mathrm{dev}}_{\mathrm{b},nm}$ the peak deviation of $\beta_{\mathrm{b},nm}$, and d_{nm} is the center-to-center distance between Core m and Core n.

Let $p_{\theta_{nm}}(\theta_{nm})$ and $p_{R_{\mathrm{b}}}(R_{\mathrm{b}})$ be the probability density functions of θ_{nm} and of R_{b}, respectively, along the MCF; by assuming that $p_{\theta_{nm}}(\theta_{nm})$ and $p_{R_{\mathrm{b}}}(R_{\mathrm{b}})$ are statistically independent, the twist of the MCF is gradual enough, and mean XT is adequately low; the mean XT $\mu_{X,nm}$ from Core m to Core n can be expressed as

$$\mu_{X,nm}(L) \approx \int_0^L H_{nm}(z)\, dz \approx L\left[\frac{1}{L}\int_0^L H_{nm}(z)\, dz\right] \approx L\mathrm{E}[H_{nm}]$$
$$\approx L\int_0^\infty p_{R_{\mathrm{b}}}(R_{\mathrm{b}})\, \bar{H}_{nm}(R_{\mathrm{b}})\, dR_{\mathrm{b}}, \tag{6.26}$$

where the average power-coupling coefficient is

$$\bar{H}_{nm}(R_\mathrm{b}) = \int_0^{2\pi} p_{\theta_{nm}}(\theta_{nm}) H_{nm}(R_\mathrm{b}, \theta_{nm})\, d\theta_{nm}. \tag{6.27}$$

By assuming that the twist of the MCF is random enough and the MCF is adequately long, $p_{\theta_{nm}}(\theta_{nm})$ can be assumed to be constant ($\simeq 1/(2\pi)$) over all θ_{nm}; therefore, by substituting $\Delta\beta = -\Delta\beta_{\mathrm{b},nm}(R_\mathrm{b}, \theta_{nm}) = -\Delta\beta_{\mathrm{b},nm}^{\mathrm{dev}}(R_\mathrm{b})\cos\theta_{nm}$ and using Eq. 6.15 and $\sin(\arccos x) = \sqrt{1-x^2}$, Eq. 6.27 can be rewritten as

$$\begin{aligned}
\bar{H}_{nm}(R_\mathrm{b}) &= \int_0^{2\pi} \frac{1}{2\pi} h_{nm}(R_\mathrm{b}, \theta_{nm})\, d\theta_{nm} = \int_0^{2\pi} \frac{1}{2\pi} \kappa_{nm}^2 2\pi S_{ff}^{(\beta)} \left[\Delta\beta_{\mathrm{c},nm}(R_\mathrm{b}, \theta_{nm})\right] d\theta_{nm} \\
&= 2\int_0^{\pi} \kappa_{nm}^2 S_{ff}^{(\beta)} \left[\Delta\beta_{\mathrm{c}nm} + \Delta\beta_{\mathrm{b},nm}^{\mathrm{dev}}(R_\mathrm{b})\cos\theta_{nm}\right] d\theta_{nm} \\
&= 2\pi \int_{-\Delta\beta_{\mathrm{b},nm}^{\mathrm{dev}}}^{\Delta\beta_{\mathrm{b},nm}^{\mathrm{dev}}} \frac{\kappa_{nm}^2}{\pi\sqrt{\left[\Delta\beta_{\mathrm{b},nm}^{\mathrm{dev}}(R_\mathrm{b})\right]^2 - \Delta\beta^2}} S_{ff}^{(\beta)}\left(\Delta\beta_{\mathrm{c},nm} - \Delta\beta\right) d(\Delta\beta),
\end{aligned} \tag{6.28}$$

where S_{ff} is the Lorentzian distribution as shown in Eq. 6.21. By using the arcsine distribution:

$$p_{\Delta\beta_\mathrm{b}}(\Delta\beta_{\mathrm{c},nm}) = \begin{cases} \dfrac{1}{\pi\sqrt{\left(\Delta\beta_{\mathrm{b},nm}^{\mathrm{dev}}\right)^2 - \Delta\beta_{\mathrm{c},nm}^2}}, & \left|\Delta\beta_{\mathrm{c},nm}\right| \le \Delta\beta_{\mathrm{b},nm}^{\mathrm{dev}}, \\ 0, & \text{otherwise}, \end{cases} \tag{6.29}$$

which is the probability distribution of $\Delta\beta_\mathrm{b}$, Eq. 6.28 can be rewritten as

$$\bar{H}_{nm}(\Delta\beta_{\mathrm{c},nm}, R_\mathrm{b}) = \kappa_{nm}^2 2\pi \left(p_{\Delta\beta_\mathrm{b}} * S_{ff}^{(\beta)}\right)_{\Delta\beta}(\Delta\beta_{\mathrm{c},nm}) = \kappa_{nm}^2 \left(p_{\Delta\tilde{\nu}_\mathrm{b}} * S_{ff}^{(\tilde{\nu})}\right)_{\Delta\tilde{\nu}}(\Delta\tilde{\nu}_{\mathrm{c},nm}), \tag{6.30}$$

where the expression of $(f * g)_x$ denotes the convolution of f and g with respect to x, and the expression with respect to $\tilde{\nu}$ is also shown for comparison. If we consider the case where PSD S_{ff} in Eq. 6.15 includes both the effects of the structure fluctuation and the macrobend, the convolution term in Eq. 6.30 may be understood as the PSD S_{ff} in Eq. 6.15.

Particularly where $\left|\Delta\beta_{\mathrm{c},nm}\right|$ and the bandwidth of $S_{ff}^{(\beta)}$ are adequately smaller than $\Delta\beta_{\mathrm{b},nm}^{\mathrm{dev}}$, S_{ff} becomes a narrow delta-function-like distribution and the convolution contains only a gradually varying part of $p_{\Delta\beta_\mathrm{b}}(\Delta\beta_{\mathrm{c},nm})$;

therefore, Eq. 6.30 can be approximated as

$$\begin{aligned}\bar{H}_{nm}\left(\Delta\beta_{\mathrm{c},nm},R_{\mathrm{b}}\right) &\approx \kappa_{nm}^{2}\left[2\pi p_{\Delta\beta_{\mathrm{b}}}\left(\Delta\beta_{\mathrm{c},nm}\right)\right] = \kappa_{nm}^{2} p_{\Delta\tilde{\nu}_{\mathrm{b}}}\left(\Delta\tilde{\nu}_{\mathrm{c},nm}\right) \\ &\approx \kappa_{nm}^{2}\frac{2}{\sqrt{\left(\frac{\beta_{\mathrm{c},n}d_{nm}}{R_{\mathrm{b}}}\right)^{2}-\Delta\beta_{\mathrm{c},nm}^{2}}} = \kappa_{nm}^{2}\frac{\lambda}{\pi\sqrt{\left(\frac{n_{\mathrm{eff,c},n}d_{nm}}{R_{\mathrm{b}}}\right)^{2}-\Delta n_{\mathrm{eff,c},nm}^{2}}},\end{aligned} \tag{6.31}$$

which is also obtained from Eq. 6.15 by approximating the PSD $S_{ff}^{(\beta)}$ as the probability distribution of $\Delta\beta_{\mathrm{b}}$—shown in Eq. 6.29— with constant R_{b}. In the case of homogeneous MCFs ($\Delta\beta_{\mathrm{c},nm}=0$), Eq. 6.31 is reduced to

$$\bar{H}_{nm}\left(R_{\mathrm{b}}\right) \approx \kappa_{nm}^{2}\frac{2R_{\mathrm{b}}}{\beta_{\mathrm{c},n}d_{nm}} = \kappa_{nm}^{2}\frac{\lambda R_{\mathrm{b}}}{\pi n_{\mathrm{eff,c},n}d_{nm}}, \tag{6.32}$$

which coincides with Eq. 3.12 in Chapter 3. The difference between Eq. 6.31 and Eq. 6.32 is less than 0.1 dB when $\Delta\beta_{\mathrm{c}} < 0.21\beta_{\mathrm{c}}d/R_{\mathrm{b}}$; therefore, Eq. 6.32 may be also used for estimating the XT of a bent heterogeneous MCF with small $\Delta\beta_{\mathrm{c}}$.

Parallel to the above study, by assuming constant R_{b} and twist rate, Koshiba *et al.* derived and reported a closed-form approximation of the average power-coupling coefficient $\bar{H}$ as [75]:

$$\bar{H}_{nm} = \kappa_{nm}^{2}\sqrt{2}l_{\mathrm{cor}}\left[\frac{1}{\sqrt{a\left(b+\sqrt{ac}\right)}}+\frac{1}{\sqrt{c\left(b+\sqrt{ac}\right)}}\right], \tag{6.33}$$

$$a = 1+\left(\Delta\beta_{\mathrm{c},nm}l_{\mathrm{cor}}-\frac{B_{nm}l_{\mathrm{cor}}}{R_{\mathrm{b}}}\right)^{2}, \tag{6.34}$$

$$b = 1+\left(\Delta\beta_{\mathrm{c},nm}l_{\mathrm{cor}}\right)^{2}-\left(\frac{B_{nm}l_{\mathrm{cor}}}{R_{\mathrm{b}}}\right)^{2}, \tag{6.35}$$

$$c = 1+\left(\Delta\beta_{\mathrm{c},nm}l_{\mathrm{cor}}+\frac{B_{nm}l_{\mathrm{cor}}}{R_{\mathrm{b}}}\right)^{2}, \tag{6.36}$$

$$B_{nm} = \sqrt{\left(\beta_{\mathrm{c},n}x_{n}-\beta_{\mathrm{c},m}x_{m}\right)^{2}+\left(\beta_{\mathrm{c},n}y_{n}-\beta_{\mathrm{c},m}y_{m}\right)^{2}}, \tag{6.37}$$

where B_{nm} can be approximated as $\beta_{\mathrm{c},n}d_{nm}$ if $\beta_{\mathrm{c},m}/\beta_{\mathrm{c},n}\simeq 1$. They also reported that Eqs. 6.33–6.37 agreed well with measurement results.

Figure 6.3 shows comparisons between $\bar{H}$ calculated by using Eq. 6.30 and $\bar{H}$ calculated by using Eqs. 6.33–6.37. Figures 6.3a and 6.3b show the PSDs normalized with respect to the Lorentzian S_{ff} and to the arcsine distribution $p_{\Delta\beta_{\mathrm{b}}}$, respectively. The Lorentzian and arcsine distributions represent the spectra of the perturbations induced by the structure fluctuation and by the macrobend, respectively. Solid lines represent $\bar{H}$ calculated by using Eq. 6.30 and dashed lines represent $\bar{H}$ calculated by using Eqs. 6.33–6.37; however, the solid lines and the dashed lines are overlapped, and we can only see the solid lines. Accordingly, it was clearly confirmed that

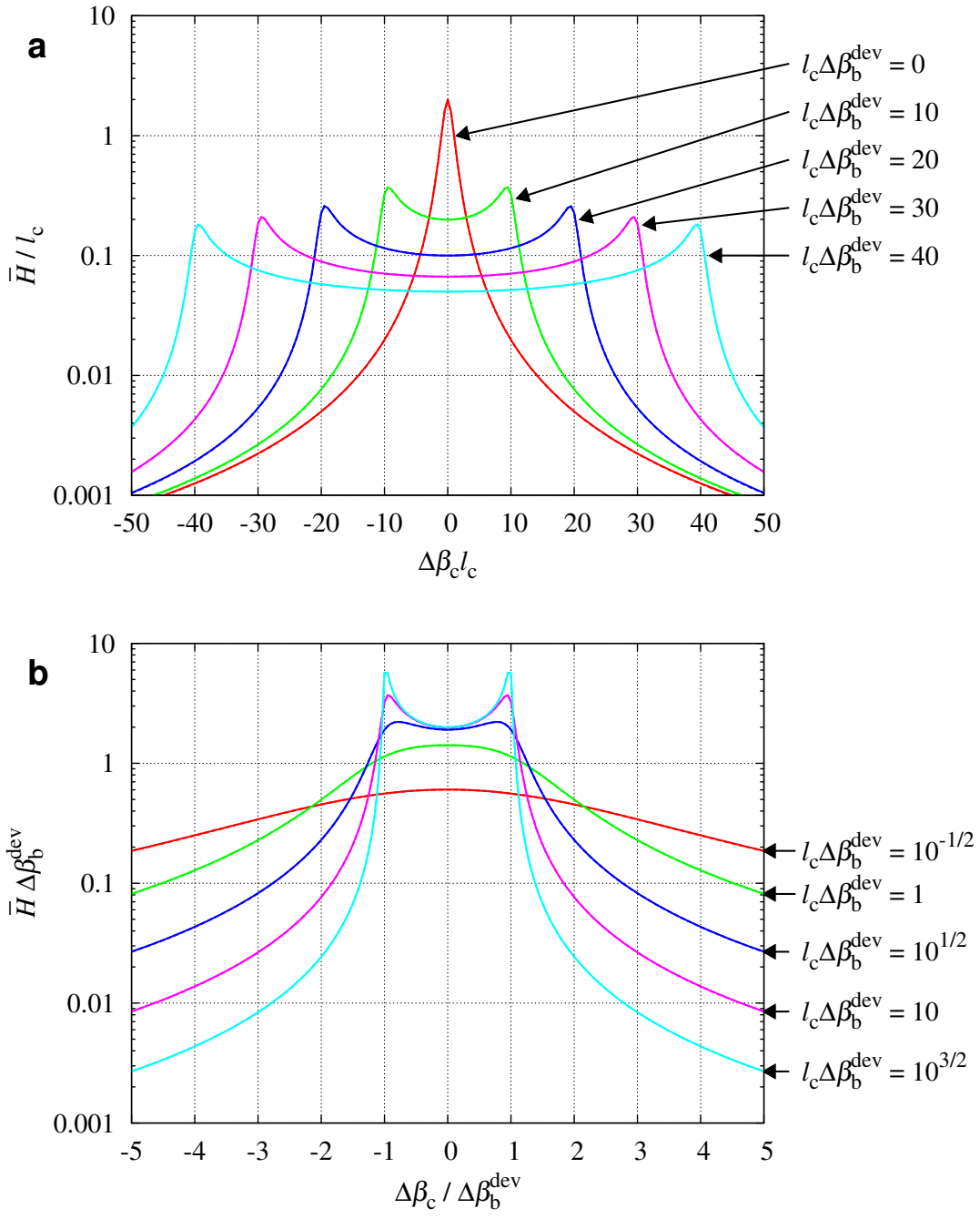

Fig. 6.3: Comparisons between $\bar{H}$ calculated by using Eq. 6.30 and $\bar{H}$ calculated by using Eqs. 6.33–6.37. (a) $\bar{H}$ normalized with respect to the Lorentzian, (b) $\bar{H}$ normalized with respect to the arcsine distribution. Solid lines: $\bar{H}$ calculated by using Eq. 6.30, dashed lines: $\bar{H}$ calculated by using Eqs. 6.33–6.37. The solid lines and the dashed lines are overlapped.

Eq. 6.30 is equivalent to the expression of $\bar{H}$ with Eqs. 6.33–6.37, and it can be also said that the set of Eqs. 6.33–6.37 is a closed-form solution of the convolution of the Lorentzian and the arcsine distribution.

It is difficult to interpret physical meaning of Eqs. 6.33–6.37 intuitively, but this closed-form expression is powerful and easy to estimate the mean XT.

6.5 Crosstalk Suppression Methods Related to Macrobend and Structure Fluctuation

Based on the above derivations, it can be understood that the XT is proportional to the power of the mode-coupling coefficient and to the PSD of the perturbations. Of course, the suppression of the mode-coupling coefficient is important and various ways were proposed for confining power into cores such as high-index small-diameter core structure [77, 78], hole-assisted core structure [41], trench-assisted core structures [66, 74, 79, 80] (see Chapter 3 for Refs. [74, 79, 80]), and photonic-crystal structures [28, 29, 81].

The PSD can be intuitively explained as the amount of the phase matching. Accordingly, how to suppress the PSD can be understood as how to suppress the phase matching. In this section, the methods for suppressing the phase matching are described.

The phase matching suppression methods can be categorized into some types according to how to utilize what kind of the perturbations. Here, three types of suppression methods are explained in the following subsections. A schematic example of $\bar{H}_{nm}\left(\Delta\beta_{\mathrm{c},nm}, R_{\mathrm{b}}\right)$ in Eq. 6.30 shown in Fig. 6.4 will help with understanding, along with Fig. 6.3.

6.5.1 Utilization of the Propagation Constant Mismatch

One is the method utilizing the propagation constant mismatch $\Delta\beta_{\mathrm{c}}$ to suppress the phase matching [15, 17, 30]. As shown as the non-phase-matching regions in Fig. 6.4, $\Delta\beta_{\mathrm{c}}$ larger than $\Delta\beta_{\mathrm{b}}^{\mathrm{dev}}$ can prevent the bend-induced phase-matching between dissimilar cores, and can suppress the XT. In other words, for suppressing the XT, the bending radius of the MCF has to be managed to be *adequately* larger than the critical bending radius R_{pk}:

$$R_{\mathrm{pk}} = \frac{B_{nm}}{\left|\Delta\beta_{\mathrm{c},nm}\right|} \approx d_{nm}\frac{\beta_{\mathrm{c},n}}{\left|\Delta\beta_{\mathrm{c},nm}\right|} = d_{nm}\frac{n_{\mathrm{eff,c},n}}{\left|\Delta n_{\mathrm{eff,c},nm}\right|}, \tag{6.38}$$

that is, R_{b} where Eq. 6.31 can be infinite, or the maximal R_{b} where the phase matching due to the macrobend can occur even if there is no structure fluctuation—an approximate solution was derived in Chapter 2, and an rigorous one was reported in Ref. [75] later. Some margin from R_{pk} is needed for avoiding the phase matching induced by the spectral broadening of S_{ff}, due to the structural fluctuations. In heterogeneous MCFs, it is preferred if the

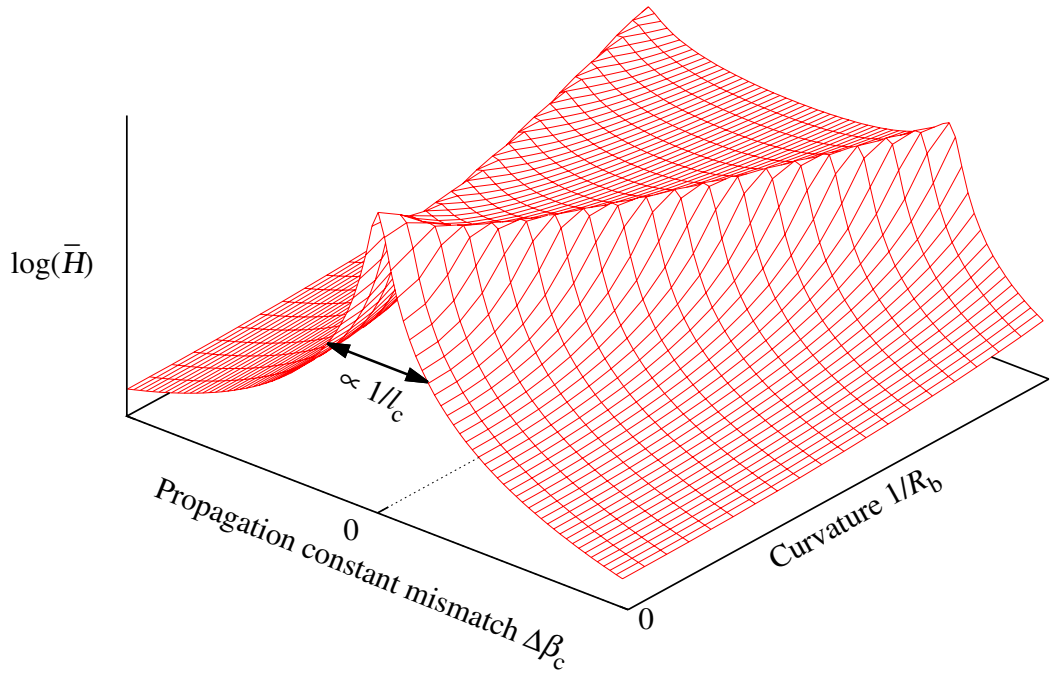

(a) 3-dimensional plot.

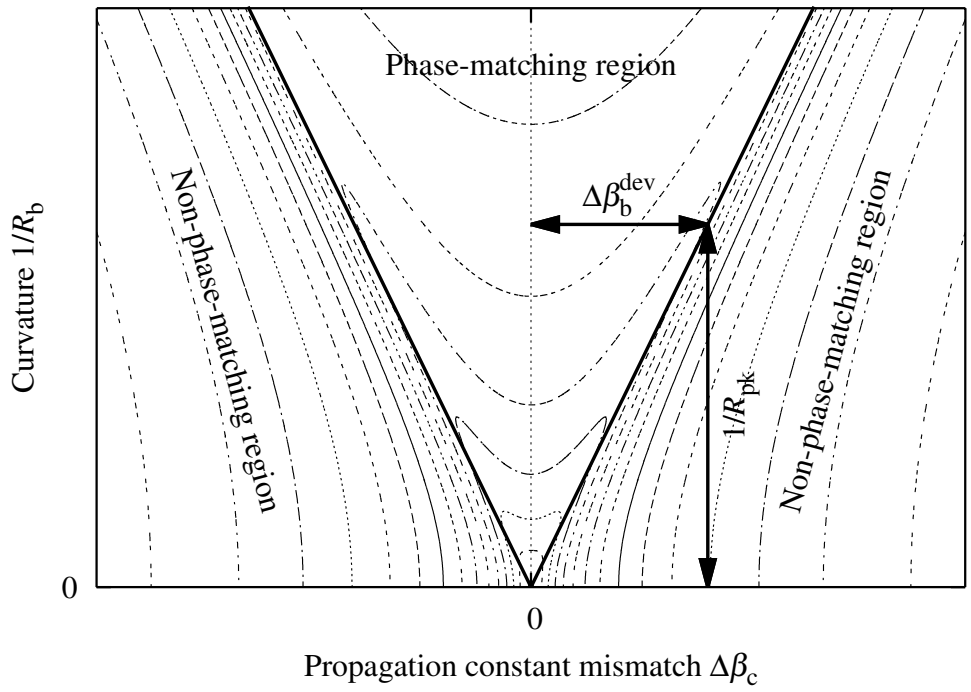

(b) Contour map of $\log(\bar{H})$. Thick solid lines are the thresholds between the phase-matching region and the non-phase-matching region.

Fig. 6.4: A schematic example of the average power-coupling coefficient $\bar{H}$, as a function of the propagation constant mismatch $\Delta\beta_c$ and the curvature $1/R_b$, in the case that twist of an MCF is gradual and random enough.

correlation length l_{cor} of the structural fluctuation can be elongated, because the spectral broadening of S_{ff} can be narrowed and the PSD leakage into the non-phase-matching region can be suppressed, as shown in Figs. 6.3b and 6.4.

If most part of an MCF is deployed in gentle-bend conditions, a slight difference in propagation constants or effective indices may be enough for the phase matching suppression [65].

Since the typical winding radii of fiber spools are around 10 cm and R_{pk} less than 10 cm requires very large difference in core structure, as shown in Section 2.2, most of XT measurements and transmission experiments reported in various papers are considered to have been conducted in the phase-matching region. A hexagonal MCF with three kinds of cores shown in Section 2.2.7 is an exception, but it has a large difference in optical properties between cores so that R_{pk} can be smaller than the bobbin radius of 140 mm.

Recently, Saitoh *et al.* reported that up to two kinds of dissimilar step-index cores can be designed to achieve R_{pk} around 5 cm while achieving a similar A_{eff} of around 80 μm^{2}at 1550 nm, and other good optical properties [82]. Tu *et al.* also reported that up to two kinds of dissimilar trench-assisted cores can be designed to achieve R_{pk} around 5 cm while achieving a similar A_{eff} of around 100 μm^2 [83].

6.5.2 Utilization of the Bend-induced Perturbation

The bend can also be utilized for the phase matching suppression, as described in Chapter 3. As shown in Figs. 6.3a and 6.4, enlargement of the bend-induced perturbation—caused by the increase of the curvature or the decrease of the bending radius— can spread the PSD and suppress the XT even in the case of homogeneous MCFs ($\Delta\beta_{\mathrm{c}} = 0$). Identical core structure is rather desirable for suppressing the PSD. The PSD changes gradually with the bend radius, and there is no drastic PSD increase like that around R_{pk} in the case of heterogeneous MCFs, since the PSD is suppressed in the phase-matching region. As shown in Eq. 6.32, the mean XT of a homogeneous MCF is proportional to the average bending radius, where $|\Delta\beta_{\mathrm{c},nm}|$ and the bandwidth of $S_{ff}^{(\beta)}$ are adequately smaller than $\Delta\beta_{\mathrm{b},nm}^{\mathrm{dev}}$. Therefore, if the average bending radius of the MCF is managed to be smaller than a certain value, or if the MCF is deployed in bend-challenged conditions, low XT can be achieved with identical cores.

6.5.3 Utilization of the Longitudinal Structural Fluctuation

As shown in Figs. 6.3b and 6.4a, the power spectrum of the perturbations is broadened by the longitudinal structural fluctuations. If the R_{ff} due to the structure fluctuation has a very short correlation length l_{cor}, the power spectrum spreads broadly over the propagation constant mismatch $\Delta\beta_{\mathrm{c}}$, and thus the PSD may be suppressed even in the case of an unbent homogeneous MCF ($\Delta\beta_{\mathrm{c}} = 0$, $1/R_{\mathrm{b}} = 0$). A homogeneous MCF utilizing the longitudinal structural fluctuations was conceptually proposed by Takenaga *et al.* as “quasi-homogeneous MCF” in

Refs. [77, 78]. To the author's knowledge, the XT suppression by the structural fluctuation has not been actually observed yet, because the bend-induced perturbations are much larger than the fluctuation induced perturbations in the measurement conditions. However, the structural fluctuation may work when the MCF is cabled and installed in very-gently-bent conditions. For example, $l_{\mathrm{cor}}\Delta\beta_{\mathrm{b},nm}^{\mathrm{dev}} \simeq l_{\mathrm{cor}}\beta_{\mathrm{c}}d/R_{\mathrm{b}}$ of 1.3, 1/3, 1.0×10^{-1}, 1.0×10^{-2}, and 1.0×10^{-3} correspond to 1-dB, 5-dB, 10-dB, 20-dB, and 30-dB decreases in $\bar{H}$ from Eq. 6.32 at $\Delta\beta_{\mathrm{c}}=0$, respectively.

6.6 Conclusion of This Chapter

We reviewed the essence of the recent studies on the XT, clarify ambiguous points of the studies, and derived an intuitively interpretable expression of the average power-coupling coefficient as the convolution of the arcsine distribution—the spectrum of the perturbation induced by the macrobend— and the Lorentzian distribution—the spectrum of the perturbation induced by the structure fluctuation. The derived expression was confirmed to be equivalent to the closed-form expression in Ref. [75]. Based on the newly derived expression, we showed how the structure fluctuation and macrobend can affect the crosstalk, and organized previously-reported methods for crosstalk suppression.

6.A Appendix: Calculation of Eq. 6.30 for Figs. 6.3 and 6.4

Based on the following relationships of the Fourier transform:

$$J_0\left(\Delta\beta_{\mathrm{b}}\zeta\right) \xrightarrow{\text{Fourier transform}} p_{\Delta\tilde{\nu}_{\mathrm{b}}}\left(\Delta\tilde{\nu}_{\mathrm{c}}\right) = 2\pi p_{\Delta\beta_{\mathrm{b}}}\left(\Delta\beta_{\mathrm{c}}\right), \tag{6.39}$$

$$R_{ff}\left(\zeta\right) \xrightarrow{\text{Fourier transform}} S_{ff}^{(\tilde{\nu})}\left(\Delta\tilde{\nu}_{\mathrm{c}}\right) = 2\pi S_{ff}^{(\beta)}\left(\Delta\beta_{\mathrm{c}}\right), \tag{6.40}$$

$$f\cdot g \xrightarrow{\text{Fourier transform}} \left(F*G\right)_{\Delta\tilde{\nu}} = \frac{1}{2\pi}\left(F*G\right)_{\Delta\beta}, \tag{6.41}$$

where $J_0(x)$ is the Bessel function of the first kind of order zero, and functions F and G represents the Fourier transform of functions f and g respectively; we calculated Eq. 6.30 numerically by performing the fast Fourier transform (FFT) on the following relations:

$$J_0\left(\Delta\beta_{\mathrm{b}}\zeta\right)R_{ff}\left(\zeta\right) \xrightarrow{\text{Fourier transform}} \left(p_{\Delta\tilde{\nu}_{\mathrm{b}}} * S_{ff}^{(\tilde{\nu})}\right)_{\Delta\tilde{\nu}_{\mathrm{b}}}\left(\Delta\tilde{\nu}_{\mathrm{c}}\right) = 2\pi\left(p_{\Delta\beta_{\mathrm{b}}} * S_{ff}^{(\beta)}\right)_{\Delta\beta_{\mathrm{b}}}\left(\Delta\beta_{\mathrm{c}}\right). \tag{6.42}$$

We calculated adequately-broad bandwidths of the PSD so that the aliasing noise caused by the FFT can be suppressed in the plotted ranges.

Chapter 7

Crosstalk Behaviors in Harsh Environments

7.1 Introduction to This Chapter

Toward the practical realization of the multi-core fiber (MCF), various factors that can can degrade the inter-core crosstalk (XT) must be cared, since the MCF can be installed in harsh environments. For examples, actually-deployed MCF link can consist of concatenated short MCFs and have many splicing points, the MCF may be tightly bent at around splices and connections, and the microbend—that is, the microscopic fiber bend induced by external stresses— can be an issue when the MCF is cabled. So, XT caused by these factors must be suppressed for realizing long-haul transmissions.

Therefore, in this chapter, we present the results on the study on the effects of the fiber splice, the tight macrobend, and the microbend on the XT.

7.2 Effect of the Fiber Splice on the Crosstalk

7.2.1 Experimental Setup for Evaluating the Effect of Misalignment on the Crosstalk

To study on the effect of fiber splices on the XT, we evaluated XT variations due to the misalignment with fabricated MCFs. The evaluated MCF samples were 200 m of MCF-B30, and 17.4 km of MCF-E. We measured the mean XT by using the setup shown in Fig. 2.6 and the wavelength scanning method described in Section 3.6.2, while the core of the launching SMF was traversed on a line connecting Core 2, Core 1, and Core 5 on the input end of the MCF (see Fig. 7.1). The measured wavelengths were 1547.5 nm (scanning range:1525–1570 nm) for MCF-B30, and 1625 nm (scanning range: 1620–1630 nm).

In this measurement setup, the XT can occur at the input splice, during propagation, and at the output splice, as shown in Fig. 7.2. The behavior of the XT occurred during propagation was elucidated in the previous chapters, and can be measured using the launching and receiving SMFs that are aligned to MCF cores with negligible misalignments. The behavior of the XT occurred at a splice can be predicted with the conventional theory; however, it has not been confirmed whether or not the conventional theory is applicable to the XT at the MCF splice. So, it is important to confirm whether or not the formula can be applicable to the MCF splice, given the inapplicability of

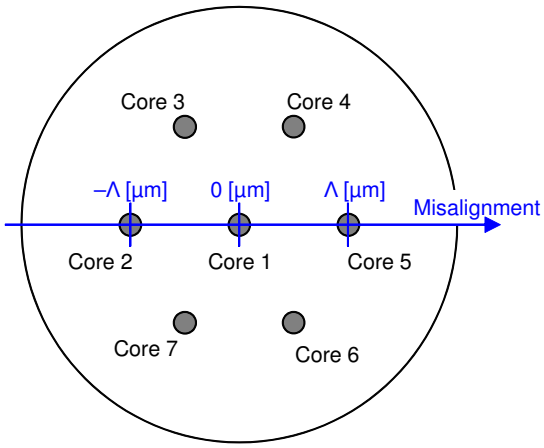

Fig. 7.1: The misalignment of the launching SMF core from Core 1, applied in the experiment. Λ: the core pitch.

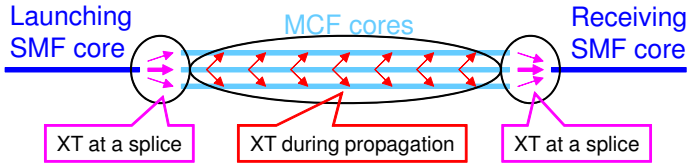

Fig. 7.2: Crosstalk-inducing factors in the measurement setup.

the conventional coupled-mode theory to the XT during propagation and the coupled power floor observed after the misaligned splice of MCF-E and a step-index SMF, which were shown in the previous chapters.

7.2.2 Theoretical Predictions of the Crosstalk for the Experiment

Based on the conventional theory, the behavior of the XT occurred at as splice is expected to be predictable with Eq. 3.17—the conventional formula of the power coupling at a butt joint.

Figure 7.3 shows the calculated relationships between the misalignment and the normalized power in each core of the MCFs.

Figures 7.3a and 7.3b show the relationships between the *misalignment* and the core-guided powers just after the input splice, which are the power coupling at a butt joint and were calculated using Eq. 3.17 from the mode profiles calculated with the full-vector finite-element imaginary-distance beam propagation method [32]. As shown in Fig. 7.1, the positive and negative directions represent the directions for Core 5 and Core 2, respectively, from Core 1. The power difference between different cores is caused by the difference in the distance between the each MCF core and the launching SMF core, as shown in Fig. 7.4.

Figures 7.3c and 7.3d show the relationships between the *misalignment* and the core-guided powers just before the output splice, which are the sums of the XT from the center core to the outer cores during propagation and

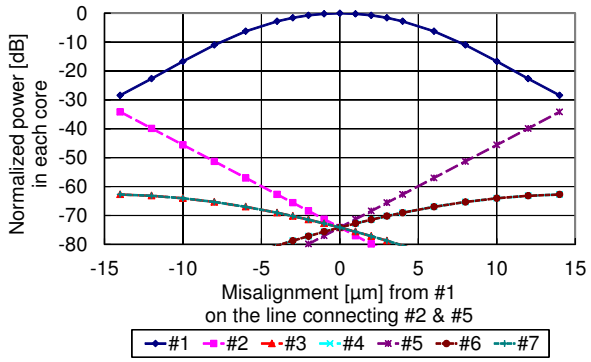

(a) Just after the input splice for MCF-B30, or the power coupling at a butt joint.

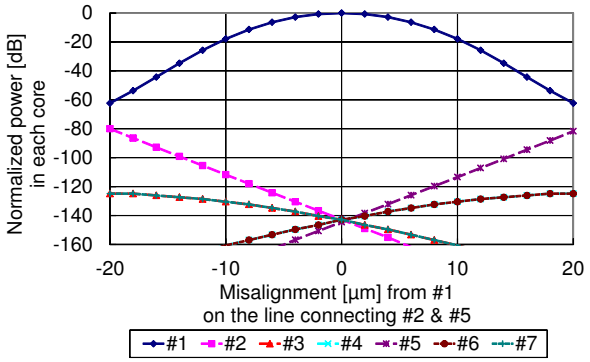

(b) Just after the input splice for MCF-E, or the power coupling at a butt joint.

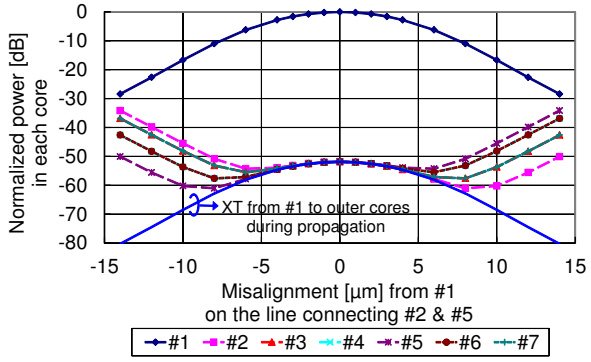

(c) Just before the output splice for MCF-B30.

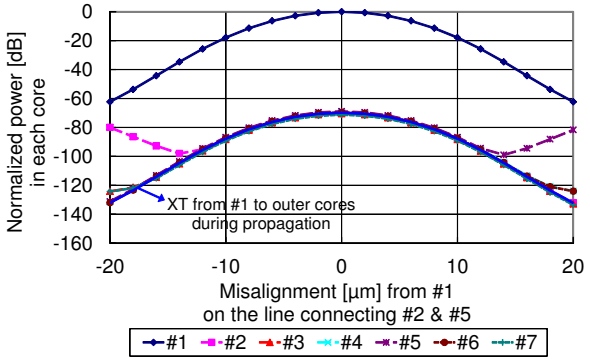

(d) Just before the output splice for MCF-E.

Fig. 7.3: Calculated power in each core of the MCFs with the misaligned excitations. Note that the scales are different between the left and the right graphs

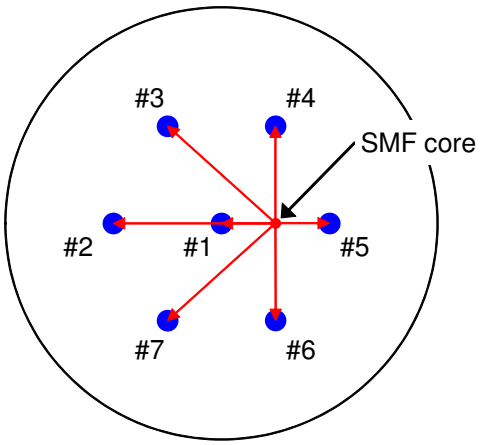

Fig. 7.4: Misalignments of the SMF core from each MCF cores. Red arrows represent the distance between the each MCF core and the launching SMF core.

the results of Figs 7.3a and 7.3b. We used measured mean XT from the center core to the outer cores for the calculation of Figs. 7.3c and 7.3d.

The power that is received from each of the MCF cores by the receiving SMF is almost equivalent to the power guided by the each of the MCF cores just before the output splice (Figs. 7.3c and 7.3d), or the power changes at the output splice was expected to be negligible for the experiment, because inter-core power coupling at the output end can be negligibly lower than the power in the each of the MCF cores—the inter-core power coupling at the input/output end equals to the normalized powers of the outer cores at the misalignment of 0 μm in Figs. 7.3a and 7.3b.

7.2.3 Measurement Results

Figure 7.5 shows the measured relationships between the misalignment and the received powers. The marks are the measured values, and the lines are the theoretical values shown in Figs. 7.3c and 7.3d. The measured values agreed well with the theoretical values.

Figure 7.6 shows the relationships between the misalignment and the mean XT, calculated from the data of Fig. 7.5. The marks represent the measured values, and the lines represent the theoretical values. Of course, the measured values agreed well with the theoretical values, as is the case with Fig. 7.5. Therefore, the XT occurred at the fiber splices can be predicted using Eq. 3.17—the conventional formula of the power coupling at the butt joint. However, there can be the cases where the power coupling through the cladding modes is not negligible, as described in Section 3.6.1—e.g., the case of very-low-crosstalk MCF with step-index cores.

In this experiment, no significant XT variations were observed with the both MCFs for the misalignment of several micrometers. Accordingly, XT increase at fiber splices can be negligible for the evaluated MCFs when

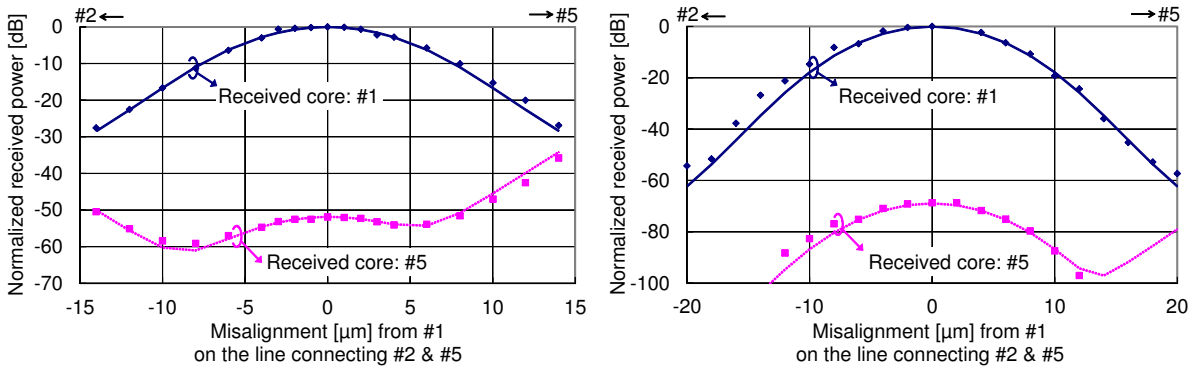

(a) MCF-B30. (b) MCF-E.

Fig. 7.5: Powers received from each of Core 1 and Core 5 with the input-end misalignment, which is shown in Fig. 7.1. Marks: the measured values, lines: the calculated values shown in Figs. 7.3c and 7.3d.

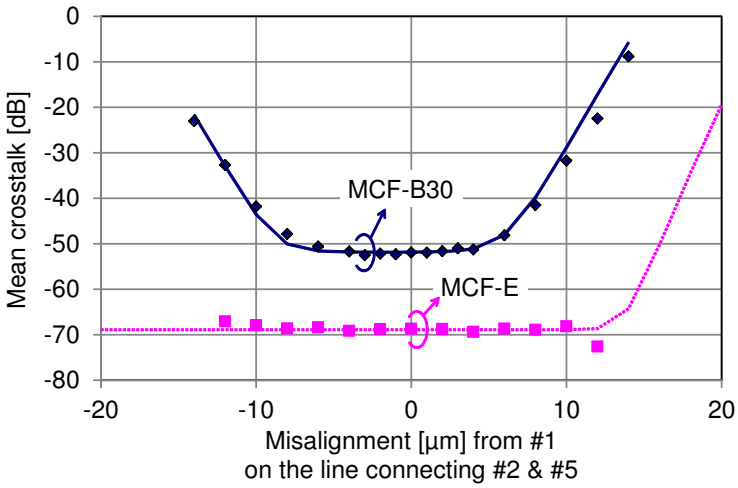

Fig. 7.6: Relationships between the misalignment and the mean crosstalk. Marks: the measured values, lines: the calculated values.

splicing loss (butt joint coupling loss) is properly suppressed, e.g., at most 0.5 dB or lower.

7.3 Effect of the Tight Bend on the Crosstalk

Though significant dependence of the XT on the fiber bend and structure has been elucidated as described in the previous chapters, the measurement results have been reported only for the loose bend, and there are no results for the tight bend.

In this section, we present the XT behavior in the tightly bent MCF.

7.3.1 Applicability of Coupled-Power Equations Only with Core Modes to Tightly Bent MCFs

The mean XT in the MCF is accumulated by obeying the coupled-power equation (CPE):

$$\begin{aligned}\frac{dP_n}{dz} &= \sum_{m\neq n} H_{nm}P_m - \sum_{m\neq n} H_{mn}P_n \\ &= \sum_{m\neq n} H_{nm}\left(P_m - P_n\right), \qquad (\because H_{nm} = H_{mn}),\end{aligned} \tag{7.1}$$

where P_n is the power in Core n, and H_{nm} is the power-coupling coefficient (PCC) from Core m to Core n. The PCC for the MCF has been significantly elucidated, as presented and reviewed in the previous chapters.

However, since Eq. 7.1 is the PCE only for direct couplings between core modes, and since the bend loss can be understood as the power coupling from core modes to the cladding modes in a bent fiber, Eq. 7.1 is considered to be inapplicable to a tightly bent MCF if the bend losses of its cores are large. This can be also understood as

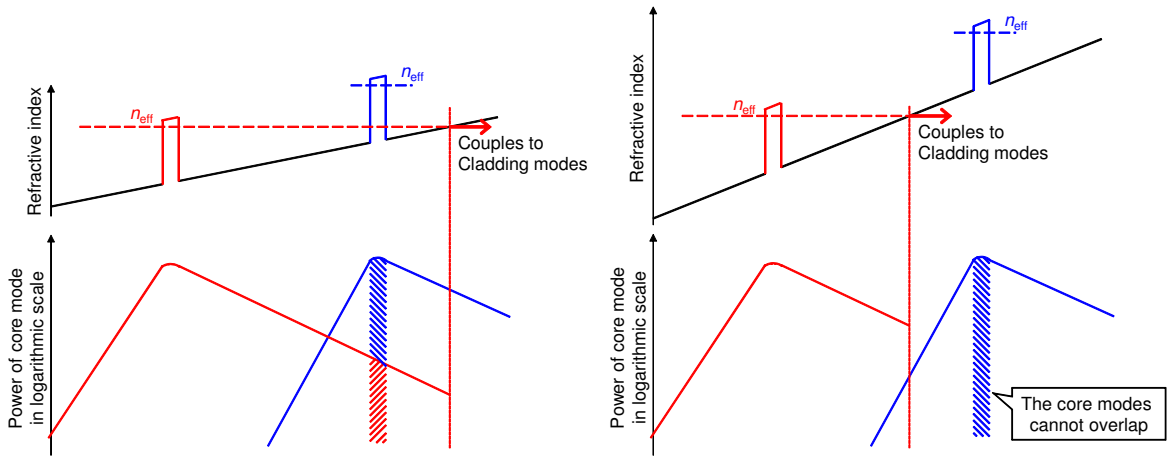

(a) Loosely bent MCF. (b) Tightly bent MCF.

Fig. 7.7: Schematic illustrations of core-mode profiles in a bent MCF.

follows: core modes can always overlap within a core area—the area of permittivity perturbation— in a *loosely* bent MCF, as shown in Fig. 7.7a, but the core modes cannot always overlap within the core in the *tightly* bent MCF as shown in Fig. 7.7b, thus the power coupling between the cores inevitably mediated by cladding modes.

Therefore, we will derive the CPE that includes the powers of the cladding modes and reveal the XT behavior in the tightly bent MCF.

7.3.2 Coupled-Power Equations Including Cladding Modes

The CPE with the cladding modes can be expressed as

$$\begin{aligned}\frac{dP_{\mathrm{Core}:n}}{dz} &= \sum_{m\neq n} H_{\mathrm{Core}:n,\mathrm{Core}:m} P_{\mathrm{Core}:m} - \sum_{m\neq n} H_{\mathrm{Core}:m,\mathrm{Core}:n} P_{\mathrm{Core}:n} \\ &\quad + \sum_{l} H_{\mathrm{Core}:n,\mathrm{Clad}:l} P_{\mathrm{Clad}:l} - \sum_{l} H_{\mathrm{Clad}:l,\mathrm{Core}:n} P_{\mathrm{Core}:n}, \qquad (7.2)\\ \frac{dP_{\mathrm{Clad}:l}}{dz} &= \sum_{m} H_{\mathrm{Clad}:l,\mathrm{Core}:m} P_{\mathrm{Core}:m} - \sum_{m} H_{\mathrm{Core}:m,\mathrm{Clad}:l} P_{\mathrm{Clad}:l} \\ &\quad + \sum_{k\neq l} H_{\mathrm{Clad}:l,\mathrm{Clad}:k} P_{\mathrm{Clad}:k} - \sum_{k\neq l} H_{\mathrm{Clad}:k,\mathrm{Clad}:l} P_{\mathrm{Clad}:l} - \alpha_{\mathrm{Clad}:l} P_{\mathrm{Clad}:l}, \qquad (7.3)\end{aligned}$$

where P is the power guided by each mode, and the subscriptions that Core:n and Clad:l represents Core mode n and Cladding mode l, respectively, and $\alpha_{\mathrm{Clad}:l}$ is the additional power loss coefficient of Cladding mode l compared with the core modes, which can include the losses due to scattering and absorption in the coating, and due to the radiation outside of the fiber. The attenuation coefficients of the core modes were assumed to be equal and thus omitted in Eqs. 7.2 and 7.3. In this section, we deal with the powers and PCCs that are statistically averaged over

twist angle of the MCF, and call "the modes that are not guided by the cores" the cladding modes, which include the modes propagating in the coating.

If we neglect the recoupling of the power from the cladding to the core, the bend loss coefficient [/unit length] of Core n is understood as the sum of the power coupling coefficients [/unit length] from Core n to all cladding modes in the bent condition, and represented as

$$\alpha_{\text{bend:}n} = \sum_{l} H_{\text{Clad:}l,\text{Core:}n}. \tag{7.4}$$

The bend loss coefficient in [dB/unit length] can be obtained by simply multiplying $10/\ln 10$ to Eq. 7.4.

However, it is very difficult and impractical to derive all of the PCCs related to cladding modes and loss coefficients of all cladding modes; therefore, for an approximation, we assume the countless cladding modes as one continuous imaginary mode. Then, Eqs. 7.2 and 7.3 can be simplified as

$$\begin{aligned}\frac{dP_{\text{Core:}n}}{dz} &= \sum_{m\neq n} H_{\text{Core:}n,\text{Core:}m} P_{\text{Core:}m} - \sum_{m\neq n} H_{\text{Core:}m,\text{Core:}n} P_{\text{Core:}n} \\ &\quad + \sum_{l} H_{\text{Core:}n,\text{Clad}(m)} P_{\text{Clad}(m)} - \sum_{l} H_{\text{Clad,Core:}n} P_{\text{Core:}n}, \end{aligned} \tag{7.5}$$

$$\frac{dP_{\text{Clad}(m)}}{dz} = \sum_{m} H_{\text{Clad,Core:}m} P_{\text{Core:}m} - \left(\sum_{i} H_{\text{Core:}i,\text{Clad}(m)} + \alpha_{\text{Clad}(m)} \right) P_{\text{Clad}(m)}, \tag{7.6}$$

where $P_{\text{Clad}(m)}$ is the power in the cladding modes coupled from Core mode m, $H_{\text{Core:}i,\text{Clad}(m)}$ the PCC from $P_{\text{Clad}(m)}$ to $P_{\text{Core:}i}$, and $\alpha_{\text{Clad}(m)}$ the loss coefficient of $P_{\text{Clad}(m)}$. Since the power distribution in the cladding may depend on the core position from which the power coupled to the cladding, we treat the powers coupled from different cores individually, thus introducing the notations of $P_{\text{Clad}(m)}$, $H_{\text{Core:}i,\text{Clad}(m)}$, and $\alpha_{\text{Clad}(m)}$.

If we assume that the bend is longitudinally constant and that $\alpha_{\text{Clad}} \gg H$, the power coupling to the cladding, and power loss in the cladding can be nearly counterbalanced—not completely because the system is not loss-less—; therefore $dP_{\text{Clad}(m)}/dz \approx 0$ can hold. Accordingly, $P_{\text{Clad}(m)}$ can be obtained as:

$$P_{\text{Clad}(m)} \approx \frac{H_{\text{Clad,Core:}m} P_{\text{Core:}m}}{\sum_i H_{\text{Core:}i,\text{Clad}(m)} + \alpha_{\text{Clad}(m)}}. \tag{7.7}$$

By substituting Eq. 7.7 to Eq. 7.5, we obtain

$$\begin{aligned}\frac{dP_{\text{Core:}n}}{dz} &\approx \sum_{m\neq n} H_{\text{Core:}n,\text{Core:}m} P_{\text{Core:}m} - \sum_{m\neq n} H_{\text{Core:}m,\text{Core:}n} P_{\text{Core:}n} \\ &\quad + \sum_{m} \frac{H_{\text{Core:}n,\text{Clad}(m)} \alpha_{\text{bend:}m} P_{\text{Core:}m}}{\sum_i H_{\text{Core:}i,\text{Clad}(m)} + \alpha_{\text{Clad}(m)}} - \alpha_{\text{bend:}n} P_{\text{Core:}n}, \end{aligned} \tag{7.8}$$

where

$$\alpha_{\text{bend:}n} = H_{\text{Clad,Core:}n}. \tag{7.9}$$

In normal CPEs, the reciprocity of the PCC—$H_{\text{Clad,Core:}n} = H_{\text{Core:}n,\text{Clad}}$— holds for the conservation of power; however, in Eqs. 7.5 and 7.6, the reciprocity of the PCC does not hold, because the cladding modes are treated as the one imaginary mode—the PCC from the imaginary cladding mode to a core depends on the positions of cores, from which the power is coupled to the cladding, and to which the power is coupled from the cladding, since the power distribution of the imaginary mode depends on the core position from which the power is coupled to the cladding, as we mentioned above. Nevertheless, we may assume

$$H_{\text{Core:}n,\text{Clad}(m)} = H_{\text{Clad,Core:}n}\eta_{nm} = \alpha_{\text{bend:}n}\eta_{nm}, \tag{7.10}$$

where H_{nm} represents the correction factor for the PCC from the imaginary cladding mode to Core n, for the power originated in Core m. H_{nm} can correct the PCC dependence on the core positions due to the bias of the power distribution in the cladding. Thus, Eq. 7.8 can rewritten as

$$\begin{aligned}\frac{dP_{\text{Core:}n}}{dz} \approx &\sum_{m\neq n} H_{\text{Core:}n,\text{Core:}m}P_{\text{Core:}m} - \sum_{m\neq n} H_{\text{Core:}m,\text{Core:}n}P_{\text{Core:}n} \\ &+ \sum_{m} \alpha_{\text{bend:}n}\tilde{\eta}_{nm}\alpha_{\text{bend:}m}P_{\text{Core:}m} - \alpha_{\text{bend:}n}P_{\text{Core:}n},\end{aligned} \tag{7.11}$$

where

$$\tilde{\eta}_{nm} = \frac{\eta_{nm}}{\sum_i \alpha_{\text{bend:}i}\eta_{im} + \alpha_{\text{Clad}(m)}}. \tag{7.12}$$

$\tilde{\eta}$ can be effectively independent of α_{bend} if $\alpha_{\text{bend}} \ll \alpha_{\text{Clad}}$ holds, and $\alpha_{\text{bend}} \ll \alpha_{\text{Clad}}$ may hold in general fibers in which the light propagations in the cladding modes are suppressed.

From here, we discuss the case where two identical cores are coupled with low XT, for further simple description. $P_{\text{Core:}m} - P_{\text{Core:}n}$ can be approximated as $P_{\text{Core:}m}$, since the XT is low. Since the bend losses are equivalent between the identical cores, the last term ($-\alpha_{\text{bend}n}P_{\text{Core:}n}$) in the right-hand side of Eq. 7.11 can be omitted for XT consideration. Thus, Eq. 7.11 can be reduced to

$$\frac{dP_n}{dz} \approx \left(H_{nm} + \tilde{\eta}_{nm}\alpha_{\text{bend}}^2\right)P_m. \tag{7.13}$$

Let L the total length of the MCF, and L_{bend} the length of the tightly-bent part of the MCF, the mean XT from

Core m to Core n can be expressed as

$$\mu_{X,nm} = \frac{P_n}{P_m} \approx H_{nm}L + \tilde{\eta}_{nm}\alpha_{\text{bend}}^2 L_{\text{bend}}. \tag{7.14}$$

Therefore, the XT increase $\mu_{X,\text{IC}}$ from the indirect coupling due to the tight bend can be derived as

$$\mu_{X,\text{IC},nm} = \tilde{\eta}_{nm}\alpha_{\text{bend}}^2 L_{\text{bend}}, \tag{7.15}$$

in the linear scale, and as

$$\mu_{X,\text{IC},nm}^{[\text{dB}]} = 10\log_{10}\left(1 + \frac{\tilde{\eta}_{nm}\alpha_{\text{bend}}^2 L_{\text{bend}}}{H_{nm}L}\right), \tag{7.16}$$

in the decibel scale.

7.3.3 Measurement

To validate the discussion in the previous section, we evaluated the XT increase from the tight bend with an actual MCF. We fabricated an MCF (MCF-G) with identical step-index cores, so that the XT increase due to the indirect coupling can be evaluated without the effect of the difference in the macrobend loss between the cores. The core Δ was $\sim$0.35%, the core diameter was $\sim$8.9 μm, and the core pitch was $\sim$45 μm.

Figure 7.8 shows the measurement setup for measuring the XT increase due to the tight bend. The XT increase was evaluated with the XT increase from the XT measured in the reference condition [see Fig. 7.8a] to the XT measured in the tightly bent condition [See Fig. 7.8b]. The XT was measured as the mean XT, averaged over 10-nm wavelength span from the XT spectra obtained by using the wavelength scanning method described in Section 3.6.2. The light was launched to and received from the MCF cores by using trench-assisted single-mode fibers (TA-SMFs). The total length of the MCF was 22 m. The length of the tight-bend-applied part was 2 m, and most of the rest was loosely bent (R_b = 140 mm) and arranged after the 2-m-long tightly-bent portion to suppress the power in the cladding modes—the power received at the midpoint between the cores in the end facet of the MCF was low enough even when the light was incident at the midpoint of the cores at the another end. The XT increases were measured at the tight bend radii R_tb of 7.5 mm and 10 mm, and at the wavelengths from 1540 nm to 1625 nm with the step of 5 nm, for measuring at various levels of α_bend. The measured mean XT for the MCF without the tight bend was less than the measurement floor, which was in the order of 10^{-7} for this measurement; therefore the variation of the XT from direct coupling, proportional to the bend radius, is negligible.

Figure 7.9 shows the measurement results for the XT increase due to the tight bend. The solid circles represent the measurement results, and the solid line represents the linear regression using Eq. 7.15 with the fitting parameter

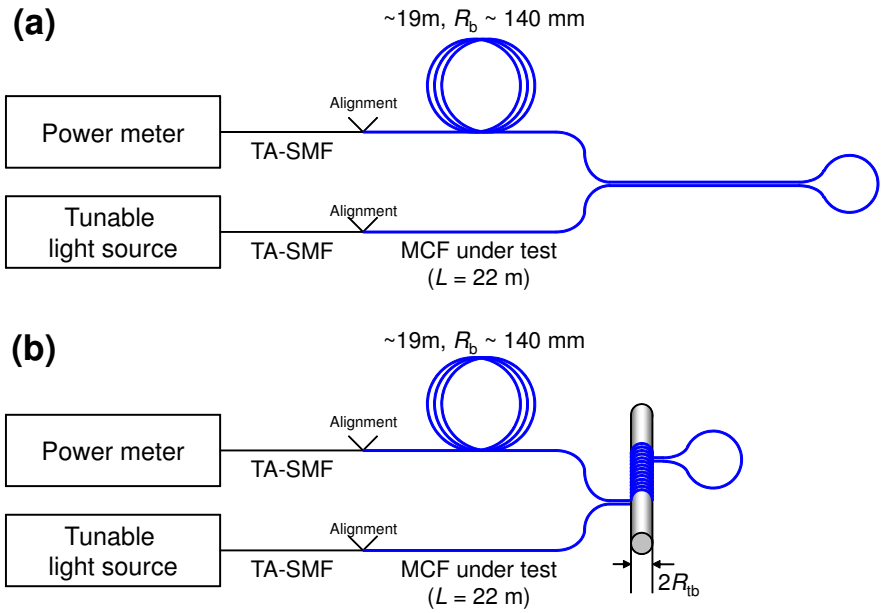

Fig. 7.8: Experimental setup for measuring (a) the reference XT and (b) tight-bend-increased XT.

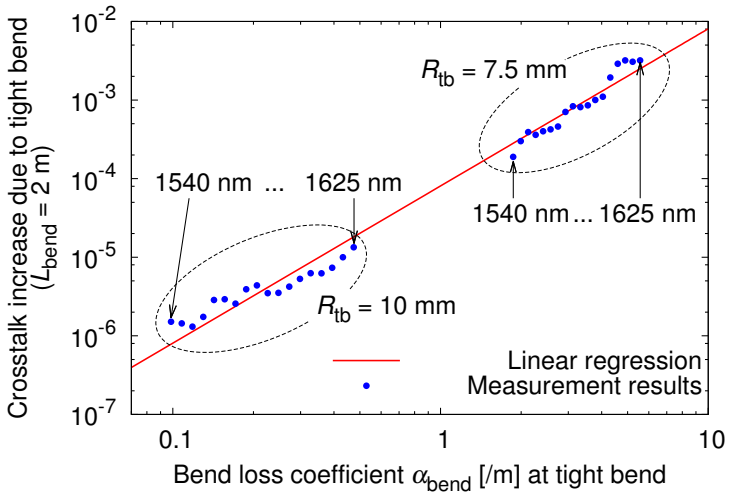

Fig. 7.9: The relationship between bend loss coefficient α_{bend} and XT increase due to tight bend of the fabricated MCF (MCF-G).

of $\tilde{\eta}$. In this case, $\tilde{\eta}$ was fitted to be $\sim 4.0 \times 10^{-5}$ m. Since Fig. 7.9 is a double logarithmic plot, only the relationship of $y = ax^b$ can be the straight line, and the slope of the line is $\log_{10} b$; therefore, it was clearly confirmed that the XT increase due to the tight bend is proportional to the square of the bend loss coefficient α_{bend}.

Based on these results, in applications where MCFs can be tightly bent, suppression of the bend loss may be important not only for the loss suppression itself but also for XT suppression.

7.4 Effect of the Microbend on the Crosstalk

7.4.1 Measurement

To study the effect of the microbend on the XT, we evaluated XT variations due to the microbend by measuring the XT of a heterogeneous MCF (MCF-B30, described in Chapter 2) and a homogeneous MCF (MCF-H, described in Ref. [84]). Table 7.1 shows the fiber properties of the MCFs. Figure 7.10 shows the dependences of the average power-coupling coefficient $\bar{H}$ on microbend conditions for MCF-B30 and for MCF-H. The microbend was applied by winding the MCFs on a 140-mm-radius bobbin with sandpaper (grade P240) at winding tension T. $\bar{H}$ at T = 0 N was measured using a 140-mm-radius bobbin *without* the sandpaper. For MCF-B30, $\bar{H}$ from the center core to an outer core was plotted. For MCF-H, the average of $\bar{H}$s between the three pairs of the neighboring cores was plotted. The values of $\bar{H}$ were calculated obtained using coupled power equation from values of measured mean

Table. 7.1: Characteristics of the evaluated MCFs

	MCF-B30 (heterogeneous)	MCF-H (homogeneous)
Core arrangement	7 cores arranged on equilateral triangular lattice	3 cores arranged on equilateral triangular lattice
Core Δ	0.38% (all core)	0.32% (all core)
Core diameter	8.1 μm (the center core) 9.4 μm (outer cores)	11.2 μm (all core)
Core pitch	30 μm	38 μm
Mode-coupling coefficient in design	9.8×10^{-1} /m at 1550 nm[a,b]	1.0×10^{-1} /m at 1550 nm
Difference of n_{eff} between cores in design	Δ0.046% at 1550 nm[b]	Δ 0%
Cladding diameter	125 μm	125 μm
Coating diameter	248 μm	244 μm

[a] Recalculated from a precise refractive index profile as the average mode-coupling coefficient (shown in Eq. 6.10).

[b] Values between the center core and an outer core.

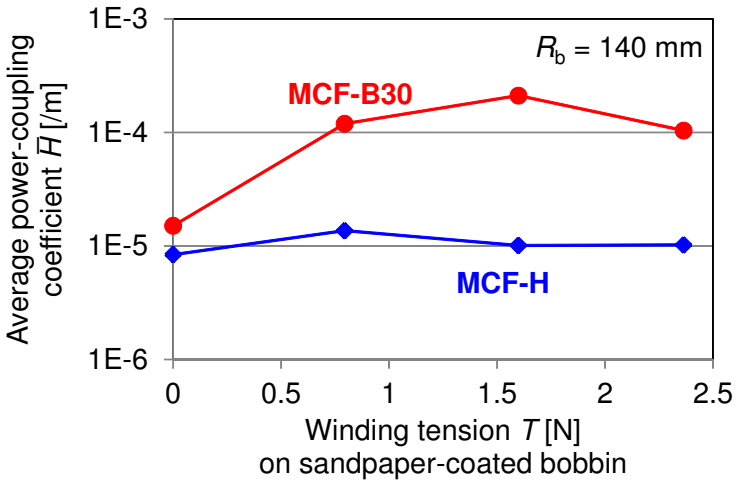

Fig. 7.10: Dependences of the microbend on the mean crosstalk (average power-coupling coefficient) for MCF-B30 (heterogeneous) and MCF-H (homogeneous), measured by wavelength scanning method described in Section 3.6.2 with 100-m fibers at λ = 1550 nm.

XT. $\bar{H}$ of the heterogeneous MCF was increased by the microbend, but that of the homogeneous MCF was varied only slightly.

7.4.2 Discussion

This results can be explained based on the discussion in Chapter 6. In Sections 6.3 and 6.4, S_{ff} only includes structure fluctuation, and $p_{\Delta\beta_b}(\Delta\beta_c)$ includes macrobend perturbation that gradually varies in longitudinal direction. Based on the assumption that the macrobend perturbation is gradual enough compared to l_{cor}, we may redefine the S_{ff} as the PSD of high frequency perturbations other than the macrobend perturbation, and thus S_{ff} may include not only the effect of structure fluctuation but also the effect of microbend, in Eq. 6.30 and Eqs. 6.33–6.37. In this case, the increase of the microbend can be understood as the decrease of the correlation length l_{cor} of S_{ff}. The microbend may induce β perturbations both within a core (Fig. 6.2a) and between cores (Fig. 6.2c), and may be induced by various ways such as winding on a sandpaper-coated bobbin, winding on a wire mesh bobbin, and actual cabling. Depending on how the microbend is induced, the shape of S_{ff} for the structure fluctuation and the microbend could possibly be different from the Lorentzian—i.e., S_{ff} only for the structure fluctuation. Thus, we need to investigate further details of the effect of the microbend on the crosstalk through experiment.

However, as a first step, we will evaluate the measurement results by assuming that S_{ff} for the structure fluctuation and the microbend. The results may be well explained as the shortening of l_{cor} by using Eqs. 6.33–6.37 or Eq. 6.30. Figure 7.11 shows comparisons of the average power-coupling coefficients $\bar{H}$s obtained from the measurement results and those obtained from Eqs. 6.33–6.37. Figure 7.11a shows the dependences of $\bar{H}$ in MCF-B30

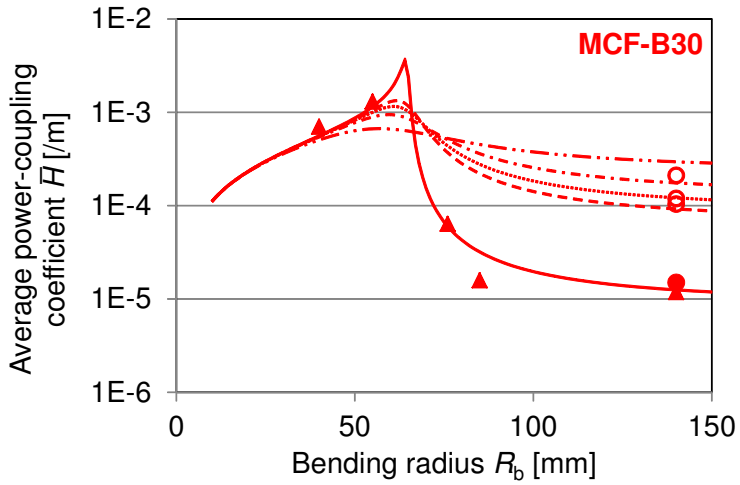

(a) The dependences of $\bar{H}$ in MCF-B30 on the bending radius R_b and on the microbend.

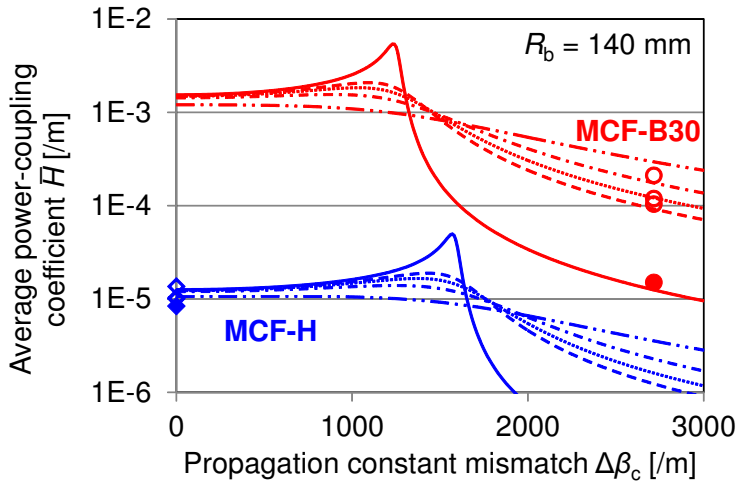

(b) The dependence of $\bar{H}$ in MCF-B30 and MCF-H on the propagation constant mismatch $\Delta\beta_c$ and on the microbend at R_b = 140 mm.

Fig. 7.11: Comparisons of the average power-coupling coefficient $\bar{H}$s obtained from the measurements and from Eqs. 6.33–6.37. Closed-marks: $\bar{H}$ measured without the microbend, open-marks: $\bar{H}$ measured with the microbend, triangles: $\bar{H}$ measured by averaging the crosstalk by rewinding 2-m fiber 10 times (Section 2.2.5), circles: $\bar{H}$ measured using the wavelength scanning method with 100-m fiber. Solid lines: $\bar{H}$ calculated at l_{cor} = 3 cm, dashed lines: $\bar{H}$ at l_{cor} = 4 mm, dotted lines: $\bar{H}$ at l_{cor} = 3 mm, dashed-dotted lines: $\bar{H}$ at l_{cor} = 2 mm, dashed-two dotted lines: $\bar{H}$ at l_{cor} = 1 mm.

on R_b, and on whether the microbend is applied or not—that is, difference of l_{cor}— at R_b = 140 mm. When the microbend is not applied, l_{cor} can be estimated to be around 3 cm for this measurement. When the microbend is applied, l_{cor} can be estimated to be around 1 mm–4 mm. Figure 7.11b shows the dependences of $\bar{H}$ in MCF-B30 and MCF-H on the propagation constant mismatch $\Delta\beta_c$ and on whether the microbend is applied or not, at R_b = 140 mm. We can see that $\Delta\beta_c$ between dissimilar cores in MCF-B30 is in the non-phase-matching region and $\bar{H}$ between dissimilar cores is increased by the decreasing of l_{cor}, or by the broadening of the bandwidth of S_{ff}. On the other hand, $\Delta\beta_c$ in MCF-H is designed to be zero and in the center of the phase-matching region; therefore, $\bar{H}$ in MCF-H is hardly affected by the decreasing of l_{cor}, at least if l_{cor} is larger than 1 mm. Based on this evaluation, l_{cor} was shortened from around 3 cm to around 1 mm–4 mm by applying the microbend in these experiments. Though this shortening of l_{cor} did not affect $\bar{H}$ in MCF-H at R_b = 140 mm, the shortening of l_{cor} may decrease $\bar{H}$ in the (quasi-)homogeneous MCF if R_b is adequately large. Thus, we may consider that the microbend is possible to be utilized for suppressing the XT in a very straight homogeneous MCF.

We evaluated the effect of the microbend on the XT by assuming S_{ff} for the structure fluctuation and the microbend as the Lorentzian. However, further investigation of the effect of the microbend on the XT is necessary for elucidating the detailed characteristics of the effect, as we mentioned above.

Though the variations of the power-coupling coefficients for direct power couplings between cores are discussed above, the indirect power coupling through cladding modes may be induced by the microbend loss, as with the macrobend-induced XT increase described in Section 7.3. The XT increase due to the indirect coupling is considered to be predicted using Eqs. 7.11–7.15 where α_{bend} is the loss coefficient of the microbend loss.

7.5 Conclusion of This Chapter

We investigated how the XT can be affected by the fiber splice, the tight macrobend, and the microbend, which may be required/induced in installed MCFs.

To study on the effect of fiber splices on the XT, we evaluated XT variations due to the misalignment with fabricated MCFs. The XT occurred at the fiber splice was able to be predicted using the conventional formula of the power coupling at the butt joint, and no unpredictable results were measured. However, there can be the cases where the power coupling through the cladding modes occurs, as described in Section 3.6.1—e.g., the case of very-low-XT MCF with step-index cores. In the experiment, no significant XT variations were observed with the MCFs for the misalignment of several micrometers. Accordingly, non-negligible coupling loss can be induced by much shorter misalignment compared with the XT at the splice, and XT increases at butt joints can be negligible in the cases of the evaluated MCFs.

As for the effect of the tight bend, we speculated that the power coupling between cores may be mediated by cladding modes, thus developed simplified coupled-power equations including cladding modes. The equations revealed that XT in the tightly bent MCF can be increased from the existing predictions that are derived only from the direct power couplings between the core modes. The XT increase due to the tight bend was theoretically derived to be proportional to the square of the bend loss coefficient, which was also validated by the experimental results.

We also discussed how the microbend can affect the XT in homogeneous and heterogeneous MCFs. By assuming the average power-coupling coefficient affected by the microbend as the convolution of the arcsine distribution and the spectrum of the high frequency perturbation, including the effects of the structure fluctuation and the microbend, we evaluated previously reported measurement results based on the derived expression—the convolution of the arcsine distribution and the Lorentzian distribution, as a first step. The XT increase due to the microbend in the non-phase-matching region of the heterogeneous MCF and the XT insensitivity to the microbend in the homogeneous MCF can be explained by the shortening of the correlation length of the high frequency perturbation. Further investigation on the effect of the microbend on the XT will be reported in the future.

Chapter 8

Conclusion

8.1 Summary

In this thesis, we presented the results of our study on the multi-core fiber (MCF) for high-capacity spatially-multiplexed transmission. The study revealed various characteristics of the inter-core crosstalk (XT) and other properties specific to the MCF, demonstrated the feasibility of the MCF for long-haul transmission, and indicated the design strategy for enhancing the signal-to-noise ratio (SNR) of each core of the MCF under the existence of the XT.

Chapter 2 described the results of our feasibility study on the MCF. We studied on characteristics degradations specific to the MCF, in order to investigate whether or not the degradations can be suppressed. In this study, we revealed that the inter-core XT of the MCF is heavily dependent not only on the fiber structure but also on the fiber bend, from the theoretical and experimental investigations. It was also revealed that the XT is a stochastic value. We also found that the losses of outer cores of a MCF can be degraded if the outer cores are too close to the coating, because the coating has a high refractive index for suppressing the propagation of cladding modes.

In Chapter 3, we proposed a suppression method of the XT of the homogeneous MCF, which utilizes the fiber bend. We developed an approximation model and derived analytical expressions of the statistical characteristics of the XT of the homogeneous MCF, so that we can easily design homogeneous MCFs. The derived expression for the statistical mean of the XT is quite simple, thus are widely used for estimating the XT of homogeneous MCFs at present. From the approximation model, the XT was revealed to have a statistical distribution of the chi-square distribution with 4 degrees of freedom, which was validated by the measurement with a newly-developed XT measurement method using wavelength scanning. Based on the results of Chapter 2 and these developments, we designed and fabricated an all-solid ultra-low-XT homogeneous MCF, and demonstrated that the XT of the MCF can be suppressed enough for ultra-long-haul ($>$10,000 km) transmissions, for the first time.

In Chapter 4, we discussed how the XT behaves stochastically, revealed the behavior of the XT as a noise, and considered and quantified the effect of the XT on Q-factor. The behavior of the XT as a noise depends on the bandwidth of the signal light, thus the effect of the XT on Q-factor depends on the bandwidth of the signal light.

When the bandwidth of the signal light is adequately broad, the XT may behave as a virtual AWGN on the I–Q plane, like ASE and nonlinear noises. If we assume the signal is equally distributed on every constellation point, the XT-induced Q^2-penalty at the Q^2 of 9.8 dB—the BER of 1×10^{-3}— can be less than 1 dB, when the total mean XT from the other cores is less than -16.7 dB for PDM-QPSK, -23.7 dB for PDM-16QAM, and -29.9 dB for PDM-64QAM. When the bandwidth of the signal light is adequately narrow, the XT X can behave as an effectively static coupling, compared to the symbol rate, but can change very gradually with time. So, the margin for the gradual temporal change has to be considered for setting the target level of the XT for the system with adequately narrow bandwidth signal light.

In Chapter 5, we presented a low-loss large-effective-area MCF whose XT is properly suppressed so that the XT can be adequately lower than the amplified spontaneous emission noise and the nonlinear interference noise. The transmission loss of the MCF was no more than 0.17 dB/km, and the lowest among the reported MCFs, to the best of our knowledge. In addition, we discussed how this result enhances the SNR in multi-core transmission systems. In many earlier studies, effective areas of cores of MCFs were enlarged without considering the effect of the XT, thus the XT negated the suppression of nonlinear noise. On the other hand, our presented MCF can improve the SNR in each core more than 2 dB compared with the standard SMF even under the existence of the XT.

Chapter 6 described the detailed characteristics of the XT, including the review of the studies of other groups. We reviewed and organized the essence of the studies on the XT, clarified ambiguous points of the studies, and derived a novel expression of the average power-coupling coefficient. Thus, we can understand the behavior of the XT and can interpret its physical meaning easily. Based on the derived expression, we discussed how the longitudinal fluctuation of fiber structures and the macrobend can affect the XT, and organized major XT suppression methods which have been reported up to the present time.

In Chapter 7, we presented the results of the investigation on how the XT is affected by the fiber splice, the tight macrobend, and the microbend, since these factors are possible to be induced in installed MCFs. For examples, actually-deployed MCF link can consist of concatenated MCFs and have many splicing points, the MCF may be tightly bent at around splices and connections, and the microbend—that is, the microscopic fiber bend induced by external stresses— can be an issue when the MCF is cabled. XT degradations due to these factors can be suppressed by proper designs based on the results.

8.2 Future Work

As presented in this thesis, the characteristics of the XT and other properties specific to the MCF have been well elucidated in the last few years, and we can fabricate MCFs with optical properties that we designed. However, many research issues remain to be solved, toward commercial realization.

To improve the transmission capacity per fiber, it is preferred to enlarge the cladding diameter of the MCF; however, the larger cladding diameter can degrade the mechanical reliability of the MCF [85]. Some groups have reported that a cladding diameter of somewhat larger than 200 μm can be acceptable [62, 86, 87], but no broad consensus have been developed on a concrete limit of the cladding diameter.

It is also desired to find optimal designs of the MCF and the MCF cable that can maximize the total capacity transmitted through limited cross-sectional areas.

We focused on the uncoupled MCF in this thesis, but there are many types of spatial multiplexing technologies as reviewed in Chapter 1. Every technology should be investigated, and the best combination of the technologies should be adopted, so that the fiber capacity can be maximally improved with reasonable cost.

Furthermore, it is important to develop other devices/techniques concerning spatially-multiplexed transmission. For example, connectors, multiplexing/demultiplexing devices, splicing techniques, amplifiers, and transponders are desired to be developed/optimized for spatially-multiplexed transmission networks.

Of course, the MCF must be standardized toward commercial deployments in the long-haul transmission field.

Acknowledgment

First and foremost, I would like to express my sincere appreciation to my supervisor, Prof. Kunimasa Saitoh. His continuous support and guidance were indispensable to complete this thesis and to fulfill all the requirements of the degree. I also would like to deeply appreciate Prof. Masanori Koshiba. His advice made me decide to earn the degree, and paved the way for my entrance into the graduate school of the university. The discussions with them significantly deepened my understanding on the theoretical descriptions of the inter-core crosstalk of the multi-core fiber (MCF).

I wish to thank to Prof. Yoshikazu Miyanaga, Prof. Toshio Nojima, and Prof. Yasutaka Ogawa for their comments for improving and completing the thesis.

I am greatly indebted to Dr. Yoshinari Awaji of the National Institute of Information and Communications Technology (NICT), for his encouragement. His encouragement was an important help for the launch of our research on the MCF.

This research was conducted in Optical Communications R & D Laboratories, Sumitomo Electric Industries, Ltd. I would like to appreciate Dr. Masayuki Shigematsu, the previous General Manager of the Laboratories, and Mr. Kazuhiro Okamoto, the General Manager of the Laboratories, for giving me a chance to write and publish the thesis.

I would like to acknowledge Mr. Eisuke Sasaoka and Mr. Takashi Sasaki of Sumitomo Electric, for their advices and managements on the research and development of the MCF.

I also would like to thank Mr. Toshiki Taru, Mr. Takuji Nagashima, and Mr. Tetsuya Nakanishi of Sumitomo Electric, for fabrications of the optical fibers. The high-quality and low-loss MCFs could not be fabricated without their supports.

I wish to acknowledge Mr. Osamu Shimakawa and Mr. Jun Ito of Sumitomo Electric, for their supports on the alignment of the MCFs and other optical fibers; and Ms. Teiko Akabane, and Ms. Yuko Sasaki of Sumitomo Electric, for their supports on the measurements of optical properties of the optical fibers. Their supports made it possible for me to concentrate on the research and development.

I am also grateful to the members of my research group in Sumitomo Electric, for their helpful discussions. The discussions with them gave me insights on the research.

The sample of MCF-H is a part of a MCF that was fabricated in the collaborative research by Alcatel-Lucent Bell Laboratories and Sumitomo Electric. Though the scope of the collaborative research is out of scope of the

thesis, the discussions with the member of Bell Labs in the collaborative research were very insightful.

This research was supported in part by the National Institute of Information and Communications Technology (NICT), Japan under “Research on Innovative Optical Fiber Technology.”

References

[1] IEEE 802.3 Ethernet Working Group, "IEEE 802.3 industry connections ethernet bandwidth assessment," IEEE, Tech. Rep., Jul. 2012. [Online]. Available: http://www.ieee802.org/3/ad_hoc/bwa/BWA_Report.pdf

[2] E. B. Desurvire, "Capacity demand and technology challenges for lightwave systems in the next two decades," *J. Lightwave Technol.*, vol. 24, no. 12, pp. 4697–4710, Dec. 2006.

[3] R.-J. Essiambre and R. W. Tkach, "Capacity trends and limits of optical communication networks," *Proc. IEEE*, vol. 100, no. 5, pp. 1035–1055, May 2012.

[4] IEEE 802.3 Higher Speed Study Group - TUTORIAL, "An overview: The next generation of ethernet," in *IEEE 802.3 Higher Speed Study Group Plenary Meeting*, Atlanta, Georgia, Nov. 2007. [Online]. Available: http://www.ieee802.org/3/hssg/public/nov07/HSSG_Tutorial_1107.zip

[5] A. Sano, T. Kobayashi, S. Yamanaka, A. Matsuura, H. Kawakami, Y. Miyamoto, K. Ishihara, and H. Masuda, "102.3-Tb/s (224 x 548-Gb/s) C-and extended L-band all-Raman transmission over 240 km using PDM-64QAM single carrier FDM with digital pilot tone," in *Opt. Fiber Commun. Conf. (OFC)*, 2012, paper PDP5C.3.

[6] R.-J. Essiambre, G. Kramer, P. J. Winzer, G. J. Foschini, and B. Goebel, "Capacity limits of optical fiber networks," *J. Lightwave Technol.*, vol. 28, no. 4, pp. 662–701, Feb. 2010.

[7] T. Morioka, "New generation optical infrastructure technologies: "EXAT initiative" towards 2020 and beyond," in *OptoElectron. Commun. Conf. (OECC)*, Hong Kong, Jul. 2009, paper FT4.

[8] S. Inao, T. Sato, S. Sentsui, T. Kuroha, and Y. Nishimura, "Multicore optical fiber," in *Opt. Fiber Commun. Conf. (OFC)*, 1979, paper WB1.

[9] S. Inao, T. Sato, H. Hondo, M. Ogai, S. Sentsui, A. Otake, K. Yoshizaki, K. Ishihara, and N. Uchida, "High density multicore-fiber cable," in *Int. Wire Cable Symp. (IWCS)*, 1979, pp. 370–384.

[10] S. Berdagué and P. Facq, "Mode division multiplexing in optical fibers," *Appl. Opt.*, vol. 21, no. 11, pp. 1950–1955, 1982.

[11] N. Kashima, E. Maekawa, and F. Nihei, "New type of multicore fiber," in *Opt. Fiber Commun. Conf. (OFC)*, 1982, paper ThAA5.

[12] S. Sumida, E. Maekawa, and H. Murata, "Fundamental studies on flat bunched optical fibers," *J. Lightwave Technol.*, vol. 3, no. 1, pp. 159–164, Feb. 1985.

[13] S. Sumida, E. Maekawa, and H. Murata, "Design of bunched optical-fiber parameters for 1.3-μm wavelength

subscriber line use," *J. Lightwave Technol.*, vol. 4, no. 8, pp. 1010–1015, Aug. 1986.

[14] F. Nihei, Y. Yamamoto, and N. Kojima, "Optical subscriber cable technologies in Japan," *J. Lightwave Technol.*, vol. 5, no. 6, pp. 809–821, Jun. 1987.

[15] G. Le Noane, D. Boscher, P. Grosso, J. C. Bizeul, and C. Botton, "Ultra high density cables using a new concept of bunched multicore monomode fibers: A key for the future FTTH networks," in *Int. Wire Cable Symp. (IWCS)*, 1994, pp. 203–210.

[16] J. R. Stern, J. W. Ballance, D. W. Fraulkner, S. Hornung, D. B. Payne, and K. Oakley, "Passive optical local networks for telephony applications and beyond," *Electron. Lett.*, vol. 23, no. 24, pp. 1255–1257, 1987.

[17] M. Koshiba, K. Saitoh, and Y. Kokubun, "Heterogeneous multi-core fibers: proposal and design principle," *IEICE Electron. Express*, vol. 6, no. 2, pp. 98–103, Jan. 2009.

[18] Y. Kokubun and M. Koshiba, "Novel multi-core fibers for mode division multiplexing: proposal and design principle," *IEICE Electron. Express*, vol. 6, no. 8, pp. 522–528, Apr. 2009.

[19] C. Xia, N. Bai, I. Ozdur, X. Zhou, and G. Li, "Supermodes for optical transmission," *Opt. Express*, vol. 19, no. 17, pp. 16 653–16 664, Aug. 2011.

[20] R. Ryf, R. Essiambre, A. Gnauck, S. Randel, M. A. Mestre, C. Schmidt, P. Winzer, R. Delbue, P. Pupalaikis, A. Sureka, T. Hayashi, T. Taru, and T. Sasaki, "Space-division multiplexed transmission over 4200 km 3-core microstructured fiber," in *Opt. Fiber Commun. Conf. (OFC)*, 2012, paper PDP5C.2.

[21] A. Li, A. A. Amin, X. Chen, and W. Shieh, "Reception of mode and polarization multiplexed 107-Gb/s CO-OFDM signal over a two-mode fiber," in *Opt. Fiber Commun. Conf. (OFC)*, 2011, paper PDPB8.

[22] R. Ryf, S. Randel, A. H. Gnauck, C. Bolle, R.-J. Essiambre, P. Winzer, D. W. Peckham, A. McCurdy, and R. Lingle, "Space-division multiplexing over 10 km of three-mode fiber using coherent 6×6 MIMO processing," in *Opt. Fiber Commun. Conf. (OFC)*, 2011, paper PDPB10.

[23] M. Salsi, C. Koebele, D. Sperti, P. Tran, P. Brindel, H. Mardoyan, S. Bigo, A. Boutin, F. Verluise, P. Sillard, M. Bigot-Astruc, L. Provost, F. Cerou, and G. Charlet, "Transmission at 2x100Gb/s, over two modes of 40km-long prototype few-mode fiber, using LCOS based mode multiplexer and demultiplexer," in *Opt. Fiber Commun. Conf. (OFC)*, 2011, paper PDPB9.

[24] V. Sleiffer, Y. Jung, V. Veljanovski, R. van Uden, M. Kuschnerov, Q. Kang, L. Grüner-Nielsen, Y. Sun, D. Richardson, S. ul Alam, F. Poletti, J. Sahu, A. Dhar, H. Chen, B. Inan, T. Koonen, B. Corbett, R. Winfield, A. Ellis, and H. D. Waardt, "73.7 Tb/s (96x3x256-Gb/s) mode-division-multiplexed DP-16QAM transmission with inline MM-EDFA," in *Eur. Conf. Opt. Commun. (ECOC)*, 2012, paper Th.3.C.4.

[25] Y. Awaji, N. Wada, Y. Toda, and T. Hayashi, "World first mode/spatial division multiplexing in multi-core fiber using laguerre-gaussian mode," in *Eur. Conf. Opt. Commun. (ECOC)*, Sep. 2011, paper We.10.P1.55.

[26] Y. Yan, J. Wang, L. Zhang, J.-Y. Yang, I. M. Fazal, N. Ahmed, B. Shamee, A. E. Willner, K. Birnbaum, J. Choi, E. Baris, and S. Dolinar, "New approach for generating and (de) multiplexing OAM modes in a fiber coupler consisting of a central ring and four external cores," in *Eur. Conf. Opt. Commun. (ECOC)*, Sep. 2011, paper We.10.P1.12.

[27] Y. Yue, Y. Yan, N. Ahmed, J.-Y. Yang, L. Zhang, Y. Ren, H. Huang, S. Dolinar, M. Tur, and A. E. Willner, "Mode and propagation effects of optical orbital angular momentum (OAM) modes in a ring fiber," in *Opt. Fiber Commun. Conf. (OFC)*, 2012, paper OM2D.2.

[28] K. Imamura, K. Mukasa, R. Sugizaki, Y. Mimura, and T. Yagi, "Multi-core holey fibers for ultra large capacity wide-band transmission," in *Eur. Conf. Opt. Commun. (ECOC)*, Sep. 2008, paper P.1.17.

[29] K. Imamura, K. Mukasa, Y. Mimura, and T. Yagi, "Multi-core holey fibers for the long-distance (>100 km) ultra large capacity transmission," in *Opt. Fiber Commun. Conf. (OFC)*, Mar. 2009, paper OTuC3.

[30] S. Kumar, U. H. Manyam, and V. Srikant, "Optical fibers having cores with different propagation constants, and methods of manufacturing same," US Patent 6 611 648, Aug. 26, 2003.

[31] A. W. Snyder, "Coupled-mode theory for optical fibers," *J. Opt. Soc. Am.*, vol. 62, no. 11, pp. 1267–1277, Nov. 1972.

[32] K. Saitoh and M. Koshiba, "Full-vectorial imaginary-distance beam propagation method based on a finite element scheme: Application to photonic crystal fibers," *IEEE J. Quant. Electron.*, vol. 38, no. 7, pp. 927–933, 2002.

[33] D. Marcuse, "Influence of curvature on the losses of doubly clad fibers," *Appl. Opt.*, vol. 21, no. 23, pp. 4208–4213, Dec. 1982.

[34] J. Sakaguchi, Y. Awaji, N. Wada, T. Hayashi, T. Nagashima, T. Kobayashi, and M. Watanabe, "Propagation characteristics of seven-core fiber for spatial and wavelength division multiplexed 10-Gbit/s channels," in *Opt. Fiber Commun. Conf. (OFC)*, Mar. 2011, paper OWJ2.

[35] Y. Murakami and H. Tsuchiya, "Bending losses of coated single-mode optical fibers," *IEEE J. Quant. Electron.*, vol. 14, no. 7, pp. 495–501, 1978.

[36] A. Harris and P. Castle, "Bend loss measurements on high numerical aperture single-mode fibers as a function of wavelength and bend radius," *J. Lightwave Technol.*, vol. 4, no. 1, pp. 34–40, 1986.

[37] R. Morgan, J. S. Barton, P. G. Harper, and J. D. C. Jones, "Wavelength dependence of bending loss in monomode optical fibers: effect of the fiber buffer coating," *Opt. Lett.*, vol. 15, no. 17, pp. 947–949, 1990.

[38] A. Sano, H. Masuda, T. Kobayashi, M. Fujiwara, K. Horikoshi, E. Yoshida, Y. Miyamoto, M. Matsui, M. Mizoguchi, H. Yamazaki, Y. Sakamaki, and H. Ishii, "69.1-Tb/s (432 x 171-Gb/s) C- and extended L-band transmission over 240 km using PDM-16-QAM modulation and digital coherent detection," in *Opt. Fiber*

Commun. Conf. (OFC), 2010, paper PDPB7.

[39] X. Zhou, J. Yu, M.-F. Huang, Y. Shao, T. Wang, L. Nelson, P. Magill, M. Birk, P. Borel, D. W. Peckham, and R. Lingle, "64-Tb/s (640x107-Gb/s) PDM-36QAM transmission over 320km using both pre- and post-transmission digital equalization," in *Opt. Fiber Commun. Conf. (OFC)*, 2010, paper PDPB9.

[40] J.-X. Cai, Y. Cai, C. Davidson, D. Foursa, A. Lucero, O. Sinkin, W. Patterson, A. Pilipetskii, G. Mohs, and N. Bergano, "Transmission of 96x100g pre-filtered PDM-RZ-QPSK channels with 300% spectral efficiency over 10,608km and 400% spectral efficiency over 4,368km," in *Opt. Fiber Commun. Conf. (OFC)*, 2010, paper PDPB10.

[41] K. Saitoh, T. Matsui, T. Sakamoto, M. Koshiba, and S. Tomita, "Multi-core hole-assisted fibers for high core density space division multiplexing," in *OptoElectron. Commun. Conf. (OECC)*, Sapporo, Japan, Jul. 2010, paper 7C2-1.

[42] P. Poggiolini, A. Carena, V. Curri, G. Bosco, and F. Forghieri, "Analytical modeling of nonlinear propagation in uncompensated optical transmission links," *IEEE Photon. Technol. Lett.*, vol. 23, no. 11, pp. 742–744, Jun. 2011.

[43] K. Imamura, K. Mukasa, and T. Yagi, "Investigation on multi-core fibers with large Aeff and low micro bending loss," in *Opt. Fiber Commun. Conf. (OFC)*, Mar. 2010, paper OWK6.

[44] K. Imamura, Y. Tsuchida, K. Mukasa, R. Sugizaki, K. Saitoh, and M. Koshiba, "Investigation on multi-core fibers with large Aeff and low micro bending loss," *Opt. Express*, vol. 19, no. 11, pp. 10 595–10 603, May 2011.

[45] B. Zhu, T. Taunay, M. Yan, J. Fini, M. Fishteyn, and E. M. Monberg, "Seven-core multicore fiber transmissions for passive optical network," *Opt. Express*, vol. 18, no. 11, pp. 11 117–11 122, May 2010.

[46] M. Wandel and P. Kristensen, "Fiber designs for high figure of merit and high slope dispersion compensating fibers," *J. Opt. Fiber Commun. Rep.*, vol. 3, no. 1, pp. 25–60, Feb. 2006, rpt. in *Fiber Based Dispersion Compensation*, S. Ramachandran Ed. New York: Springer, 2007.

[47] D. Marcuse, "Microdeformation losses of single-mode fibers," *Appl. Opt.*, vol. 23, no. 7, pp. 1082–1091, Apr. 1984.

[48] D. Gloge, "Optical-fiber packaging and its influence on fiber straightness and loss," *Bell Syst. Tech. J.*, vol. 54, no. 2, pp. 245–262, Feb. 1975.

[49] F. Cocchini, "The lateral rigidity of double-coated optical fibers," *J. Lightwave Technol.*, vol. 13, no. 8, pp. 1706–1710, Aug. 1995.

[50] J. Sakaguchi, Y. Awaji, N. Wada, A. Kanno, T. Kawanishi, T. Hayashi, T. Taru, T. Kobayashi, and M. Watanabe, "109-Tb/s (7 × 97 × 172-Gb/s SDM/WDM/PDM) QPSK transmission through 16.8-km homogeneous

multi-core fiber," in *Opt. Fiber Commun. Conf. (OFC)*, Mar. 2011, paper PDPB6.

[51] Y. Awaji, N. Wada, Y. Toda, and T. Hayashi, "Propagation of laguerre-gaussian mode light through multi-core fiber at telecom wavelength," in *Conf. Lasers and Electro-Opt. (CLEO)*, May 2011, paper CThGG2.

[52] G. B. Arfken and H.-J. Weber, *Mathematical methods for physicists*, 6th ed. Boston: Elsevier, 2005.

[53] P. Winzer, A. Gnauck, A. Konczykowska, F. Jorge, and J. Dupuy, "Penalties from in-band crosstalk for advanced optical modulation formats," in *Eur. Conf. Opt. Commun. (ECOC)*, Sep. 2011, paper Tu.5.B.7.

[54] B. Zhu, T. Taunay, M. Fishteyn, X. Liu, S. Chandrasekhar, M. Yan, J. Fini, E. Monberg, and F. Dimarcello, "112-Tb/s space-division multiplexed DWDM transmission with 14-b/s/Hz aggregate spectral efficiency over a 76.8-km seven-core fiber," *Opt. Express*, vol. 19, no. 17, pp. 16 665–16 671, Aug. 2011.

[55] M. Koshiba, K. Saitoh, K. Takenaga, and S. Matsuo, "Multi-core fiber design and analysis: coupled-mode theory and coupled-power theory," *Opt. Express*, vol. 19, no. 26, pp. B102–B111, Nov. 2011.

[56] R.-J. Essiambre, G. Foschini, P. Winzer, and G. Kramer, "Capacity limits of fiber-optic communication systems," in *Opt. Fiber Commun. Conf. (OFC)*, 2009, paper OThL1.

[57] A. Carena, G. Bosco, V. Curri, P. Poggiolini, M. Tapia Taiba, and F. Forghieri, "Statistical characterization of PM-QPSK signals after propagation in uncompensated fiber links," in *Eur. Conf. Opt. Commun. (ECOC)*, 2010, paper P4.07.

[58] "ITU-T Recommendation G.975.1," Feb. 2004.

[59] H. Zhang, J.-X. Cai, H. G. Batshon, M. Mazurczyk, O. Sinkin, D. Foursa, A. Pilipetskii, G. Mohs, and N. Bergano, "200 Gb/s and dual wavelength 400 Gb/s transmission over transpacific distance at 6 b/s/Hz spectral efficiency," in *Opt. Fiber Commun. Conf. (OFC)*, 2013, paper PDP5A.6.

[60] K. Imamura, K. Mukasa, and R. Sugizaki, "Trench assisted multi-core fiber with large Aeff over 100 μm^2 and low attenuation loss," in *Eur. Conf. Opt. Commun. (ECOC)*, Sep. 2011, paper Mo.1.LeCervin.1.

[61] K. Takenaga, Y. Arakawa, Y. Sasaki, S. Tanigawa, S. Matsuo, K. Saitoh, and M. Koshiba, "A large effective area multi-core fiber with an optimized cladding thickness," *Opt. Express*, vol. 19, no. 26, pp. B543–B550, Nov. 2011.

[62] S. Matsuo, K. Takenaga, Y. Arakawa, Y. Sasaki, S. Tanigawa, K. Saitoh, and M. Koshiba, "Large-effective-area ten-core fiber with cladding diameter of about 200 μm," *Opt. Lett.*, vol. 36, no. 23, pp. 4626–4628, Dec. 2011.

[63] B. Yao, K. Ohsono, N. Shiina, F. Koji, A. Hongo, E. H. Sekiya, and K. Saito, "Reduction of crosstalk by hole-walled multi-core fibers," in *Opt. Fiber Commun. Conf. (OFC)*, 2012, paper OM2D.5.

[64] H. Takara, H. Ono, Y. Abe, H. Masuda, K. Takenaga, S. Matsuo, H. Kubota, K. Shibahara, T. Kobayashi, and Y. Miyamoto, "1000-km 7-core fiber transmission of 10 x 96-Gb/s PDM-16QAM using Raman amplification

with 6.5 W per fiber," *Opt. Express*, vol. 20, no. 9, pp. 10 100–10 105, Apr. 2012.

[65] J. M. Fini, B. Zhu, T. F. Taunay, and M. F. Yan, "Statistics of crosstalk in bent multicore fibers," *Opt. Express*, vol. 18, no. 14, pp. 15 122–15 129, Jun. 2010.

[66] K. Takenaga, Y. Arakawa, S. Tanigawa, N. Guan, S. Matsuo, K. Saitoh, and M. Koshiba, "Reduction of crosstalk by trench-assisted multi-core fiber," in *Opt. Fiber Commun. Conf. (OFC)*, Mar. 2011, paper OWJ4.

[67] J. M. Fini, B. Zhu, T. F. Taunay, M. F. Yan, and K. S. Abedin, "Crosstalk in multicore fibers with randomness: gradual drift vs. short-length variations," *Opt. Express*, vol. 20, no. 2, pp. 949–959, Jan. 2012.

[68] A. Hardy and W. Streifer, "Coupled mode theory of parallel waveguides," *J. Lightwave Technol.*, vol. 3, no. 5, pp. 1135–1146, Oct. 1985.

[69] W. Streifer, M. Osinski, and A. Hardy, "Reformulation of the coupled-mode theory of multiwaveguide systems," *J. Lightwave Technol.*, vol. 5, no. 1, pp. 1–4, Jan. 1987.

[70] S.-L. Chuang, "A coupled mode formulation by reciprocity and a variational principle," *J. Lightwave Technol.*, vol. 5, no. 1, pp. 5–15, Jan. 1987.

[71] H. A. Haus, W. P. Huang, S. Kawakami, and N. A. Whitaker, "Coupled-mode theory of optical waveguides," *J. Lightwave Technol.*, vol. 5, no. 1, pp. 16–23, Jan. 1987.

[72] B. E. Little and W.-P. Huang, "Coupled-mode theory for optical waveguides," *Progress In Electromagnetics Research*, vol. 10, pp. 217–270, 1995.

[73] W.-P. Huang, "Coupled-mode theory for optical waveguides: an overview," *J. Opt. Soc. Am. A*, vol. 11, no. 3, pp. 963–983, 1994.

[74] T. Hayashi, T. Taru, O. Shimakawa, T. Sasaki, and E. Sasaoka, "Design and fabrication of ultra-low crosstalk and low-loss multi-core fiber," *Opt. Express*, vol. 19, no. 17, pp. 16 576–16 592, Aug. 2011.

[75] M. Koshiba, K. Saitoh, K. Takenaga, and S. Matsuo, "Analytical expression of average power-coupling coefficients for estimating intercore crosstalk in multicore fibers," *IEEE Photon. J.*, vol. 4, no. 5, pp. 1987–1995, Oct. 2012.

[76] K. Petermann, "Microbending loss in monomode fibers," *Electron. Lett.*, vol. 12, no. 4, pp. 107–109, Feb. 1976.

[77] K. Takenaga, S. Tanigawa, N. Guan, S. Matsuo, K. Saitoh, and M. Koshiba, "Reduction of crosstalk by quasi-homogeneous solid multi-core fiber," in *Opt. Fiber Commun. Conf. (OFC)*, Mar. 2010, paper OWK7.

[78] K. Takenaga, Y. Arakawa, S. Tanigawa, N. Guan, S. Matsuo, K. Saitoh, and M. Koshiba, "An investigation on crosstalk in multi-core fibers by introducing random fluctuation along longitudinal direction," *IEICE Trans. Commun.*, vol. E94.B, no. 2, pp. 409–416, Feb. 2011.

[79] T. Hayashi, T. Taru, O. Shimakawa, T. Sasaki, and E. Sasaoka, "Low-crosstalk and low-loss multi-core fiber

utilizing fiber bend," in *Opt. Fiber Commun. Conf. (OFC)*, Mar. 2011, paper OWJ3.

[80] T. Hayashi, T. Taru, O. Shimakawa, T. Sasaki, and E. Sasaoka, "Ultra-low-crosstalk multi-core fiber feasible to ultra-long-haul transmission," in *Opt. Fiber Commun. Conf. (OFC)*, Mar. 2011, paper PDPC2.

[81] D. M. Taylor, C. R. Bennett, T. J. Shepherd, L. F. Michaille, M. D. Nielsen, and H. R. Simonsen, "Demonstration of multi-core photonic crystal fibre in an optical interconnect," *Electron. Lett.*, vol. 42, no. 6, pp. 331–332, 2006.

[82] K. Saitoh, M. Koshiba, K. Takenaga, and S. Matsuo, "Low-crosstalk multi-core fibers for long-haul transmission," in *Proc. SPIE*, vol. 8284, Jan. 2012, paper 82840I.

[83] J. Tu, K. Saitoh, M. Koshiba, K. Takenaga, and S. Matsuo, "Design and analysis of large-effective-area heterogeneous trench-assisted multi-core fiber," *Opt. Express*, vol. 20, no. 14, pp. 15 157–15 170, 2012.

[84] R. Ryf, R.-J. Essiambre, S. Randel, A. H. Gnauck, P. J. Winzer, T. Hayashi, T. Taru, and T. Sasaki, "MIMO-based crosstalk suppression in spatially multiplexed 3 × 56-Gb/s PDM-QPSK signals for strongly coupled three-core fiber," *IEEE Photon. Technol. Lett.*, vol. 23, pp. 1469–1471, Oct. 2011.

[85] IEC/TR 62048 ed2.0, "Optical fibres – Reliability – Power law theory," International Electrotechnical Commission, Tech. Rep., May 2011.

[86] K. Imamura, K. Mukasa, and T. Yagi, "Effective space division multiplexing by multi-core fibers," in *Eur. Conf. Opt. Commun. (ECOC)*, Sep. 2010, paper P1.09.

[87] K. Imamura, I. Shimotakahara, K. Mukasa, N. Oyama, and R. Sugizaki, "A study on reliability for large diameter multi-core fibers," in *Int. Wire Cable Symp. (IWCS)*, 2011, paper P-2, pp. 284–288.

List of Publications Related to This Thesis

A. Journal Articles

1. **[Invited]** Tetsuya Hayashi, Toshiki Taru, Osamu Shimakawa, Takashi Sasaki, and Eisuke Sasaoka, "Design and fabrication of ultra-low crosstalk and low-loss multi-core fiber," *Optics Express*, vol. 19, no. 17, pp. 16576–16592, August 15, 2011. [Online]. Available: http://dx.doi.org/10.1364/OE.19.016576
2. Tetsuya Hayashi, Toshiki Taru, Osamu Shimakawa, Takashi Sasaki, and Eisuke Sasaoka, "Characterization of crosstalk in ultra-low-crosstalk multi-core fiber," *Journal of Lightwave Technology*, vol. 30, no. 4, pp. 583–589, February 15, 2012. [Online]. Available: http://dx.doi.org/10.1109/JLT.2011.2177810
3. Jun Sakaguchi, Yoshinari Awaji, Naoya Wada, Atsushi Kanno, Tetsuya Kawanishi, Tetsuya Hayashi, Toshiki Taru, Tetsuya Kobayashi, Masayuki Watanabe, "Space division multiplexed transmission of 109-Tb/s data signals using homogeneous seven-core fiber," *Journal of Lightwave Technology*, vol. 30, no. 4, pp. 658–665, February 15, 2012. [Online]. Available: http://dx.doi.org/10.1109/JLT.2011.2180509
4. Tetsuya Hayashi, Toshiki Taru, Osamu Shimakawa, Takashi Sasaki, and Eisuke Sasaoka, "Uncoupled multi-core fiber enhancing signal-to-noise ratio," *Optics Express*, vol. 20, no. 26, pp. B94–B103, December 10, 2012. [Online]. Available: http://dx.doi.org/10.1364/OE.20.000B94
5. Tetsuya Hayashi, Takashi Sasaki, Eisuke Sasaoka, Kunimasa Saitoh, and Masanori Koshiba, "Physical interpretation of intercore crosstalk in multicore fiber: effects of macrobend, structure fluctuation, and microbend," *Optics Express*, vol. 21, no. 5, pp. 5401–5412, March 11, 2013. [Online]. Available: http://dx.doi.org/10.1364/OE.21.005401
6. Tetsuya Hayashi, Takashi Sasaki, and Eisuke Sasaoka, "Behavior of inter-core crosstalk as a noise and its effect on Q-factor in multi-core fiber," submitted for publication.

B. International Conference Presentations (Refereed)

1. Tetsuya Hayashi, Takuji Nagashima, Osamu Shimakawa, Takashi Sasaki, and Eisuke Sasaoka, "Crosstalk variation of multi-core fibre due to fibre bend," in *European Conference on Optical Communication (ECOC)*, 2010, Torino, Italy, paper We.8.F.6. [Online]. Available: http://dx.doi.org/10.1109/ECOC.2010.5621143

2. Tetsuya Hayashi, Toshiki Taru, Osamu Shimakawa, Takashi Sasaki, and Eisuke Sasaoka, "Low-crosstalk and low-loss multi-core fiber utilizing fiber bend," in *Optical Fiber Communication Conference (OFC)*, 2011, Los Angeles, paper OWJ3. [Online]. Available: http://dx.doi.org/10.1364/OFC.2011.OWJ3
3. Jun Sakaguchi, Yoshinari Awaji, Naoya Wada, Tetsuya Hayashi, Takuji Nagashima, Tetsuya Kobayashi, Masayuki Watanabe, "Propagation characteristics of seven-core fiber for spatial and wavelength division multiplexed 10-Gbit/s channels," in *Optical Fiber Communication Conference (OFC)*, 2011, Los Angeles, paper OWJ2. [Online]. Available: http://dx.doi.org/10.1364/OFC.2011.OWJ2
4. **[Postdeadline]** Tetsuya Hayashi, Toshiki Taru, Osamu Shimakawa, Takashi Sasaki, and Eisuke Sasaoka, "Ultra-low-crosstalk multi-core fiber feasible to ultra-long-haul transmission," in *Optical Fiber Communication Conference (OFC)*, 2011, Los Angeles, paper PDPC2. [Online]. Available: http://dx.doi.org/10.1364/OFC.2011.PDPC2
5. **[Postdeadline]** Jun Sakaguchi, Yoshinari Awaji, Naoya Wada, Atsushi Kanno, Tetsuya Kawanishi, Tetsuya Hayashi, Toshiki Taru, Tetsuya Kobayashi, Masayuki Watanabe, "109-Tb/s (7x97x172-Gb/s SDM/WDM/PDM) QPSK transmission through 16.8-km homogeneous multicore fiber," in *Optical Fiber Communication Conference (OFC)*, 2011, Los Angeles, paper PDPB6. [Online]. Available: http://dx.doi.org/10.1364/OFC.2011.PDPB6
6. Yoshinari Awaji, Naoya Wada, Yasunori Toda, Tetsuya Hayashi, "Propagation of Laguerre-Gaussian mode light through multi-core fiber at telecom wavelength," in *Conference on Lasers and Electro-Optics (CLEO)*, 2011, Baltimore, paper CThGG2. [Online]. Available: http://dx.doi.org/10.1364/CLEO_SI.2011.CThGG2
7. Yoshinari Awaji, Naoya Wada, Yasunori Toda, Tetsuya Hayashi, "World first mode/spatial division multiplexing in multi-core fiber using Laguerre-Gaussian mode," in *European Conference on Optical Communication (ECOC)*, 2011, Geneva, paper We.10.P1.55. [Online]. Available: http://dx.doi.org/10.1364/ECOC.2011.We.10.P1.55
8. Tetsuya Hayashi, Takashi Sasaki, and Eisuke Sasaoka, "Microbending-induced crosstalk increase in heterogeneous multi-core fiber," in *European Conference on Optical Communication (ECOC)*, 2011, Geneva, paper Mo.1.LeCervin.3. [Online]. Available: http://dx.doi.org/10.1364/ECOC.2011.Mo.1.LeCervin.3
9. **[Invited]** Tetsuya Hayashi, Takashi Sasaki, and Eisuke Sasaoka, "Multi-core fibers for high capacity transmission," in *Optical Fiber Communication Conference (OFC)*, 2012, Los Angeles, paper OTu1D.4. [Online]. Available: http://dx.doi.org/10.1364/OFC.2012.OTu1D.4
10. **[Invited]** Tetsuya Hayashi, Toshiki Taru, Osamu Shimakawa, Takashi Sasaki, and Eisuke Sasaoka, "Ultra-low-crosstalk multi-core fiber realizing space-division multiplexed ultra-long-haul transmission," in *Conference on Lasers and Electro-Optics (CLEO)*, 2012, San Jose, paper CTh4G.3. [Online]. Available:

http://dx.doi.org/10.1364/CLEO_SI.2012.CTh4G.3

11. **[Invited]** Tetsuya Hayashi, Takashi Sasaki, and Eisuke Sasaoka, "Multi-core fibers and their crosstalk characteristics," in *IEEE Summer Topical Meeting Series*, 2012, Seattle, paper TuC4.1. [Online]. Available: http://dx.doi.org/10.1109/PHOSST.2012.6280774
12. **[Invited]** Tetsuya Hayashi, Toshiki Taru, Osamu Shimakawa, Takashi Sasaki, and Eisuke Sasaoka, "Low-loss and large-A_{eff} multi-core fiber for SNR enhancement ," in *European Conference on Optical Communication (ECOC)*, 2012, Amsterdam, paper Mo.1.F.3. [Online]. Available: http://dx.doi.org/10.1364/ECEOC.2012.Mo.1.F.3
13. Tetsuya Hayashi, Toshiki Taru, Takashi Sasaki, Kunimasa Saitoh, and Masanori Koshiba, "Crosstalk increase in tightly bent multi-core fiber due to power coupling mediated by cladding modes," in *European Conference on Optical Communication (ECOC)*, 2013, London, paper Mo.3.A.4, to be presented.

C. Book Chapter

1. Tetsuya Hayashi, "Multi-Core Optical Fibers," in *Optical Fiber Telecommunications*, Sixth Edition, I. P. Kaminow, T. Li, and A. E. Willner, eds. Boston, USA: Academic Press/Elsevier, May 2013, vol. A, ch. 9, pp. 321–352. [Online]. Abstract Available: http://dx.doi.org/10.1016/B978-0-12-396958-3.00009-3

D. Domestic Conference Presentations (Non-Refereed)

Themed Meetings (in Japanese with English Abstract)

1. Tetsuya Hayashi, Takuji Nagashima, Osamu Shimakawa, Takashi Sasaki, and Eisuke Sasaoka, "Crosstalk variation of multi-core fibre due to fibre bend," *IEICE Technical Report*, vol. 110, no. 291, OCS2010-96, pp. 51–56, 2010. （林 哲也, 永島 拓志, 島川 修, 佐々木 隆, 笹岡 英資, "曲げ付与によるマルチコアファイバのクロストーク変化," 電子情報通信学会技術研究報告, vol. 110, no. 291, OCS2010-96, pp. 51–56, 2010.）
2. Jun Sakaguchi, Yoshinari Awaji, Naoya Wada, Tetsuya Hayashi, Takuji Nagashima, Tetsuya Kobayashi, Masayuki Watanabe, "5-km Transmission of Spatial and Wavelength Division Multiplexed 10-Gb/s Channels using Heterogeneous Seven-core Fiber," *IEICE Technical Report*, vol. 111, no. 36, OCS2011-4, pp. 15–19, 2011. （坂口 淳, 淡路祥成, 和田尚也, 林 哲也, 永島拓志, 小林哲也, 渡辺正行, "異種型 7 コアファイバを用いた 10-Gb/s チャネル波長×空間多重信号の 5km 伝送," 電子情報通信学会技術研究報告, vol. 111, no. 36, OCS2011-4, pp. 15–19, 2011.）

3. Yoshinari Awaji, Naoya Wada, Yasunori Toda, Tetsuya Hayashi, “Reservation of orbital angular momentum of Laguerre-Gaussian passing thorough seven core fiber,” *IEICE Technical Report*, vol. 111, no. 69, OFT2011-6, pp. 25–28, 2011. （淡路祥成, 和田尚也, 戸田泰則, 林 哲也, “ラゲール・ガウスモードの 7 コアファイバ通過時の軌道角運動量の保存について,” 電子情報通信学会技術研究報告, vol. 111, no. 69, OFT2011-6, pp. 25–28, 2011.）
4. Jun Sakaguchi, Yoshinari Awaji, Naoya Wada, Tetsuya Hayashi, Toshiki Taru, Tetsuya Kobayashi, Masayuki Watanabe, “Transmission of 109-Tb/s SDM/WDM/PDM-QPSK signals through 16.8-km homogeneous 7-core fiber,” *IEICE Technical Report*, vol. 111, no. 92, OCS2011-16, pp. 27–31, 2011.（坂口 淳, 淡路祥成, 和田尚也, 林 哲也, 樽 稔樹, 小林哲也, 渡辺正行, “均一 7 コアファイバを用いた 109-Tb/s 空間/波長/偏波多重 QPSK 信号の 16.8km 伝送,” 電子情報通信学会技術研究報告, vol. 111, no. 92, OCS2011-16, pp. 27–31, 2011.）
5. Jun Sakaguchi, Yoshinari Awaji, Naoya Wada, Atsushi Kanno, Tetsuya Kawanishi, Tetsuya Hayashi, Toshiki Taru, Tetsuya Kobayashi, Masayuki Watanabe, “Technologies on multi-core fiber and spatial division multiplexing enabling extremely advanced optical transmission,” *IEICE Technical Report*, vol. 111, no. 112, LQE2011-21, pp. 29–34, 2011. （坂口 淳, 淡路祥成, 和田尚也, 菅野敦史, 川西哲也, 林 哲也, 樽 稔樹, 小林哲也, 渡辺正行, “伝送容量の飛躍的向上へ向けた空間多重・マルチコアファイバ通信の為の基盤技術,” 電子情報通信学会技術研究報告, vol. 111, no. 112, LQE2011-21, pp. 29–34, 2011.）
6. Tetsuya Hayashi, Osamu Shimakawa, Takuji Nagashima, Takashi Sasaki, and Eisuke Sasaoka, “Investigation of effects of microbending and of small-radius macrobending on crosstalk of a heterogeneous multi-core fiber,” *IEICE Technical Report*, vol. 111, no. 181, OCS2011-45, pp. 1–6, 2011.（林 哲也, 島川 修, 永島拓志, 佐々木 隆, 笹岡英資, “異種コア型マルチコアファイバのクロストークへのマイクロベンド及び小径マクロベンドの影響に関する調査,” 電子情報通信学会技術研究報告, vol. 111, no. 181, OCS2011-45, pp. 1–6, 2011.）
7. Yoshinari Awaji, Naoya Wada, Yasunori Toda, Tetsuya Hayashi, “Laguerre-Gaussian mode division multiplexing in 7-core fiber,” *IEICE Technical Report*, vol. 111, no. 265, OCS2011-82, pp. 145–148, 2011.（淡路祥成, 和田尚也, 戸田泰則, 林 哲也, “7 コアファイバでのラゲール・ガウスモード分割多重,” 電子情報通信学会技術研究報告, vol. 111, no. 265, OCS2011-82, pp. 145–148, 2011.）
8. Tetsuya Hayashi, Takashi Sasaki, and Eisuke Sasaoka, “Effect of inter-core crosstalk of multi-core fiber on Q-factor,” *IEICE Technical Report*, vol. 112, no. 193, OCS2012-34, pp. 31–36, 2012. （林 哲也, 佐々木 隆, 笹岡英資, “マルチコアファイバのクロストークの Q 値への影響,” 電子情報通信学会技術研究報告, vol. 112, no. 193, OCS2012-34, pp. 31–36, 2011.）

General Conferences (in Japanese)

1. Tetsuya Hayashi, Takuji Nagashima, Osamu Shimakawa, Takashi Sasaki, and Eisuke Sasaoka, "Crosstalk Variation of Multi-Core Fiber due to Fiber Bend," in *Proceedings of the 2010 IEICE Communication Society Conference*, Osaka, B-10-16, 2010. （林 哲也, 永島拓志, 島川 修, 佐々木隆, 笹岡英資, "曲げ付与によるマルチコアファイバのクロストーク変化," 2010 年電子情報通信学会ソサイエティ大会, 大阪, B-10-16, 2010.）
2. Tetsuya Hayashi, Toshiki Taru, Osamu Shimakawa, Takashi Sasaki, and Eisuke Sasaoka, "Very Low Crosstalk and Low Loss Multi-Core Fiber," in *Proceedings of the 2011 IEICE General Conference*, Tokyo, B-10-3, 2011. （林 哲也, 樽 稔樹, 島川 修, 佐々木隆, 笹岡英資, "極低クロストーク・低損失マルチコアファイバ," 2011 年電子情報通信学会総合大会, 東京, B-10-3, 2011.）
3. Tetsuya Hayashi, Toshiki Taru, Osamu Shimakawa, Takashi Sasaki, and Eisuke Sasaoka, "Measurement of Crosstalk Distribution of a Very Low Crosstalk Multi-Core Fiber," in *Proceedings of the 2011 IEICE General Conference*, Tokyo, B-10-5, 2011. （林 哲也, 樽 稔樹, 島川 修, 佐々木隆, 笹岡英資, "極低クロストークマルチコアファイバのクロストーク分布の測定," 2011 年電子情報通信学会総合大会, 東京, B-10-5, 2011.）
4. **[Invited]** Tetsuya Hayashi, Toshiki Taru, Osamu Shimakawa, Takashi Sasaki, and Eisuke Sasaoka, "Ultra-Low-Crosstalk Multi-Core Fiber," in *Proceedings of the 2011 IEICE Communications Society Conference*, Sapporo, BI-7-2, 2011. （[招待講演] 林 哲也, 樽 稔樹, 島川 修, 佐々木隆, 笹岡英資, "極低クロストークマルチコアファイバ," 2011 年電子情報通信学会ソサイエティ大会, 札幌, BI-7-2, 2011.）
5. Tetsuya Hayashi, Takashi Sasaki, and Eisuke Sasaoka, "Effect of inter-core crosstalk of multi-core fiber on Q-factor," in *Proceedings of the 2012 IEICE General Conference*, Okayama, B-10-80, 2012. （林 哲也, 佐々木隆, 笹岡英資, "マルチコアファイバのクロストークの Q 値への影響," 2012 年電子情報通信学会総合大会, 岡山, B-10-80, 2012.）
6. Yoshinari Awaji, Naoya Wada, Tetsuya Hayashi, Yasunori Toda, "Novel multiplexed transmission based on multi-core fiber," in *Proceedings of the 2012 IEICE General Conference*, Okayama, C-3-1, 2012. （淡路祥成, 和田尚也, 林 哲也, 戸田泰則, "マルチコアファイバによる新しい多重伝送手法," 2012 年電子情報通信学会総合大会, 岡山, C-3-1, 2012.）
7. Tetsuya Hayashi, Toshiki Taru, Osamu Shimakawa, Takashi Sasaki, and Eisuke Sasaoka, "Low-loss Large-A_{eff} and Low-crosstalk Multi-core Fiber Enabling High SNR," in *Proceedings of the 2012 IEICE Communications Society Conference*, Toyama, B-10-1, 2012. （林 哲也, 樽 稔樹, 島川 修, 佐々木隆, 笹岡英資, "高 SNR を実現する低ロス・大 A_{eff}・低クロストークマルチコアファイバ," 2012 年電子情報通信学会ソ

サイエティ大会, 富山, B-10-1, 2012.）

E. Awards

1. 2011 IEICE Communications Society OCS Young Researchers Award, to Tetsuya Hayashi, for “Crosstalk variation of multi-core fibre due to fibre bend,” *IEICE Technical Report*, vol. 110, no. 291, OCS2010-96, pp. 51–56, 2010. （2011 年 光通信システム研究会 奨励賞: 林 哲也, “曲げ付与によるマルチコアファイバのクロストーク変化,” 電子情報通信学会技術研究報告, vol. 110, no. 291, OCS2010-96, pp. 51–56, 2010. に対して）
2. 2012 IEICE Communications Society OCS Best Paper Award, to Tetsuya Hayashi, Takashi Sasaki, and Eisuke Sasaoka, for “Effect of inter-core crosstalk of multi-core fiber on Q-factor,” *IEICE Technical Report*, vol. 112, no. 193, OCS2012-34, pp. 31–36, 2012. （2011 年 光通信システム研究会 論文賞: 林 哲也, 佐々木 隆, 笹岡 英資, “マルチコアファイバのクロストークの Q 値への影響,” 電子情報通信学会技術研究報告, vol. 112, no. 193, OCS2012-34, pp. 31–36, 2011. に対して）